NUMERICAL SIMULATION OF A LONG-LASTING MESOSCALE CONVECTIVE LINE

by

NEIL DAVID GORDON

B.Sc., University of Auckland, New Zealand
(1972)

B.Sc. (Hons), Victoria University of Wellington, New Zealand
(1973)

SUBMITTED IN PARTIAL FULFILLMENT
OF THE REQUIREMENTS FOR THE
DEGREE OF

DOCTOR OF SCIENCE

at the

MASSACHUSETTS INSTITUTE OF TECHNOLOGY

(FEBRUARY 1978)

Signature of Author..
Department of Meteorology
21 November 1977

Certified by..
Thesis Supervisor

Accepted by..
Chairman, Departmental Committee

/

NUMERICAL SIMULATION OF A LONG-LASTING MESOSCALE CONVECTIVE LINE

by

NEIL DAVID GORDON

Submitted to the Department of Meteorology
on 21 November 1977 in partial fulfillment of
the requirements for the Degree of
Doctor of Science

ABSTRACT

A numerical model which explicitly resolves both the cumulus scale and the mesoscale is developed, tested, and used to simulate a long-lasting mesoscale convective system. The work was motivated by recent observational studies on a cold-front-associated convective line in the NSSL mesonetwork (on 14 May 1970). These studies revealed a mesoscale downdraft over the frontal surface wind shift (apparently driven by evaporative cooling from the tops of deep cumulus), a saturated mesoscale updraft about 25 km behind that, and the eventual development of a reverse circulation with recycled air feeding into the updraft from the rear and weakening the system.

The model uses the anelastic equations, and parameterizations of subgrid diffusion and warm rain microphysics. There is no Coriolis force. Grid spacings are nonuniform normal to the line and in the vertical, with best resolution in the region of expected important convection. Along the line there are just 3 grid-points spaced 4 km apart, with assumed periodicity of 12 km. The numerical differencing is mostly centred in space and time.

To simulate the 14 May system the model is initialized with representative temperature and moisture profiles, and a 2 km deep slab of cold air based on the actual cold front. From a highly unbalanced state with no motion the cold air spreads forward, with the temperature break (TB) at its leading edge moving at about the same speed as the actual cold front. The cold pool acts like a mountain barrier, providing initial uplift and condensation in the low-level air, but producing a gravity (lee) wave structure aloft. As on 14 May, there is a downdraft over the TB, but it is part of the lee wave.

Embryonic cells (i.e., lines of cells) break off periodically from the cloud over the TB and move back, with their initial development slowed by the lee wave and by vertical wind shear. Farther back they develop strongly, attaining peak updrafts of about 15 m s^{-1}, 20 to 30 km behind the TB. While their averaged effect is a mesoscale updraft in the same location as on 14 May, it is neither saturated nor as strong, apparently because of the inadequacy of the representation of the third dimension.

The cells rain out, producing strong in situ evaporative cooling in the cold pool, and leaving cloud debris trailing back from the system in an anvil based at about 6 km. (Because of the comparative weakness of the simulated system, the debris is less extensive than on 14 May and no forward flow of recycled air develops beneath it.) The cold pool is also warmed by diffusion; this warming dominates, slowly weakening the system, so the simulation is discontinued after 250 min.

Thesis Supervisor: Frederick Sanders, Professor of Meteorology.

ACKNOWLEDGEMENTS

I would like to thank Professor Frederick Sanders for his guidance throughout my studies at M.I.T., for initially suggesting the numerical simulation, and for always requiring physical insight. Professor Eugenia Kálnay de Rivas provided invaluable assistance on numerical details, especially during the early stages of designing the model. I had some interesting discussions with Professor David Randall, and thank him for his constructive criticism. Discussions with other faculty and students in the Department of Meteorology, particularly Kerry Emanuel and Dr Peter Yau, were also helpful.

My appreciation is extended to Isabelle Kole for her superb work in drafting the figures.

My stay at M.I.T. would not have been possible without a New Zealand National Research Advisory Council fellowship, and leave granted from the New Zealand Meteorological Service.

This research was partially supported by N.S.F. grant 74-24405ATM, and the numerical computations were carried out at the Goddard Institute for Space Studies under N.A.S.A. grant NGR 22-009-727.

Most of all, I want to thank Jenny Gordon for all her love, help, and encouragement.

TABLE OF CONTENTS

Page

ABSTRACT 2

ACKNOWLEDGEMENTS 4

TABLE OF CONTENTS 5

LIST OF FIGURES 7

LIST OF TABLES 10

1. INTRODUCTION 11

2. NUMERICAL MODEL DESIGN 20

   2.1 Mathematical Definition of the Model 21

      2.1.1 Dynamics and Thermodynamics 21
      2.1.2 Water and Microphysics 25
      2.1.3 Diffusion 32
      2.1.4 Boundary Conditions 35

   2.2 The Numerical Model 37

      2.2.1 The Domain and Grid System 38
      2.2.2 Time Integration 47

3. MODEL VALIDATION AND COMPARISONS AMONG DIFFERENT DOMAIN GEOMETRIES 72

   3.1 Models Used 73

   3.2 Results 77

   3.3 Conclusions 85

Page

4. SIMULATION OF THE CONVECTIVE SYSTEM OF 14 MAY 1970 . . 87
    4.1 Observations 87
    4.2 Model Setup and Initialization 93
    4.3 Results 97
        4.3.1 Overall Description 98
        4.3.2 The Period from 107.3 to 165.4 Minutes . . . 108
            4.3.2.1 Cloud, Rain, and Vertical Velocity Fields 108
            4.3.2.2 Other Fields at 136.8 Minutes . . . 129
        4.3.3 Space- and Time-Averaged Fields over 107.3 to 165.4 Minutes 143
            4.3.3.1 Methodology and Terminology 143
            4.3.3.2 Averaged Velocity Fields 148
            4.3.3.3 Other Fields 168
    4.4 Sensitivity Tests 182
        4.4.1 Two-dimensional Simulation 184
        4.4.2 Increase of Autoconversion Threshold 185
        4.4.3 Variation of k_D 187

5. CONCLUDING REMARKS AND SUGGESTIONS FOR FURTHER WORK . 191

APPENDIX A - LIST OF SYMBOLS 201

APPENDIX B - COMPUTATION OF SATURATION VAPOUR PRESSURE . . 207

APPENDIX C - THE SHAPIRO FILTER 209

APPENDIX D - PROGRAMMING CONSIDERATIONS 211

REFERENCES 213

BIOGRAPHICAL NOTE 219

LIST OF FIGURES

Figure Page

2.1 A hierarchy of warm rain microphysical parameterizations 26

2.2 The geometry of the grid system and domain . . . 42

2.3 Variation of i and grid spacing Δx with x . . . 45

2.4 Variation of j and grid spacing Δz with z, for the simulation of 14 May 1970 46

3.1 Base-state profiles of relative humidity (RH), equivalent potential temperature (θ_e) and temperature (T) used for the runs in Chapter 3 . . . 76

3.2 Time variation of maximum vertical velocity on the central axis of the cloud for the various models 78

3.3 Time variation of maximum potential temperature perturbation on the central axis of the cloud for the various models 80

3.4 Time variation of maximum rain-water mixing ratio on the central axis of the cloud for the various models 81

4.1 Synoptic situation at 1800 CST, 14 May 1970 . . . 88

4.2 Fields of u (relative to the ground) and ω for 14 May 1970 91

4.3 Base-state profiles used for simulation of the case of 14 May 1970 94

4.4 Initial field of θ' 96

4.5 Position of the model temperature break in time, relative to the ground 100

4.6 Movement of cell updrafts with time relative to the TB 102

4.7 (a) Cloud, rain, and vertical velocity fields on the central plane at 107.3 min. 109

(b) As in (a) but for the side plane at 107.3 min. . 110

Figure Page

4.8 (a) Cloud, rain, and vertical velocity fields on the central plane at 122.1 min. 114

(b) As in (a) but for the side plane at 122.1 min. . 115

4.9 (a) Cloud, rain, and vertical velocity fields on the central plane at 136.8 min. 117

(b) As in (a) but for the side plane at 136.8 min. . 118

4.10 (a) Central plane fields at 136.8 min as in Fig. 4.9 (a) but for 35 km to 75 km behind the TB . . 120

(b) Side plane fields at 136.8 min as in Fig. 4.9 (b) but for 35 km to 75 km behind the TB . . 121

4.11 (a) Cloud, rain, and vertical velocity fields on the central plane at 150.6 min. 123

(b) As in (a) but for the side plane at 150.6 min. . 124

4.12 (a) Cloud, rain, and vertical velocity fields on the central plane at 165.4 min. 125

(b) As in (a) but for the side plane at 165.4 min. . 126

4.13 The v velocity component at 136.8 min. 130

4.14 The u velocity components (relative to the ground) on both planes at 136.8 min. 132

4.15 (a) The field of potential temperature perturbation (θ') on the central plane at 136.8 min. 134

(b) As in (a) but on the side plane at 136.8 min. . . 135

4.16 Schematic streamlines of flow in the central x-z plane relative to cell (5) at 136.8 min. . . 137

4.17 The field of equivalent potential temperature (θ_e) on the central plane at 136.8 min. 139

4.18 The field of pressure perturbation (p') averaged over the domain in y at 136.8 min. 142

4.19 Response versus wavelength for the low-pass, normal-weighting filter used in the x direction . 149

4.20 The field of $\{[u]\}$, relative to the movement of the TB, averaged over 107.3 min to 165.4 min. . . 150

Figure Page

4.21 The field of $\{[w]\}$, averaged over 107.3 min to 165.4 min. 152

4.22 The fields of $\{[u]\}$ and $\{[w]\}$ for 35 km to 75 km behind the TB, averaged over 107.3 min to 165.4 min. 154

4.23 Vertical profile of the Scorer parameter, ℓ^2 . . 159

4.24 Vertical structure of the model vertical velocity (Wm) directly over the TB, and theoretical structures for three different lower boundary conditions (W_2, W_1, W_0). 162

4.25 Time variation of the potential temperature perturbation 5 km behind the TB (θ'), the strongest updraft over the TB (W_{UP}), and the downdraft immediately above that (W_{DOWN}) 165

4.26 The field of $\{[\theta']\}$ averaged over 107.3 min to 165.4 min. 169

4.27 (a) The field of $\dot{\theta}^A$, the apparent source of potential temperature, for 107.3 min to 165.4 min. . . 171

(b) As in (a) but for 35 km to 75 km behind the TB . 172

4.28 The field of $\dot{\theta}^R$, the real source of potential temperature, for 107.3 min to 165.4 min. 173

4.29 The field of $\dot{Q}_V^R$, the real source of water vapour, for 107.3 min to 165.4 min. 176

4.30 The field of $\dot{\theta}^V$, the virtual source of potential temperature, for 107.3 min to 165.4 min. . . 178

4.31 The field of $\dot{\theta}^D$, the diffusive source of potential temperature, for 107.3 min to 165.4 min. . . 179

4.32 The field of $\dot{u}^R$, the real source of the u velocity component, for 107.3 min to 165.4 min. . . . 183

4.33 The time variation of maximum rainfall rates beneath cells (5) and (6) for the two different autoconversion thresholds 188

5.1 Photograph of an approaching severe gust front . 198

LIST OF TABLES

Table Page

3.1 The PGF at the initial time, the vertical velocity at 10 min, and the time and value of the peak vertical velocity, for all the models 83

4.1 Horizontal wavelengths in kilometres of the eigenvalues for the three different lower boundary conditions 160

1. INTRODUCTION

Because of the paucity of observations of mesoscale convective systems in three-dimensional detail, there is a lack of understanding of their structure and dynamics, and particularly of their interactions with the cumulus scale. The recent field program of the GARP Atlantic Tropical Experiment (GATE) was oriented towards observing and understanding scale interactions (Betts, 1974). Yet aside from satellite photos and radar the only observations taken specifically of mesoscale systems (the GATE C scale of 10 to 100 km) were with stacked aircraft, providing good resolution along the flight paths but poor vertical and temporal resolution. Consequently, the best data source for studying the mesoscale continues to be the National Severe Storms Laboratory (NSSL) mesonetwork in Oklahoma. This has provided a number of comparatively well-documented cases of squall lines and other convective systems, with data from radar, surface stations, and serial rawinsonde ascents.

The case of particular interest here occurred on 14 May 1970 and was analyzed by Sanders and Paine (1975). The convective system was associated with the southeastwards advance through the network of a cold front, with lines of thunderstorms developing in the over-running warm air above the frontal surface. The situation and observational results will be described more fully in Chapter 4, but the main, intriguing result was an analyzed mesoscale downdraft/updraft doublet at a level of about 40 kPa (400 mb). The downdraft of about 2 m s^{-1}

was directly over the frontal surface wind shift, and the updraft of 3 m s^{-1} about 25 km towards the northwest. They conjectured, on the basis of an apparent source of water vapour and sink of heat following the mesoscale flow in the downdraft region, that the downdraft was aided by strong evaporative cooling at the tops of initial deep cumulus clouds which were set off by the convergence at the surface wind shift and penetrated into the dry air aloft.

This finding was totally unexpected and somewhat suspect, since the analyses were obtained from balloon soundings into a hostile environment - many of the balloons crashed and the observations (particularly of water vapour) were often of doubtful accuracy. However, further analyses of the same case using slightly different analysis techniques were made by Sanders and Emanuel (1977) with essentially the same results. The analyses also revealed a time evolution of the system which led them to speculate on a characteristic life cycle of such systems; in this, following the mature stage of the strong mesoscale updraft and downdraft, the resultant cloud mass becomes very extensive and eventually disconnected from the surface wind shift and its supply of new "fuel". Recycled air feeds into the residual mesoscale updraft from the rear and the system gradually dies. The estimated typical lifetime of such a system is about ten hours.

In order to test the validity of this speculative view, further studies have and will be made on other cases from the

NSSL archives. Stokes (1977) has already analyzed the case of 26 April 1969 and found a similar downdraft/updraft doublet for the mesoscale system. This case was quite different from that of 14 May in many details. The system was triggered by an approaching cold front but developed its own gust front and propagated ahead of the cold front as a squall line. Also, the downdraft found over the area of the surface wind shift was at a lower level of about 60 kPa and was apparently aided[1] by cooling due to evaporation of a middle cloud deck feeding into the system from the south. Another squall line on 8 June 1966, was found by Fankhauser (1974) to have a downdraft/updraft doublet and is currently being analyzed in detail by researchers at M.I.T.

An alternative way of testing the validity of the observational results and speculations is to run a numerical simulation of a mesoscale convective line like that on 14 May. That is the approach taken in this thesis. We particularly want to see whether a downdraft/updraft doublet develops and whether the system goes through a life cycle as described by Sanders and Emanuel. In order to do this we must be able to resolve with reasonable fidelity both the entire mesoscale system and the cumulus clouds within it, since at least in the downdraft

---

[1] The downdraft was aided in the sense that where it descended moist adiabatically (rather than dry adiabatically) in a conditionally unstable environment there was conversion from potential to kinetic energy rather than the other way round.

region they play an important part. Before outlining the means used to resolve both scales without using too many grid points we will briefly review previous modelling efforts of a related kind.

Most attempts to numerically model deep convective systems have been two-dimensional, relying on the largely two-dimensional structure of observed squall lines. This requires much less computing power than three-dimensional simulations, but does have some major disadvantages. For instance, the geometry leads to stronger compensating subsidence and warming in the environment of simulated cumuli, which in terms of buoyancy results in a lower excess temperature in the updraft and a less vigorous circulation.

The first attempt to numerically model a squall line was by Sasaki (1959). The motivation was apparently Tepper's (1950) conception of a squall line as being triggered by a gravity wave travelling along the warm sector inversion and setting off convection in favourable areas. What Sasaki's model produced was a hydrostatic internal gravity wave propagating away from a frontal-like zone in geostrophic imbalance. No account was taken of any effects of cumulus convection, but a dry and moist case were run with almost no differences. (The moist case had condensation with latent heat release but no precipitation.) Ogura and Charney (1960) ran a similar model but using the anelastic set of equations rather than the hydrostatic set. The two models used horizontal grid spacings of about 20 km and 7 km respectively so had little chance of resolving the shorter wavelengths on the mesoscale, let alone the cumulus scale.

More recent two-dimensional models still used comparatively large grid spacings. For example, Schlesinger's (1973) model had spacings of 3.2 km in the horizontal and 700 m in the vertical, with a large model domain of 172.8 km horizontally. On the other hand, Hane (1973) used a much smaller spacing of 400 m in the horizontal and vertical but a horizontal domain of only 35 km. Because of the limited domain the interesting results he obtained apply more to the scale of a single thunderstorm than an entire squall line. One result of particular interest to us was the periodic regeneration of cells at the leading edge of a pool of cold air which developed beneath the storm. The period was about thirty minutes; Sanders and Emanuel (1977) found a periodic development of radar echo lines at intervals of forty-five minutes to an hour in the 14 May case.

In an approach similar to the one we will present, Yamasaki (1975) used a <u>nonuniform</u> horizontal grid in a two-dimensional axisymmetric model. The grid spacing was 200 m within a radius of 20 km and increased steadily from there out to 150 km, beyond which it was constant at 25 km out to the domain edge at a radius of 500 km. In the vertical the grid spacing was 300 m up to a model lid at 5.4 km. While the simulation was oriented towards a tropical cyclone development, it did show how the cumulus convection in the central zone of good resolution interacted with the larger scales, and illustrated the utility of such a grid system in reducing the amount of computation for a scale-interaction problem.

Only very recently have fully three-dimensional simulations been attempted for deep convection (in shear, since a two-dimensional axisymmetric model can only be used when there is no vertical wind shear). Some examples for isolated clouds are Wilhelmson (1974), Klemp and Wilhelmson (1977), and Schlesinger (1975 and 1977). Moncrieff and Miller (1976) successfully simulated a tropical squall line using a non-hydrostatic model formulated in pressure co-ordinates, over a domain only 29 km square with horizontal grid spacings of 1 km, and 80 kPa deep with the relatively large vertical grid spacing of 10 kPa. A surface cold pool formed during the rainout of the first simulated cell. Its leading edge propagated westwards (faster than the ambient low-level easterlies) and triggered the development of new cells at intervals of about 35 min. The scale of the system was much smaller than that of 14 May, with the cells reaching their peak amplitudes only a few kilometres behind (to the east of) the surface wind shift and the entire width of the system being only about 20 km. There was no evidence of any downdraft over the surface wind shift; most of the downward motion apparently occurred during the rain-out stages of the cells.

Rather than using a very fine grid to be able to resolve the cumulus elements one can use a much coarser grid to explicitly model the larger scale flow and then parameterize the effects of the convection. For example, Brown (1974) used a steady-state one-dimensional plume model at each horizontal grid point (spaced 25 km apart). To calculate the effects of the cumuli the mass flux into the clouds was required; Brown took this as a constant times the large-scale upward flux at cloud base. The results of the runs were very sensitive to the value of this constant, suggesting that perhaps the parameterization was not appropriate and the model should somehow determine the mass flux itself. For a similar model, Kreitzberg and Perkey (1976) determined the flux by equating the hydrostatic pressure at the base of the plume with that in the environment, taking into account the effect of compensating subsidence on the environmental temperature profile. While the approach may be more sophisticated, it is not necessarily valid; observational verification of any such relationship should be made. However, using that model Kreitzberg and Perkey (1977) managed to simulate the development from a weak mesoscale updraft, with parameterized convective release of potential instability, to a stronger mesoscale updraft in a hydrostatically neutral atmosphere with almost no convection.

In any case, the method of parameterizing the effects of cumulus convection cannot be applied to a system on the scale that we are considering. The mesoscale updraft and downdraft are only about 25 km apart which necessitates a horizontal grid spacing of at most 5 km. For this spacing the usual assumptions of small fractional coverage of cumulus elements and some kind of quasi-equilibrium between the cumulus and the mesoscale forcing are obviously invalid. The scale separation (in both time and space) between the cumulus scale and the mesoscale just is not enough.

So the approach taken in this thesis is to explicitly model both the cumulus scale and the mesoscale. By using a nonuniform horizontal grid in the direction transverse to the convective line we will be able to have good resolution in the region where the convection is expected to be of importance, <u>and</u> a large enough domain to encompass all of the mesoscale system, without requiring too many grid-points. Further, to partially circumvent the problems of two-dimensional models, we will use a quasi-three-dimensional model having three grid-points and assumed periodicity in the direction along the line. The specific details of the model design are discussed in Chapter 2. In Chapter 3 the model is validated and the effects of various geometrical configurations tested by comparing the simulation of an isolated cumulus cloud with that of Soong and Ogura (1973).

Chapter 4 starts with a summary of the observational studies on the case of 14 May 1970, then presents the results of a simulation spanning more than four hours. A representative period of an hour is chosen for more detailed study; averages over that period are computed to reveal the mesoscale fields and show the manner in which the smaller scales affect the mesoscale. Finally, the results of a two-dimensional simulation and of sensitivity tests on the microphysical and diffusion parameterizations are given.

Chapter 5 consists of concluding remarks and suggestions for further work. Four appendices follow, with a list of symbols used, and descriptions of some of the more exotic numerical and programming details.

2. NUMERICAL MODEL DESIGN

Before describing the model in detail, we can summarize its main features as follows:

(1) It uses the deep anelastic (quasi-Boussinesq) set of equations.

(2) The microphysical parameterizations follow Kessler (1969), with the water split into the three categories of vapour, cloud, and rain; there is no ice.

(3) Subgrid diffusion is explicitly parameterized using a variable diffusion coefficient which is a function of the local deformation and static stability.

(4) The geometry of the model can be either two-dimensional and slab-symmetric (in the x-z plane), or three-dimensional with just a small number of grid-points in the y direction and assumed periodicity.

(5) Stretched co-ordinates can be used in the x and z directions for best resolution in the most interesting regions - in the middle of the model and near the ground.

(6) For the simulation of the 14 May system the domain size is 150 km in x and 15 km in z. There are 100 grid-points in x and 31 in z; stretching allows the grid spacings to be as low as 400 m in x and 250 m in z. For the three-dimensional run there are just three grid-points in the y direction over a width of 12 km.

(7) The finite difference equations use centred time differencing (leapfrog) except for the diffusive terms, and cen-

tred space differencing. The advective terms are in quadratically-conservative flux form.

(8) The time-step is usually about ten seconds.

(9) There is no Coriolis force.

2.1 Mathematical Definition of the Model

This section describes the model only in mathematical terms. All finite difference equations and computational details will be left to Section 2.2.

2.1.1 Dynamics and Thermodynamics

The model uses the deep anelastic or quasi-Boussinesq set of equations; these are non-hydrostatic but have acoustic waves filtered out. In their derivation by Ogura and Phillips (1962) an isentropic base- or reference-state was assumed; here we use a non-isentropic base-state which gives better accuracy - deviations from it are smaller - but, as noted by Dutton and Fichtl (1969), results in energetic inconsistency (energy equations cannot be formed).

Following Schlesinger (1975) we define a transformed non-dimensional pressure variable P as

$$P = \frac{\overline{T}}{\overline{\theta}\,\overline{p}}\, p' \qquad (2.1)$$

Here an overbar denotes a base state variable (a function of z

alone), and a prime a perturbation or deviation from that. T is temperature, θ potential temperature, and p pressure. For a full list of symbols see Appendix A.

The three equations of motion are then

$$\begin{aligned}\bar{\rho}\frac{\partial u}{\partial t} &= -R_d\bar{\theta}\bar{\rho}\frac{\partial P}{\partial x} - \nabla\cdot(\bar{\rho}u\underset{\sim}{V}) + F_x \\ &= -R_d\bar{\theta}\bar{\rho}\frac{\partial P}{\partial x} + \bar{\rho}A\end{aligned} \tag{2.2}$$

$$\begin{aligned}\bar{\rho}\frac{\partial v}{\partial t} &= -R_d\bar{\theta}\bar{\rho}\frac{\partial P}{\partial y} - \nabla\cdot(\bar{\rho}v\underset{\sim}{V}) + F_y \\ &= -R_d\bar{\theta}\bar{\rho}\frac{\partial P}{\partial y} + \bar{\rho}B\end{aligned} \tag{2.3}$$

$$\begin{aligned}\bar{\rho}\frac{\partial w}{\partial t} &= -R_d\bar{\theta}\bar{\rho}\frac{\partial P}{\partial z} - \nabla\cdot(\bar{\rho}w\underset{\sim}{V}) + F_z + g\bar{\rho}\left(\frac{\theta'}{\bar{\theta}} + aQ_v' - (Q_c+Q_R)\right) \\ &= -R_d\bar{\theta}\bar{\rho}\frac{\partial P}{\partial z} + \bar{\rho}C\end{aligned} \tag{2.4}$$

The three velocity components of the vector $\underset{\sim}{V}$ are u, v and w in the x, y and z directions respectively. ∇ is the three-dimensional divergence operator ($\frac{\partial}{\partial x}\underset{\sim}{i} + \frac{\partial}{\partial y}\underset{\sim}{j} + \frac{\partial}{\partial z}\underset{\sim}{k}$). The forces per unit volume - F_x, F_y, and F_z - will be discussed in Section 2.1.3. The symbols A, B, and C are used for convenience to represent the non-pressure accelerations in x, y, and z.

Note that the vertical equation of motion (2.4) includes a buoyancy due to the potential temperature perturbation ($\theta'/\bar{\theta}$), a water vapour buoyancy arising from the virtual temperature effect (aQ_V', where a is a constant and Q_V is the mixing ratio of water vapour), and a liquid-water drag due to cloud and rain (of mixing ratios Q_C and Q_R respectively).

There is no Coriolis force - it is not allowed because of the symmetry assumption in the y direction (see Section 2.2.1). This should not seriously affect the 14 May simulation since Sanders and Emanuel (1977) showed the Coriolis accelerations to be mostly small compared with other accelerations. In other cases Coriolis effects may be important.

The equation for mass continuity is

$$G \equiv \frac{1}{\bar{\rho}} \frac{\partial \rho}{\partial t} = \frac{1}{\bar{\rho}} \nabla \cdot (\bar{\rho} \underset{\sim}{V}) \tag{2.5}$$

where the net divergence (G) is retained on the left-hand side for computational purposes, even though it is identically zero in the exact anelastic equations.

We take the local time derivative of (2.5) and combine it with the spatial derivatives of the three equations of motion to obtain an elliptic diagnostic equation for P:

$$\begin{aligned} &\frac{\partial^2 P}{\partial x^2} + \frac{\partial^2 P}{\partial y^2} + \frac{1}{R_d \bar{\theta} \bar{\rho}} \frac{\partial}{\partial z}\left(R_d \bar{\theta} \bar{\rho} \frac{\partial P}{\partial z}\right) \\ &= \frac{1}{R_d \bar{\theta} \bar{\rho}} \left[\frac{\partial (\bar{\rho} A)}{\partial x} + \frac{\partial (\bar{\rho} B)}{\partial y} + \frac{\partial (\bar{\rho} C)}{\partial z} \right] - \frac{1}{R_d \bar{\theta}} \frac{\partial G}{\partial t} \end{aligned} \tag{2.6}$$

The expression on the right-hand side constitutes a forcing function for the pressure field, and includes a correction term in $\partial G/\partial t$ to minimize the computational value of the net divergence.

The thermodynamic equation is

$$\frac{\partial \theta'}{\partial t} = -\frac{1}{\bar{\rho}}\nabla\cdot(\bar{\rho}\,\theta'\underset{\sim}{V}) - w\frac{\partial \bar{\theta}}{\partial z} + \frac{1}{\bar{\rho}}\nabla\cdot(\bar{\rho}\,K_H\nabla\theta') \quad (2.7)$$

+ net latent heating rate

where K_H is the eddy diffusion coefficient for heat (diagnosed as a function of deformation and static stability, as described in Section 2.1.3). Note that only perturbations from the base-state of the potential temperature are diffused - the implication is that the base-state profile is maintained by some unspecified large-scale (compared to the model) process, so should not be smoothed out by the much-smaller-scale diffusion. (The same reasoning is later applied to water vapour and the u velocity component.) However, this formulation really means that the second derivative in the vertical of the base-state profile, rather than the profile itself, is left untouched. Because of unsmoothness in the 14 May profile of $\overline{Q}_V$ this resulted in some problems in the numerical simulation, as will be shown in Section 4.3.3.3.

Computation of the net latent heating rate by condensation and evaporation will be discussed in Section 2.2.2.

2.1.2 Water and Microphysics

To include in detail all the microphysical processes occurring in real clouds would require an inordinate amount of computer time for this model. We must simplify them.

The first simplification we can make is to eliminate all ice processes (they are not well understood in any case) and hope that the results will not be too badly affected. The remaining processes controlling the spectrum of water drops include cloud condensation nucleii (CCN) activation and deactivation, diffusional transfer between water vapour and water drops, drop-drop stochastic coalescence, drop breakup, and differential fall velocities. Fig. 2.1 shows a hierarchy of models which have been used to handle these processes, either explicitly or implicitly, ranging from the very complicated (A) to the simplest (D).

Models A and B are still too complex to be used by us. In any case Clark (1973) found that consideration of CCN in modelling cloud condensation and evaporation made little difference in the dynamics, and Yau (1977) found little difference in the results for the raindrop spectrum between models of type B and C.

Even model C requires too much computer storage and calculation - for instance, Yau (1977) used ten size categories to represent the raindrop spectrum. We must use model D and <u>assume</u> that the raindrop spectrum follows the Marshall-Palmer (1948) distribution. This distribution is a good fit to

A.

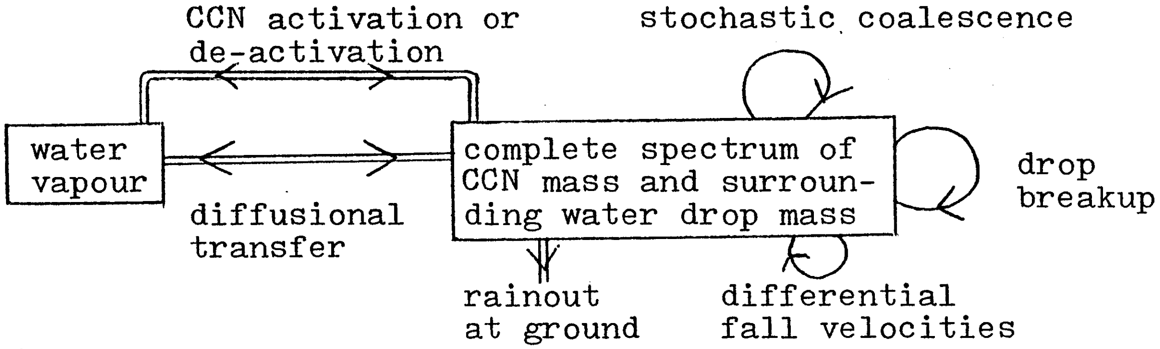

<u>Example</u>: Clark (1973) - no drop breakup or rainout.

B.

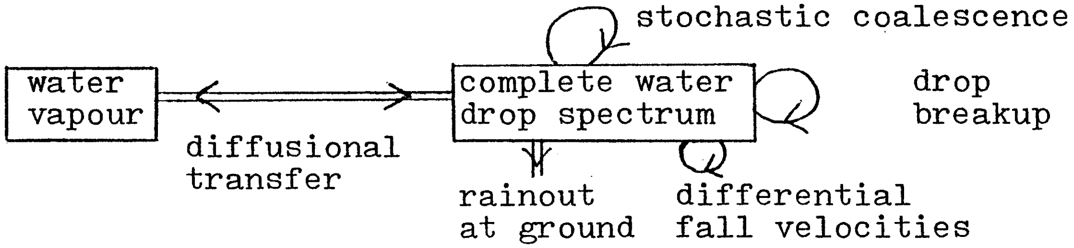

<u>Examples</u>: Clark (1976) - spectrum modelled as sum of two log-normal functions with six total parameters. No drop breakup or differential fall velocities.
Yau (1977) - S model, used in a kinematic model without water vapour.

Figure 2.1. A hierarchy of warm rain microphysical parameterizations. The full arrows ($\Longrightarrow$) represent processes which transfer water from one category to another. The single arrows ($\longrightarrow$) represent self-interaction processes which change the distribution within a category.

C.

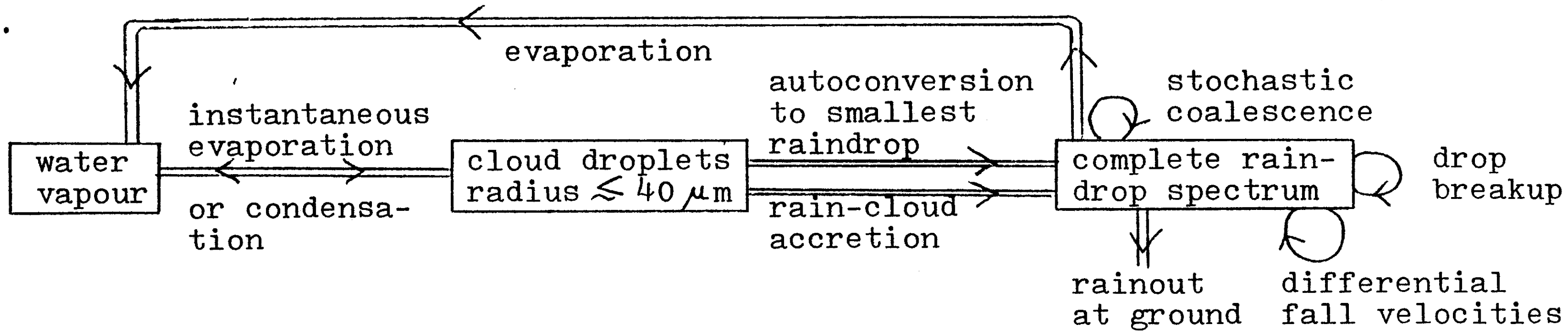

Example: Yau (1977) - P model. Ice microphysics were also included.

D.

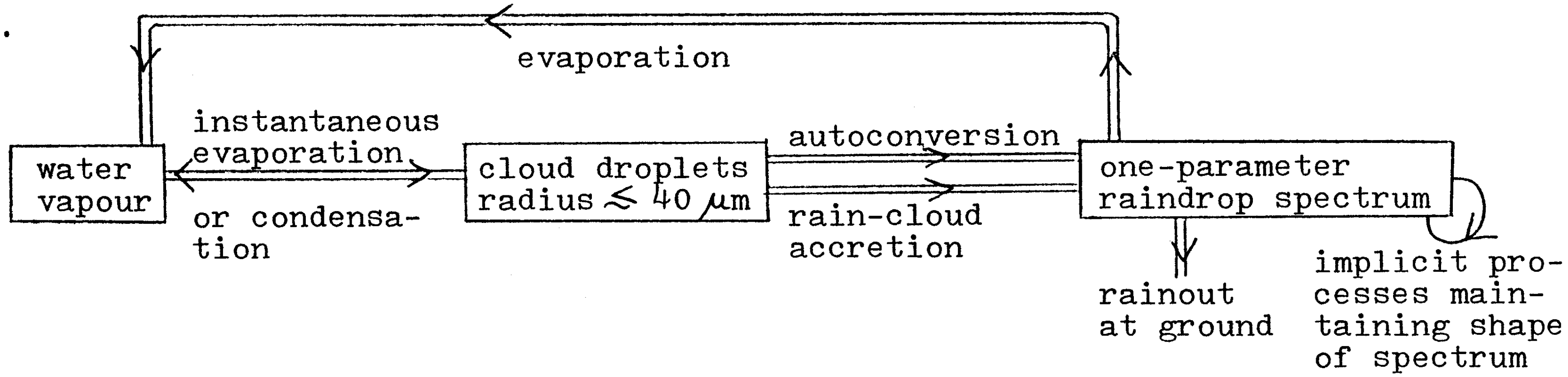

Examples: Kessler (1969).
Clark (1973) - without rain.
Manton and Cotton (1977).

Figure 2.1 (continued)

averaged observations of spectra, but not so good for individual observations (Mason and Andrews, 1960). It has the form

$$N(D) = N_o e^{-\lambda D} \tag{2.8}$$

where $N(D)\delta D$ is the number of raindrops per unit volume of diameter in the range $(D, D+\delta D)$, and N_o is the intercept at $D = 0$. Observations averaged over many types of rain indicate that N_o is approximately constant at 10^7 m^{-4}; the parameter λ then depends only on the amount of rain per unit volume.[1]

Based on this distribution, we have the following expressions for accretion of cloud water by rain, evaporation of rain, and the terminal velocity for rain (a mass-weighted mean over the distribution), adapted from Kessler (1969):

$$\left.\frac{dQ_R}{dt}\right|_{\text{accretion}} = 0{\cdot}294\, \rho_o^{\frac{1}{2}}\, N_o^{\frac{1}{8}}\, \bar{\rho}^{\frac{3}{8}}\, Q_c\, Q_R^{\frac{7}{8}} \tag{2.9}$$

$$\left.\frac{dQ_R}{dt}\right|_{\text{evaporation}} = -1{\cdot}72 \times 10^{-4}\, N_o^{\frac{7}{20}}\, \bar{\rho}^{\frac{13}{20}}\, (Q_{VS} - Q_V)\, Q_R^{\frac{13}{20}} \tag{2.10}$$

$$W_R = -92{\cdot}0\, \rho_o^{\frac{1}{2}}\, N_o^{-\frac{1}{8}}\, \bar{\rho}^{\frac{3}{8}}\, Q_R^{\frac{1}{8}} \tag{2.11}$$

---

[1] Manton and Cotton (1977) postulate that for high rainfall rates drop breakup is the dominant process controlling the spectrum; they use a constant λ (an inverse length scale related to a characteristic drop size) and have N_o vary with the density of rain.

All units are in the International System of Units (American Meteorological Society, 1974) - the base units being the metre, kilogramme, second, and kelvin. ρ_0 is the mean-sea-level density of air (1.225 kg m^{-3}). The saturation mixing ratio Q_{VS} is given (to a good approximation) by

$$Q_{VS} = \frac{0{\cdot}622}{\bar{p}} \, e_{SW}(T) \tag{2.12}$$

where the saturation vapour pressure over water, e_{SW}, is computed as explained in Appendix B.

The formula for autoconversion - the production of rain-sized drops by stochastic coalescence of cloud droplets with themselves - is

$$\left.\frac{dQ_R}{dt}\right|_{\text{autoconversion}} = k_a \left(Q_c - \frac{\rho_{CT}}{\bar{\rho}}\right) H\left(Q_c - \frac{\rho_{CT}}{\bar{\rho}}\right) \tag{2.13}$$

where H is the Heaviside function, defined by $H(x) = 0$ for $x < 0$ and $H(x) = 1$ for $x \geqslant 0$.

The autoconversion rate constant, k_a, used in all runs is 10^{-3} s^{-1}. The autoconversion threshold, ρ_{CT}, below which no autoconversion can take place, was taken to be 0.5 g m^{-3} by Kessler. Our choice is based on the work of Manton and Cotton (1977). Manton (1974) had shown that the effect of coalescence on the cloud droplet distribution became comparable with that of condensation for droplet radii larger than about 10 μm. Assuming monodisperse droplets, this occurs for a cloud-water density of

$$\rho_{cT} = 4 \cdot 189 \times 10^{-6} \; N_c \qquad (2.14)$$

where N_c is the number of cloud droplets per cubic metre. For a typical N_c of 240 m^{-3} the threshold is 1.005 g m^{-3}, the value used for most of the runs.

The numbers chosen for k_a and ρ_{cT} have little physical basis, since the autoconversion rate should really depend on the entire life history of a parcel of cloud droplets, but fortunately they are not particularly sensitive parameters. Yau (1977) found that his kinematic model was remarkably insensitive to variations in k_a over two orders of magnitude (10^{-2} s^{-1} to 10^{-4} s^{-1}) and to a change in ρ_{cT} from 0.7 g m^{-3} to 0.0 g m^{-3}. The explanation is apparently that autoconversion is only important for small rain-water densities; the accretion quickly dominates as the rain-water density increases. We can see that by comparing the two rates for a typical air density of 1.0 kg m^{-3} and $k_a = 10^{-3}$ s^{-1}. For a zero autoconversion threshold the autoconversion and accretion rates are both proportional to Q_c and are the same for a rain-water density of only 0.13 g m^{-3}; above this the accretion rate dominates. So a change in the autoconversion threshold would act mainly to delay the initial formation of rain; unless this time is critical the total amount of rain produced will not be affected much. The results of a sensitivity test on the autoconversion threshold, given in Section 4.4.2, support this contention.

We can now write the continuity equations for water vapour (of mixing ratio Q_V), cloud-water (Q_C) and rain-water (Q_R):

$$\frac{\partial Q_V}{\partial t} = -\frac{1}{\bar{\rho}}\nabla\cdot(\bar{\rho}\, Q_V \underset{\sim}{V}) + \frac{1}{\bar{\rho}}\nabla\cdot(\bar{\rho} K_H \nabla Q_V') \tag{2.15}$$

+ cloud evaporation + rain evaporation - condensation

$$\frac{\partial Q_C}{\partial t} = -\frac{1}{\bar{\rho}}\nabla\cdot(\bar{\rho}\, Q_C \underset{\sim}{V}) + \frac{1}{\bar{\rho}}\nabla\cdot(\bar{\rho} K_H \nabla Q_C) \tag{2.16}$$

+ condensation - autoconversion - accretion

$$\frac{\partial Q_R}{\partial t} = -\frac{1}{\bar{\rho}}\nabla\cdot(\bar{\rho}\, Q_R (\underset{\sim}{V} + \underset{\sim}{k} W_R)) \tag{2.17}$$

+ autoconversion + accretion - rain evaporation

The diffusion coefficient K_H is diagnosed as explained in Section 2.1.3. Just as for the potential temperature, we do not diffuse the base-state profile of water vapour. No diffusion at all is applied to rain-water; the rain-drops are assumed to have enough inertia that they are not affected by subgrid-scale turbulence. The cloud moves with the air; the rain falls relative to it with terminal velocity W_R.

As noted in Fig. 2.1, any cloud-water finding itself in subsaturated air is evaporated until it is all gone or saturation is reached, and more cloud is condensed whenever the air becomes supersaturated. The computational details will be discussed in Section 2.2.2.

2.1.3 Diffusion

Lilly (1962) derived a formula for the subgrid eddy diffusion coefficient of momentum, K_M, as

$$K_M = (k_D \Delta)^2 \sqrt{|D|^2 - d \frac{g}{\theta}\left(\frac{\partial \theta}{\partial z} - \frac{d\theta}{dz}\bigg|_{ad}\right)} \tag{2.18}$$

where k_D is a coefficient of order unity, Δ is a measure of the grid spacing, $|D|$ is the magnitude of the three-dimensional deformation, $d \equiv K_H/K_M$ is an assumed fixed ratio between the eddy coefficients of heat and momentum, and $d\theta/dz|_{ad}$ is the moist or dry adiabatic lapse rate. (Lilly only considered the dry case.)

It can be seen that K_M (with units $m^2\ s^{-1}$) is the product of a squared length scale and the root-mean-square of two inverse time scales - deformation and an imaginary Brunt-Väisälä frequency. This formula is similar to one derived by Hill (1974) on dimensional considerations alone, but he used the <u>sum</u> of the inverse time scales rather than the root-mean-square.

The formula can also be written as

$$K_M = (k_D \Delta)^2 |D| \sqrt{1 - d \frac{\frac{g}{\theta}\left(\frac{\partial \theta}{\partial z} - \frac{d\theta}{dz}\big|_{ad}\right)}{|D|^2}} \tag{2.19}$$

in which the coefficient is based on the deformation time-scale but with a correction factor depending on a type of Richardson number:

$$R_i = \frac{\frac{g}{\theta}\left(\frac{\partial\theta}{\partial z} - \frac{d\theta}{dz}\Big|_{ad}\right)}{|D|^2} \tag{2.20}$$

This is seen to enhance the eddy diffusion under unstable conditions of negative R_i, and decrease it for stable conditions. Lilly used $d = 1.0$ and took K_M to be zero when the factor under the square-root was negative, i.e., when the Richardson number was greater than unity. Hill also took K_M to be zero under stable conditions, but defined by a Richardson number greater than 0.25. (Miles (1961) and Howard (1961) proved on the basis of linear theory that when R_i is greater than 0.25 there is no net energy source available for the generation of turbulence.)

In the application of (2.18) to this model the following choices have been made:

(1) For simplicity, the ratio d is taken as 1.0. (It could arguably be larger in the case of buoyancy-driven turbulence where heat is not just a passive contaminant.)

(2) The coefficient k_D is set to 0.42 for the 14 May simulation. Steiner (1973) also used this value, based on comparison of his model results with similarity theory, although he did set $d = 3.0$. Some sensitivity tests on k_D will be discussed in Section 4.4.3.

(3) For both two- and three-dimensional runs the grid-spacing scale, Δ, is taken as the geometric mean of the spacings in x and z, i.e., $\Delta = (\Delta x \Delta z)^{1/2}$. The spacing in the y

direction, Δy, is not taken into account because of the coarse resolution and small number of grid-points to be used in y; the parameterized turbulence would be expected to be controlled mostly by flow in the x-z plane.

(4) The square-root correction factor is only included in the case of static instability; buoyancy enhancement of the turbulence is allowed, but not degradation.

The expression for the three-dimensional deformation used in the above formulae, in tensor notation, is

$$|D|^2 = \frac{1}{2}\left(\frac{\partial u_i'}{\partial x_j} + \frac{\partial u_j'}{\partial x_i}\right)^2 \tag{2.21}$$

where deviations from the base state are used for the same reason as before - we are considering small-scale effects only. Expanded into its components, this expression is

$$\begin{aligned} |D|^2 = {} & 2\left[\left(\frac{\partial u'}{\partial x}\right)^2 + \left(\frac{\partial v}{\partial y}\right)^2 + \left(\frac{\partial w}{\partial z}\right)^2\right] \\ & + \left(\frac{\partial u'}{\partial y} + \frac{\partial v}{\partial x}\right)^2 + \left(\frac{\partial u'}{\partial z} + \frac{\partial w}{\partial x}\right)^2 + \left(\frac{\partial v}{\partial z} + \frac{\partial w}{\partial y}\right)^2 \end{aligned} \tag{2.22}$$

(Now only the u velocity component needs a prime on it, since $\overline{w} \equiv \overline{v} \equiv 0$.)

Using K_M, the frictional forces per unit mass are (Lilly, 1962):

$$F_i = \overline{\rho}\,\frac{\partial}{\partial x_j}\left(K_M\left(\frac{\partial u_i'}{\partial x_j} + \frac{\partial u_j'}{\partial x_i}\right)\right) \tag{2.23}$$

in tensor notation, or in expanded form:

$$F_x = \bar{\rho}\left[\frac{\partial}{\partial x}\left(K_M\left(\frac{\partial u'}{\partial x}+\frac{\partial u'}{\partial x}\right)\right)+\frac{\partial}{\partial y}\left(K_M\left(\frac{\partial u'}{\partial y}+\frac{\partial v}{\partial x}\right)\right)+\frac{\partial}{\partial z}\left(K_M\left(\frac{\partial u'}{\partial z}+\frac{\partial w}{\partial x}\right)\right)\right] \quad (2.24)$$

$$F_y = \bar{\rho}\left[\frac{\partial}{\partial x}\left(K_M\left(\frac{\partial v}{\partial x}+\frac{\partial u'}{\partial y}\right)\right)+\frac{\partial}{\partial y}\left(K_M\left(\frac{\partial v}{\partial y}+\frac{\partial v}{\partial y}\right)\right)+\frac{\partial}{\partial z}\left(K_M\left(\frac{\partial v}{\partial z}+\frac{\partial w}{\partial y}\right)\right)\right] \quad (2.25)$$

$$F_z = \bar{\rho}\left[\frac{\partial}{\partial x}\left(K_M\left(\frac{\partial w}{\partial x}+\frac{\partial u'}{\partial z}\right)\right)+\frac{\partial}{\partial y}\left(K_M\left(\frac{\partial w}{\partial y}+\frac{\partial v}{\partial z}\right)\right)+\frac{\partial}{\partial z}\left(K_M\left(\frac{\partial w}{\partial z}+\frac{\partial w}{\partial z}\right)\right)\right] \quad (2.26)$$

The diffusion terms for potential temperature, water vapour, and cloud-water have already been given in their respective prediction equations, in terms of the eddy diffusion coefficient for heat, K_H, obtained by simply setting $K_H = d * K_M$.

2.1.4 Boundary Conditions

The lower boundary is rigid, with no flux of heat or moisture across it:

$$W = \frac{\partial \theta'}{\partial z} = \frac{\partial Q_v'}{\partial z} = \frac{\partial Q_c}{\partial z} = \frac{\partial Q_R}{\partial z} = \frac{\partial K_M}{\partial z} = 0$$

However, it is not free-slip. There is a modelled stress exerted by the ground on the air at the lowest level for which horizontal velocity components are computed (about 250 m). This stress is obtained by expressing it in terms of a drag coefficient and an imaginary wind at the anemometer level, 10 m above the ground. This wind is estimated by equating the drag stress with a stress computed from K-theory using the wind shear between the anemometer level and the first computed level. The procedure is similar to that used by Kasahara and Washington (1967) for a general circulation model; it is described fully in Section 2.2.2.

The upper boundary is rigid and free-slip; with again no fluxes of heat and moisture across it:

$$\frac{\partial u}{\partial z} = \frac{\partial v}{\partial z} = w = \frac{\partial \theta'}{\partial z} = \frac{\partial Q_v'}{\partial z} = \frac{\partial Q_c}{\partial z} = \frac{\partial Q_R}{\partial z} = \frac{\partial K_M}{\partial z} = 0$$

The lateral boundary conditions in the y direction are that there is periodicity with a period of WIDTH.

The lateral boundary conditions in x for heat and moisture are either zero gradient:

$$\frac{\partial \theta'}{\partial x} = \frac{\partial Q_v'}{\partial x} = \frac{\partial Q_c}{\partial x} = \frac{\partial Q_R}{\partial x} = 0$$

or zero perturbation:

$$\theta' = Q_v' = Q_c = Q_R = 0$$

For the isolated cumulus cloud simulations in Chapter 3 the zero gradient boundary conditions are used.

For the 14 May simulation the outflow boundary on the left uses zero gradient conditions and the inflow boundary on the right uses zero perturbation conditions.

The lateral boundary conditions in x on momentum are:

$$w = v = \frac{\partial u}{\partial x} = 0$$

since the boundaries are expected to be far enough from the main activity that the flow will be nearly horizontal and two-dimensional.

By the same reasoning, we expect that the pressure at these boundaries will be nearly hydrostatic - the boundary condition is that it be exactly so. The perturbation pressure is set to zero at all points in y at the top right of the domain, and to a suitable constant at the top left of the domain, such that the resulting net pressure gradient integrated in z and in y does not accelerate the air in the domain as a whole.

An alternative boundary condition would be $\partial P/\partial x = 0$. However, this results in a singular system of equations when solving for the pressure - the solution is only unique to within a constant. The algorithm being used to solve the equations unfortunately always chooses a constant which is large in comparison with the variation of pressure over the domain, thus degrading the accuracy of the solution.

2.2 The Numerical Model

We will now consider the numerical aspects of integrating the finite-difference version of the model defined mathematically in the first part of this chapter. Section 2.2.1 describes the domain of integration and the system of grid-points within it at which the model variables are defined. Section 2.2.2 describes how the time integration is actually performed.

It includes a list of the operations carried out sequentially for each time-step, and most of the required finite-difference equations. (Computer programming details are considered in Appendix D.) Only the three-dimensional model will be described - the two-dimensional model is an obvious simplification of this.

2.2.1 The Domain and Grid System

The radar cross-sections in Sanders and Emanuel (1977) for the convective system of 14 May give us an idea of the space scales of the type of system we wish to simulate. Radar-detectable precipitation is confined to within a range of 10 km to 60 km behind the surface wind shift, and reaches no higher than 12 km. The strongest echoes, over 60 dbz, occur mostly about 30 km behind the surface wind shift, indicating that the strongest convective activity is ahead of that. Horizontal radar scans show the convective cells to be quasi-uniformly spaced at intervals of about 12 km along the line.

In order to retain the mesoscale system within the interior of the domain while minimizing effects from the lateral boundaries we need a domain LENGTH (in x) of about 150 km. A domain HEIGHT of 15 km should be sufficient to keep the cells from penetrating too near the top. For the y direction (along the line) it seems reasonable to assume periodicity over a domain WIDTH of about 12 km.

There are some observations to guide us in the choice of grid spacings: Ackerman (1967) found significant fluctuations on scales of 200-900 m inside cumulus clouds; from aircraft observations Kyle _et al_ (1976) reported thunderstorm updraft radii at about 2000 m above cloud base to be from 900-2300 m. To resolve such features we want a horizontal grid spacing of a few hundred metres or smaller, and a comparable vertical spacing.

Suppose, then, that we take a domain of 150 km x 12 km x 15 km with constant $\Delta x = \Delta y = \Delta z = 300$ m. That would require one million grid-points - a totally unrealistic number even for today's computers. To bring the number down to a manageable figure over the same domain size we need to use some sort of nonuniform grid spacing so that there is good resolution in the region of most interest (about a 30 km span in x where the convection is most important), and coarse resolution elsewhere.

One possibility is to use a nested grid system as did Walsh (1974) for a two-dimensional hydrostatic sea-breeze model, and Walsh (1976) for a two-dimensional non-hydrostatic cumulus model. This has the advantage of allowing longer time-steps for the coarser sections of the grid, but disadvantages of more complicated programming and the possibility of numerical instabilities where the nested grids match.

The other approach is to use stretched co-ordinates so that the grid spacings increase smoothly away from the region of finest resolution. Kálnay de Rivas (1971) has shown that, provided the transformation function used to stretch the co-ordinates is suitably smooth, the extra errors due to taking centred finite differences over a nonuniform grid are only of second-order.[1] The disadvantage is that to satisfy linear stability criteria the time-step used for the entire grid depends on the smallest grid spacing so can be quite short. This model is designed so that stretched co-ordinates can be used in the x and z directions.

The simplest representation in the y direction is to use only one grid-point - we then have a two-dimensional, slab-symmetric model. Such models are usually applied to squall lines on the basis of their obvious two-dimensional character. However, it is only the <u>mesoscale</u> structure which is two-dimensional - the individual thunderstorm cells comprising the line are fully three-dimensional. In modelling these cells, slab-symmetric models have the well-known problems of too-strong compensating subsidence because of the geometry, resulting in less vigorous cells, and blocking of the mesoscale flow by the cells because there can be no flow around them.

The simplest possible three-dimensional model has only two grid-points in the y direction - for a spacing of 6 km if we are using a WIDTH of 12 km. For about the same computational effort we can have three grid-points for a spacing of 4 km, and use symmetry so that we need compute at only two of the grid-

---

[1] Although Yamasaki's (1975) nonuniform horizontal grid implicitly used a function having a discontinuous first derivative there were no evident numerical problems.

points. (The symmetry assumption is used only to reduce the computation - it implies nothing about the structure of actual squall lines. One consequence of the assumption is that there can be no mean v wind component - since v is antisymmetric about the central x-z plane of the model - and therefore no Coriolis force which would produce a mean v.) This model setup does <u>alleviate</u> the two problems mentioned above - subsidence can now occur in a third dimension and the air can now flow around a cell - but is still an extremely crude representation of the third dimension. (Chapter 3 will compare model runs for the slab-symmetric and simple three-dimensional setups.)

A staggered grid system is used in order that derivatives may be computed mostly over a single grid step, minimizing space truncation error. A staggered grid is also necessary so that the finite-difference analogue of the diagnostic pressure equations uses only three pressure points in each direction, and not five. The domain is constructed of grid boxes like the one depicted in Fig. 2.2 (a). The pressure is computed in the interior of the box, and velocities at the centres (in stretched space) of its six faces. The quantities θ', Q_V, Q_C, and Q_R are all computed at the same points as the pressure. The diffusion coefficient, K_M, is diagnosed at the same points as the vertical velocity, W. Note that the usual association of grid co-ordinates (i, j, k) with space co-ordinates (x, y, z) has been twisted around to (i, k, j) for computer programming convenience.

The model can also be considered to consist of a number of

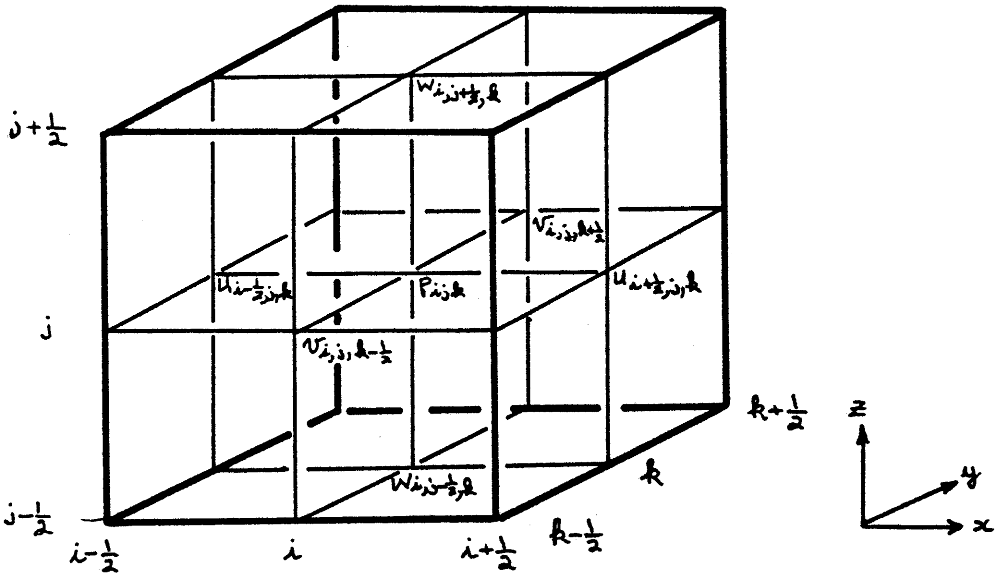

(a) A representative grid box.

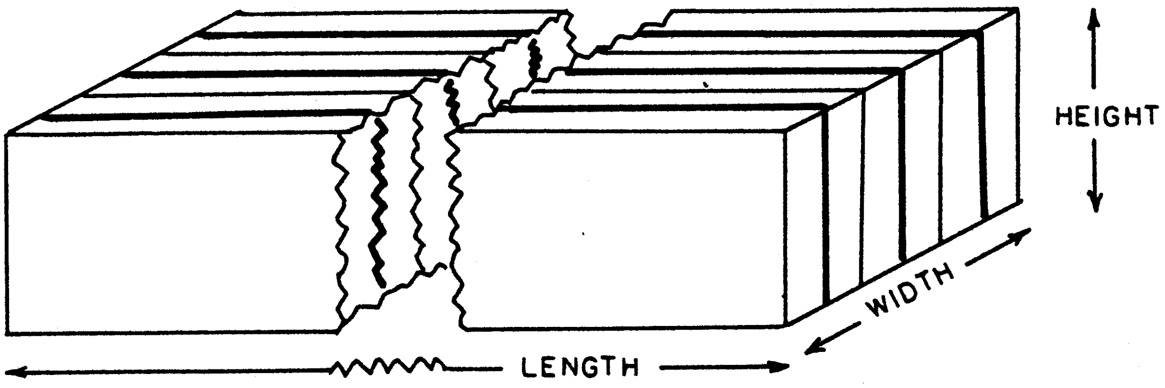

(b) An overall view of the domain (compressed in x).

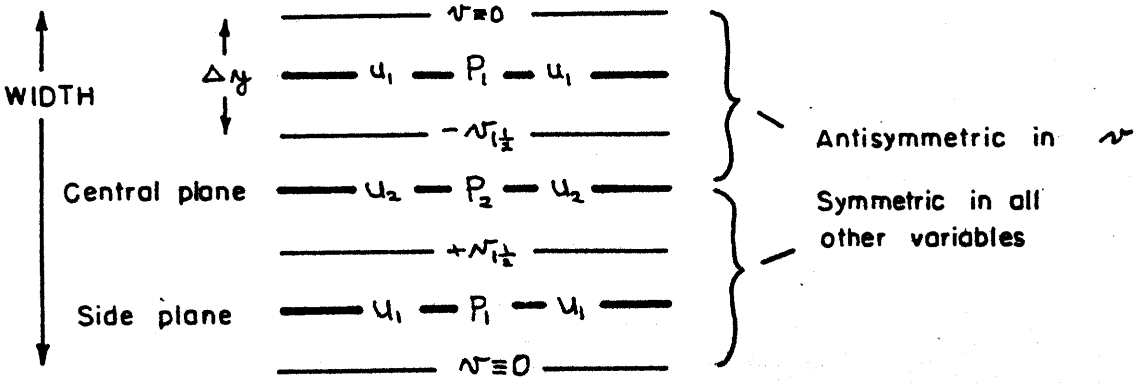

(c) A top view showing the different x-z planes.

Figure 2.2. The geometry of the grid system and domain.

parallel x-z planes as shown in Fig. 2.2 (b) for an overall view, and Fig. 2.2 (c) for a top view, in the case of three grid-points in y. The heavily outlined planes in the figures are those containing the P, u, and w grid-point values. The lightly outlined planes contain the v velocities only. The top view shows how in this case only two (P, u, w) planes (the "central" and "side") and one v plane need be computed because of the imposed symmetry. In general, we compute fields at N planes of type (P, u, w) and $N-1$ of type v. The spacing between like planes is then

$$\Delta y = \frac{\text{WIDTH}}{N+N-1} \tag{2.27}$$

The stretching used in x and z requires transformation functions relating x to i, and z to j. For the x co-ordinate the best resolution is needed near the middle of the model so a cubic transformation is used. For the 14 May simulation the particular transformation is

$$x_i = 101{\cdot}36 \times 10^3 + 400(i-58) + 0{\cdot}41218\,(i-58)^3 \tag{2.28}$$

where $x_{\frac{1}{2}} = 0$ (the left-hand edge of the domain) and $x_{100\frac{1}{2}}$ = 150 km (the right-hand edge of the domain); the number of pressure grid-points, L, is 100. Fig. 2.3 shows the resulting values of i and the grid spacing, Δx, as functions of x. The minimum spacing is 400 m at x = 101.4 km and increases almost linearly with x in each direction, the maximum being 4400 m on the left. Within the central 80-120 km - the region which is expected to contain the important convection and the leading edge of the cold air beneath the thunderstorms - the spacing is less than 1500 m and mostly less than 1000 m.

In the vertical there are M pressure grid-points, with the grid co-ordinate j ranging from 0.5 at the ground to $M+0.5$ at the top. For the model runs we use $M = 31$, since the algorithm for solving the diagnostic pressure equation requires M to be one less than a power of two. For a HEIGHT of 15 km this gives an average spacing of 484 m. The stretching is designed so that grid-points are spaced at approximately equal pressure intervals, using a hydrostatic formula based on a surface temperature and pressure of T_0 and p_0 and a constant vertical temperature gradient of $-\Gamma$. The transformation is

$$z_j = \frac{T_0}{\Gamma}\left[1 - \left(1 - (j-0.5)\frac{\Delta p}{p_0}\right)^{\frac{R_d\Gamma}{g}}\right] \qquad (2.29)$$

where the approximate pressure interval Δp is such that $z_{M+0.5}$ = HEIGHT. As an example, Fig. 2.4 shows j and Δz graphed versus z for the case of 14 May. Here, Δp is approximately 2.8 kPa. Below a height of 6000 m the spacing, Δz is everywhere less than the average spacing of 484 m. At the ground - where the best resolution is needed because of boundary effects on thunderstorm outflow - the spacing is 250 m.

Finally, if the simulated system is moving in x relative

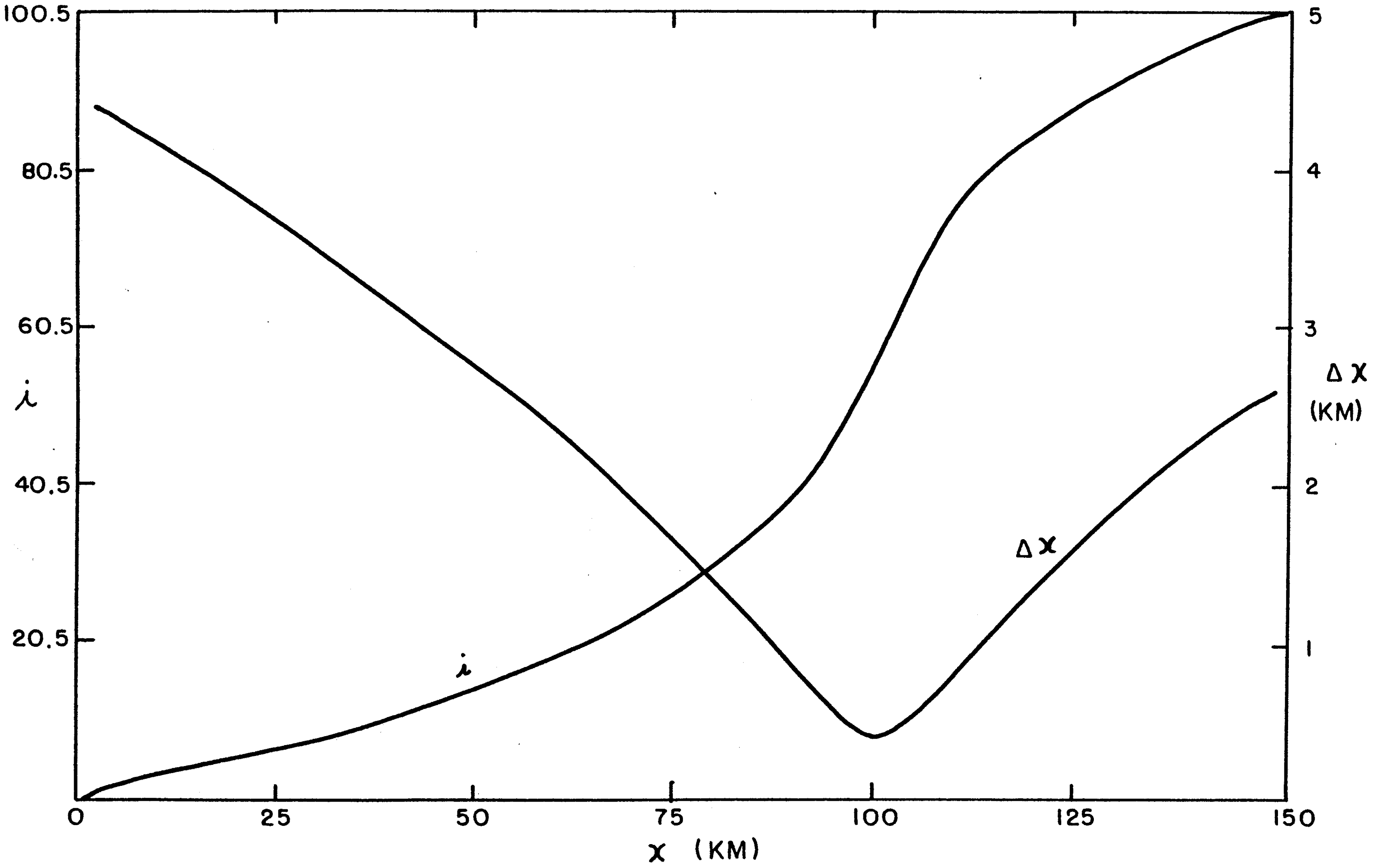

Figure 2.3. Variation of i and grid spacing Δx with x.

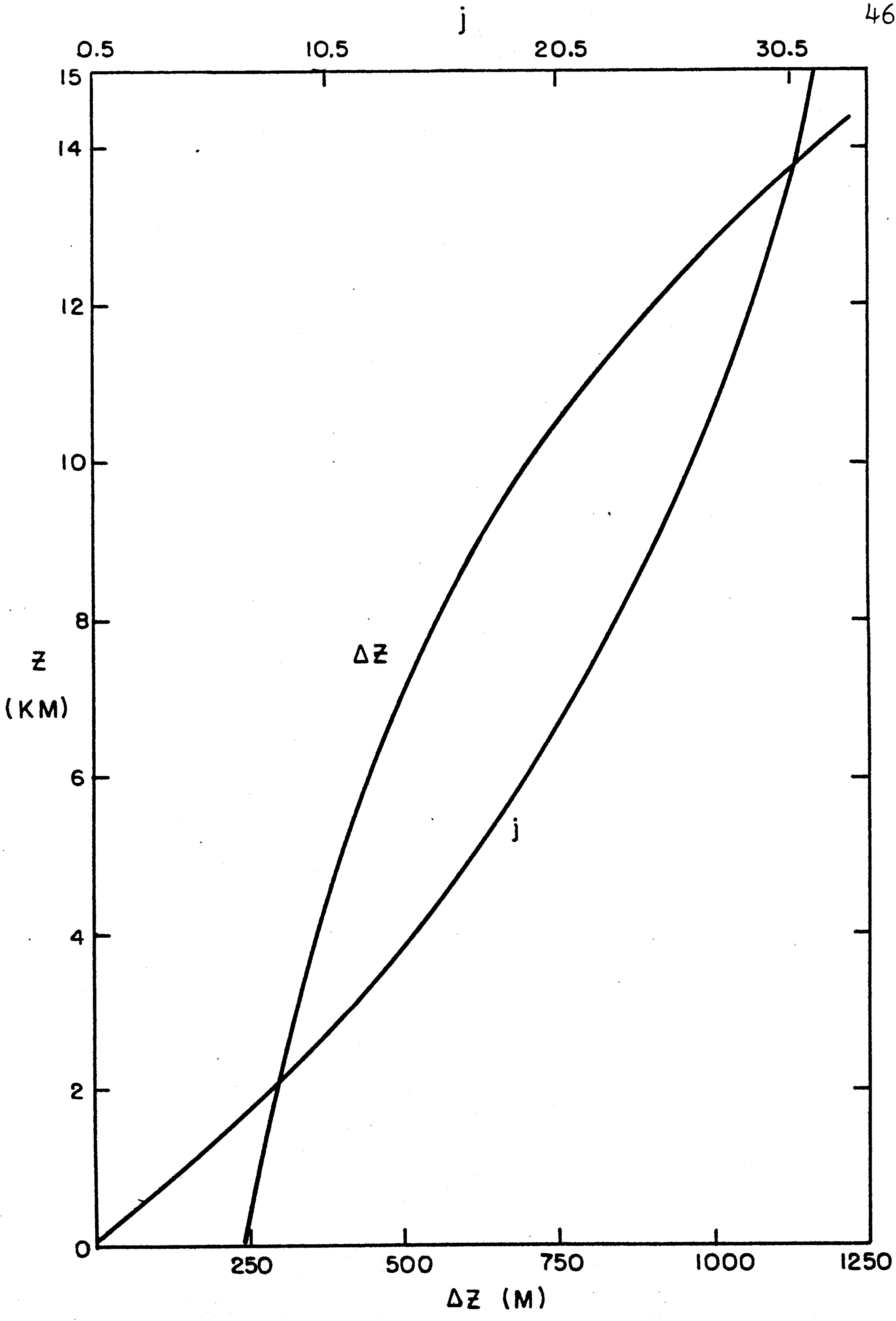

Figure 2.4. Variation of j and grid spacing Δz with z, for the simulation of 14 May 1970.

to the ground then we want to move the domain along with it to keep the fine resolution where it is needed. This is accomplished by subtracting the domain translation speed in the x direction, UTRANS, from the entire field of u velocity components, except when the stress at the ground is being computed.

2.2.2 Time Integration

Most previous cumulus- or squall-line-type models have used a combination of forward time-steps and upstream space differences, with the advantages of numerical stability and small computer storage, but the major disadvantage of strong implicit diffusion, as shown by Molenkamp (1968) among others. It is physically more appealing to compute the diffusion explicitly - even if unrealistically - than to have little control over it.

This model uses non-diffusive, centred time-differencing (leapfrog) and space-differencing, with the advective terms in the conservative (flux) form as derived by Bryan (1966) for nonuniform grids. Provided that the equation of continuity is satisfied exactly, this advective scheme is both linearly and quadratically conservative. But Piacsek and Williams (1970) have pointed out that if continuity is not satisfied exactly then the scheme is no longer quadratically conservative - for momentum advection there can be spurious increases in kinetic energy, the nonlinear instability we had hoped to avoid.[1]

---

[1] This problem would not arise for a two-dimensional model using a vorticity formulation rather than individual velocity components.

Piacsek and Williams suggested a modification to the scheme to make it exactly quadratically conservative (although there is always a time truncation error); it is also exactly linearly conservative if continuity is exact. This modification is used here for momentum only, since linear conservation is more important for the other quantities.

The leapfrog method has a well-known tendency for the solutions at alternate time-steps to separate. This separation is started off by the only first-order accuracy of the initial forward time-step; we therefore start with a small forward time-step of $\Delta t/8$ followed by straddling leapfrog steps to $\Delta t/4$, $\Delta t/2$ and finally Δt, after which the standard leapfrog can be used. The model still needs to be restarted after every thirty time-steps before the separation becomes noticeable, with fields for the last two times averaged to remove the $2\Delta t$ time component in the solution. At each restart a new time-step can be chosen - this is typically about ten seconds for linear stability.

Before proceeding with the time integration the model must first be initialized: The parameters specifying the domain size and co-ordinate stretching are input and used to set up the domain and grid. From input point values of $\overline{T}$, $\overline{Q_V}$, and $\overline{u}$ at various heights linear interpolation is used for grid-point values in the vertical - from those $\overline{p}$ is obtained hydrostatically, hence $\overline{\theta}$ and $\overline{\rho}$. Various other parameters governing the run, such as the surface drag coefficient, are input and some used to precompute coefficient vectors used often during the run. The model fields are loaded with a prescribed initial disturbance.

The following steps are carried out in sequence each time the model is integrated by the leapfrog scheme from time $t-\Delta t$ to time $t+\Delta t$ using time rates of change calculated mostly at time t:

(1) Diagnose the field of G, the computational net divergence, at time $t-\Delta t$.

(2) Diagnose the field of K_M, the eddy diffusion coefficient for momentum, for time $t-\Delta t$.

(3) Compute advection, buoyancy, and friction terms in the equations of motion.

(4) Solve the diagnostic pressure equation for the pressure at time t.

(5) Predict new velocity components for time $t+\Delta t$.

(6) Predict first-guess potential temperature and water quantities for time $t+\Delta t$ using only advection and diffusion.

(7) Optionally filter potential temperature and water vapour fields.

(8) Correct any negative values of cloud- and rain-water.

(9) Adjust cloud and rain for autoconversion and accretion.

(10) Adjust for condensation and evaporation.

Each of these steps will be explained fully in succeeding pages, with some of the required finite-difference equations. In those equations, the grid spacings are defined as

$$\Delta x_i = x_{i+\frac{1}{2}} - x_{i-\frac{1}{2}}$$

$$\Delta z_{j+\frac{1}{2}} = z_{j+1} - z_j$$

and so on, where x_i and z_j are given by the transformation functions of Section 2.2.1. Variables with a superscript $t-\Delta t$ or $t+\Delta t$ correspond to those times; all others are assumed to be defined at time t. An asterisk denotes a first-guess quantity for time $t+\Delta t$.

(1) Diagnose the field of G

We use the finite-difference version of (2.5),

$$G^{t-\Delta t}_{ijk} = \frac{u^{t-\Delta t}_{i+\frac{1}{2},j,k} - u^{t-\Delta t}_{i-\frac{1}{2},j,k}}{\Delta x_i} + \frac{v^{t-\Delta t}_{i,j,k+\frac{1}{2}} - v^{t-\Delta t}_{i,j,k-\frac{1}{2}}}{\Delta y} + \frac{\bar{\rho}_{j+\frac{1}{2}} w^{t-\Delta t}_{i,j+\frac{1}{2},k} - \bar{\rho}_{j-\frac{1}{2}} w^{t-\Delta t}_{i,j-\frac{1}{2},k}}{\bar{\rho}_j \Delta z_j} \qquad (2.30)$$

This field is used later, in Step (4).

(2) Diagnose the field of K_M

As the diffusion terms must be computed for time $t-\Delta t$ for numerical stability, the eddy diffusion coefficients are diagnosed for that time too. First we calculate a number of velocity gradient pairs to be used in both the deformation determination and the frictional forces.

$$DUU_{ijk}^{t-\Delta t} = 2\left(\frac{\partial u'}{\partial x}\right)_{ijk}^{t-\Delta t} = 2\,\frac{u'^{\,t-\Delta t}_{i+\frac{1}{2},j,k} - u'^{\,t-\Delta t}_{i-\frac{1}{2},j,k}}{\Delta x_i}$$

$$DVV_{ijk}^{t-\Delta t} = 2\left(\frac{\partial v}{\partial y}\right)_{ijk}^{t-\Delta t} = 2\,\frac{v^{t-\Delta t}_{i,j,k+\frac{1}{2}} - v^{t-\Delta t}_{i,j,k-\frac{1}{2}}}{\Delta y}$$

$$DWW_{ijk}^{t-\Delta t} = 2\left(\frac{\partial w}{\partial z}\right)_{ijk}^{t-\Delta t} = 2\,\frac{w^{t-\Delta t}_{i,j+\frac{1}{2},k} - w^{t-\Delta t}_{i,j-\frac{1}{2},k}}{\Delta z_j}$$

$$\begin{aligned} DUV_{i-\frac{1}{2},j,k+\frac{1}{2}}^{t-\Delta t} &= \left(\frac{\partial u'}{\partial y} + \frac{\partial v}{\partial x}\right)_{i-\frac{1}{2},j,k+\frac{1}{2}}^{t-\Delta t} \\ &= \frac{u'^{\,t-\Delta t}_{i-\frac{1}{2},j,k+1} - u'^{\,t-\Delta t}_{i-\frac{1}{2},j,k}}{\Delta y} + \frac{v^{t-\Delta t}_{i,j,k+\frac{1}{2}} - v^{t-\Delta t}_{i-1,j,k+\frac{1}{2}}}{\Delta x_{i-\frac{1}{2}}} \end{aligned} \tag{2.31}$$

$$\begin{aligned} DUW_{i-\frac{1}{2},j-\frac{1}{2},k}^{t-\Delta t} &= \left(\frac{\partial u'}{\partial z} + \frac{\partial w}{\partial x}\right)_{i-\frac{1}{2},j-\frac{1}{2},k}^{t-\Delta t} \\ &= \frac{u'^{\,t-\Delta t}_{i-\frac{1}{2},j,k} - u'^{\,t-\Delta t}_{i-\frac{1}{2},j-1,k}}{\Delta z_{j-\frac{1}{2}}} + \frac{w^{t-\Delta t}_{i,j-\frac{1}{2},k} - w^{t-\Delta t}_{i-1,j-\frac{1}{2},k}}{\Delta x_{i-\frac{1}{2}}} \end{aligned}$$

$$\begin{aligned} DVW_{i,j-\frac{1}{2},k+\frac{1}{2}}^{t-\Delta t} &= \left(\frac{\partial v}{\partial z} + \frac{\partial w}{\partial y}\right)_{i,j-\frac{1}{2},k+\frac{1}{2}}^{t-\Delta t} \\ &= \frac{v^{t-\Delta t}_{i,j,k+\frac{1}{2}} - v^{t-\Delta t}_{i,j-1,k+\frac{1}{2}}}{\Delta z_{j-\frac{1}{2}}} + \frac{w^{t-\Delta t}_{i,j-\frac{1}{2},k+1} - w^{t-\Delta t}_{i,j-\frac{1}{2},k}}{\Delta y} \end{aligned}$$

From these, the squared three-dimensional deformation at the grid-point $(i,\ j - \frac{1}{2},\ k)$ may be computed using mean-square averages of the velocity gradients defined at other grid-points. From (2.22),

$$\begin{aligned}\left|D^{t-\Delta t}_{i,j-\frac{1}{2},k}\right|^2 = \frac{1}{4}\Big[&\left(DUU^{t-\Delta t}_{ijk}\right)^2 + \left(DUU^{t-\Delta t}_{i,j-1,k}\right)^2\\ &+\left(DVV^{t-\Delta t}_{ijk}\right)^2 + \left(DVV^{t-\Delta t}_{i,j-1,k}\right)^2\\ &+\left(DWW^{t-\Delta t}_{ijk}\right)^2 + \left(DWW^{t-\Delta t}_{i,j-1,k}\right)^2\Big]\\ +\frac{1}{2}\Big[&\left(DUW^{t-\Delta t}_{i+\frac{1}{2},j-\frac{1}{2},k}\right)^2 + \left(DUW^{t-\Delta t}_{i-\frac{1}{2},j-\frac{1}{2},k}\right)^2\\ &+\left(DVW^{t-\Delta t}_{i,j-\frac{1}{2},k+\frac{1}{2}}\right)^2 + \left(DVW^{t-\Delta t}_{i,j-\frac{1}{2},k-\frac{1}{2}}\right)^2\Big]\\ +\frac{1}{8}\Big[&\left(DUV^{t-\Delta t}_{i-\frac{1}{2},j,k-\frac{1}{2}}\right)^2 + \left(DUV^{t-\Delta t}_{i-\frac{1}{2},j-1,k-\frac{1}{2}}\right)^2\\ &+\left(DUV^{t-\Delta t}_{i+\frac{1}{2},j,k-\frac{1}{2}}\right)^2 + \left(DUV^{t-\Delta t}_{i+\frac{1}{2},j-1,k-\frac{1}{2}}\right)^2\\ &+\left(DUV^{t-\Delta t}_{i-\frac{1}{2},j,k+\frac{1}{2}}\right)^2 + \left(DUV^{t-\Delta t}_{i-\frac{1}{2},j-1,k+\frac{1}{2}}\right)^2\\ &+\left(DUV^{t-\Delta t}_{i+\frac{1}{2},j,k+\frac{1}{2}}\right)^2 + \left(DUV^{t-\Delta t}_{i+\frac{1}{2},j-1,k+\frac{1}{2}}\right)^2\Big]\end{aligned} \qquad (2.32)$$

From this, the eddy diffusion coefficient, K_M, can be diagnosed by (2.18):

$$\begin{aligned}K^{t-\Delta t}_{M\,i,j-\frac{1}{2},k} &= k_D^2\,\Delta z_{j-\frac{1}{2}}\Delta x_i\\ &\times\left[\left|D^{t-\Delta t}_{i,j-\frac{1}{2},k}\right|^2 - d\,\frac{g}{\overline{\theta}_{j-\frac{1}{2}}\Delta z_{j-\frac{1}{2}}}\left(\theta'_{ijk}-\theta'_{i,j-1,k}-\left(\theta^{ad}_{ijk}-\theta_{i,j-1,k}\right)\right)\right]^{\frac{1}{2}}\end{aligned} \qquad (2.33)$$

θ^{ad}_{ijk} is computed by going up an adiabat from $\theta_{i,j-1,k}$ at height z_{j-1} to height z_j; a moist adiabat is used if there is cloud at both grid-points $(i, j-1, k)$ and (i, j, k). As noted in Section 2.1.3, the entire second term in the square brackets is included only when it is negative, i.e., there is moist or dry static instability.

The values of K_M at other types of grid-points are obtained by simple arithmetic averages, for example,

$$K_{M\,ijk}^{t-\Delta t} = \frac{1}{2}\left(K_{M\,i,j+\frac{1}{2},k}^{t-\Delta t} + K_{M\,i,j-\frac{1}{2},k}^{t-\Delta t}\right)$$

Values of K_H, the coefficient for heat, are easily obtained using the fixed ratio, α, between K_H and K_M.

(3) Compute advection, buoyancy and friction terms in equations of motion

(a) Advection

As noted previously, the advection of momentum is put in a flux form, with fluxes computed into and out of a box surrounding the grid-point holding the velocity component of interest. To do this we must estimate values of the advected velocity and the advection velocity on the faces of the box. As will be shown shortly, the estimated advected velocities must be simple averages of the values at the two points on either side of the face in order for there to be quadratic conservation. For instance, the estimated $u_{i-\frac{1}{2},j+\frac{1}{2},k} = \frac{1}{2}(u_{i-\frac{1}{2},j,k} + u_{i-\frac{1}{2},j+1,k})$ when u is being advected. However, the estimated advection velocities (denoted here by a tilde) must satisfy an equation of continuity for the box surrounding the predicted velocity component.

Since the original equation of motion is not satisfied exactly in practice, neither are the derived ones using the estimated advection velocities. The following formulae give the advection velocities, together with their corresponding computational net divergences $\tilde{G}$:

For predicting u:

$$
\begin{aligned}
\tilde{u}_{ijk} &= \frac{1}{2}\left(u_{i+\frac{1}{2},j,k} + u_{i-\frac{1}{2},j,k}\right) \\
\tilde{v}_{i-\frac{1}{2},j,k-\frac{1}{2}} &= \frac{\Delta x_i v_{i,j,k-\frac{1}{2}} + \Delta x_{i-1} v_{i-1,j,k-\frac{1}{2}}}{2\Delta x_{i-\frac{1}{2}}} \\
\tilde{w}_{i-\frac{1}{2},j-\frac{1}{2},k} &= \frac{\Delta x_i w_{i,j-\frac{1}{2},k} + \Delta x_{i-1} w_{i-1,j-\frac{1}{2},k}}{2\Delta x_{i-\frac{1}{2}}} \\
\tilde{G}_{i-\frac{1}{2},j,k} &= \frac{\Delta x_i G_{ijk} + \Delta x_{i-1} G_{i-1,j,k}}{2\Delta x_{i-\frac{1}{2}}}
\end{aligned}
\qquad (2.34)
$$

For predicting v:

$$
\begin{aligned}
\tilde{u}_{i-\frac{1}{2},j,k-\frac{1}{2}} &= \frac{1}{2}\left(u_{i-\frac{1}{2},j,k} + u_{i-\frac{1}{2},j,k-1}\right) \\
\tilde{v}_{ijk} &= \frac{1}{2}\left(v_{i,j,k+\frac{1}{2}} + v_{i,j,k-\frac{1}{2}}\right) \\
\tilde{w}_{i,j-\frac{1}{2},k-\frac{1}{2}} &= \frac{1}{2}\left(w_{i,j-\frac{1}{2},k} + w_{i,j-\frac{1}{2},k-1}\right) \\
\tilde{G}_{i,j,k-\frac{1}{2}} &= \frac{1}{2}\left(G_{ijk} + G_{i,j,k-1}\right)
\end{aligned}
\qquad (2.35)
$$

For predicting W:

$$\begin{aligned}
\tilde{u}_{i-\frac{1}{2},j-\frac{1}{2},k} &= \frac{\bar{\rho}_j \Delta z_j u_{i-\frac{1}{2},j,k} \quad + \bar{\rho}_{j-1} \Delta z_{j-1} u_{i-\frac{1}{2},j-1,k}}{2\bar{\rho}_{j-\frac{1}{2}} \Delta z_{j-\frac{1}{2}}} \\
\tilde{v}_{i,j-\frac{1}{2},k-\frac{1}{2}} &= \frac{\bar{\rho}_j \Delta z_j v_{i,j,k-\frac{1}{2}} \quad + \bar{\rho}_{j-1} \Delta z_{j-1} v_{i,j-1,k-\frac{1}{2}}}{2\bar{\rho}_{j-\frac{1}{2}} \Delta z_{j-\frac{1}{2}}} \\
\tilde{W}_{ijk} &= \frac{\bar{\rho}_{j+\frac{1}{2}} W_{i,j+\frac{1}{2},k} + \bar{\rho}_{j-\frac{1}{2}} W_{i,j-\frac{1}{2},k}}{2\bar{\rho}_j} \\
\tilde{G}_{i,j-\frac{1}{2},k} &= \frac{\bar{\rho}_j \Delta z_j G_{ijk} \quad + \bar{\rho}_{j-1} \Delta z_{j-1} G_{i,j-1,k}}{2\bar{\rho}_{j-\frac{1}{2}} \Delta z_{j-\frac{1}{2}}}
\end{aligned} \tag{2.36}$$

Using these, we could now write the advection terms for the prediction of $u_{i-\frac{1}{2},j,k}$, as an example, as:

$$\frac{1}{\bar{\rho}} \nabla \cdot (\bar{\rho} u \underset{\sim}{V}) \Big|_{i-\frac{1}{2},j,k} =$$

$$\frac{\frac{1}{2}\left(u_{i+\frac{1}{2},j,k} + u_{i-\frac{1}{2},j,k}\right)\tilde{u}_{ijk} \quad - \frac{1}{2}\left(u_{i-\frac{1}{2},j,k} + u_{i-\frac{3}{2},j,k}\right)\tilde{u}_{i-1,j,k}}{\Delta x_{i-\frac{1}{2}}}$$

$$+ \frac{\frac{1}{2}\left(u_{i-\frac{1}{2},j,k+1} + u_{i-\frac{1}{2},j,k}\right)\tilde{v}_{i-\frac{1}{2},j,k+\frac{1}{2}} - \frac{1}{2}\left(u_{i-\frac{1}{2},j,k} + u_{i-\frac{1}{2},j,k-1}\right)\tilde{v}_{i-\frac{1}{2},j,k-\frac{1}{2}}}{\Delta y}$$

$$+ \frac{\frac{1}{2}\bar{\rho}_{j+\frac{1}{2}}\left(u_{i-\frac{1}{2},j+1,k} + u_{i-\frac{1}{2},j,k}\right)\tilde{W}_{i-\frac{1}{2},j+\frac{1}{2},k} - \frac{1}{2}\bar{\rho}_{j-\frac{1}{2}}\left(u_{i-\frac{1}{2},j,k} + u_{i-\frac{1}{2},j-1,k}\right)\tilde{W}_{i-\frac{1}{2},j-\frac{1}{2},k}}{\bar{\rho}_j \Delta z_j}$$

This is in exactly linearly conservative form, which can be verified by multiplying through by $\bar{\rho}_j \Delta x_{i-\frac{1}{2}} \Delta y \Delta z_j$ and noting that each term denoting a flux out of one box into a second box is the same whether we are predicting the velocity in the first or in the second.

But the advection is not in exactly quadratically conservative form. We can show this by subtracting $\frac{1}{2}u_{i-\frac{1}{2},j,k}$ times the equation of continuity satisfied by the advecting velocities, that is

$$\frac{1}{2}u_{i-\frac{1}{2},j,k}\times\left[\frac{\tilde{u}_{ijk}-\tilde{u}_{i-1,j,k}}{\Delta x_{i-\frac{1}{2}}}+\frac{\tilde{v}_{i-\frac{1}{2},j,k+\frac{1}{2}}-\tilde{v}_{i-\frac{1}{2},j,k-\frac{1}{2}}}{\Delta y}\right.$$
$$\left.+\frac{\bar{\rho}_{j+\frac{1}{2}}\tilde{W}_{i-\frac{1}{2},j+\frac{1}{2},k}-\bar{\rho}_{j-\frac{1}{2}}\tilde{W}_{i-\frac{1}{2},j-\frac{1}{2},k}}{\bar{\rho}_j\Delta z_j}-\tilde{G}_{i-\frac{1}{2},j,k}\right]$$

to get

$$\frac{1}{\bar{\rho}}\nabla\cdot(\bar{\rho}u\underset{\sim}{V})\Big|_{i-\frac{1}{2},j,k}=$$
$$\frac{u_{i+\frac{1}{2},j,k}\tilde{u}_{ijk}-u_{i-\frac{3}{2},j,k}\tilde{u}_{i-1,j,k}}{2\Delta x_{i-\frac{1}{2}}}$$
$$+\frac{u_{i-\frac{1}{2},j,k+1}\tilde{v}_{i-\frac{1}{2},j,k+\frac{1}{2}}-u_{i-\frac{1}{2},j,k-1}\tilde{v}_{i-\frac{1}{2},j,k-\frac{1}{2}}}{2\Delta y} \qquad (2.37)$$
$$+\frac{\bar{\rho}_{j+\frac{1}{2}}u_{i-\frac{1}{2},j+1,k}\tilde{W}_{i-\frac{1}{2},j+\frac{1}{2},k}-\bar{\rho}_{j-\frac{1}{2}}u_{i-\frac{1}{2},j-1,k}\tilde{W}_{i-\frac{1}{2},j-\frac{1}{2},k}}{2\bar{\rho}_j\Delta z_j}$$
$$+\frac{1}{2}u_{i-\frac{1}{2},j,k}\tilde{G}_{i-\frac{1}{2},j,k}$$

(Note that we could not have done this if the estimated advected velocities had not been simple averages.)

If we now try multiplying through by $\bar{\rho}_j\Delta x_{i-\frac{1}{2}}\Delta y\Delta z_j u_{i-\frac{1}{2},j,k}$ we find that the fluxes of $\bar{\rho}u^2$ across the faces between adjacent grid boxes match again, except for the term in $\tilde{G}_{i-\frac{1}{2},j,k}$. Only if that is zero can we have exact quadratic conservation. So in the application of (2.37) we neglect that term entirely, retaining consistency with the original mathematical equations since the field of $\tilde{G}_{i-\frac{1}{2},j,k}$ should be zero anyway. Now the advection is exactly quadratically conservative - a desirable feature for kinetic energy conservation - but no longer exactly linearly conservative because of the non-zero $\tilde{G}_{i-\frac{1}{2},j,k}$.

The advection terms for $v_{i,j,k-\frac{1}{2}}$ and $w_{i,j-\frac{1}{2},k}$ are obtained similarly, resulting in

$$\frac{1}{\bar{\rho}}\nabla\cdot(\bar{\rho}v\underset{\sim}{V})\Big|_{i,j,k-\frac{1}{2}} = \frac{v_{i+1,j,k-\frac{1}{2}}\tilde{U}_{i+\frac{1}{2},j,k-\frac{1}{2}} - v_{i-1,j,k-\frac{1}{2}}\tilde{U}_{i-\frac{1}{2},j,k-\frac{1}{2}}}{2\Delta x_i} + \frac{v_{i,j,k+\frac{1}{2}}\tilde{V}_{i,j,k} - v_{i,j,k-3/2}\tilde{V}_{i,j,k-1}}{2\Delta y} + \frac{\bar{\rho}_{j+\frac{1}{2}}v_{i,j+1,k-\frac{1}{2}}\tilde{W}_{i,j+\frac{1}{2},k-\frac{1}{2}} - \bar{\rho}_{j-\frac{1}{2}}v_{i,j-1,k-\frac{1}{2}}\tilde{W}_{i,j-\frac{1}{2},k-\frac{1}{2}}}{2\bar{\rho}_j\Delta z_j} \tag{2.38}$$

$$\frac{1}{\bar{\rho}}\nabla\cdot(\bar{\rho}w\underset{\sim}{V})\Big|_{i,j-\frac{1}{2},k} = \frac{w_{i+1,j-\frac{1}{2},k}\tilde{U}_{i+\frac{1}{2},j-\frac{1}{2},k} - w_{i-1,j-\frac{1}{2},k}\tilde{U}_{i-\frac{1}{2},j-\frac{1}{2},k}}{2\Delta x_i} + \frac{w_{i,j-\frac{1}{2},k+1}\tilde{V}_{i,j-\frac{1}{2},k+\frac{1}{2}} - w_{i,j-\frac{1}{2},k-1}\tilde{V}_{i,j-\frac{1}{2},k-\frac{1}{2}}}{2\Delta y} + \frac{\bar{\rho}_j w_{i,j+\frac{1}{2},k}\tilde{W}_{i,j,k} - \bar{\rho}_{j-1}w_{i,j-3/2,k}\tilde{W}_{i,j-1,k}}{2\bar{\rho}_{j-\frac{1}{2}}\Delta z_{j-\frac{1}{2}}} \tag{2.39}$$

(b) Buoyancy

The buoyancy terms in the vertical equation of motion (2.4) must use simple averages since the potential temperature and water quantities are not defined at the same points as the vertical velocity.

$$
\begin{aligned}
&g\bar{\rho}\left(\frac{\theta'}{\bar{\theta}} + aQ_v' - (Q_c+Q_R)\right)\Big|_{i,j-\frac{1}{2},k} = \\
&\frac{1}{2}\Bigg[\frac{\theta'_{i,j,k}+\theta'_{i,j-1,k}}{\bar{\theta}_{j-\frac{1}{2}}} + a\left(Qv_{i,j,k}+Qv_{i,j-1,k}-2\bar{Q}v_{j-\frac{1}{2}}\right) \\
&\qquad -\left(Qc_{i,j,k}+Qc_{i,j-1,k}+QR_{i,j,k}+QR_{i,j-1,k}\right)\Bigg]\times g\bar{\rho}_{j-\frac{1}{2}}
\end{aligned}
\tag{2.40}
$$

(c) Friction

The friction terms in the equations of motion use the velocity gradient pairs previously computed for the diagnosis of K_M, and defined at time $t-\Delta t$.

$$
\begin{aligned}
\frac{Fx^{t-\Delta t}_{i-\frac{1}{2},j,k}}{\bar{\rho}_j} = {}& \frac{K_{M\,i,j,k}^{t-\Delta t}\,DUU^{t-\Delta t}_{i,j,k} - K_{M\,i-1,j,k}^{t-\Delta t}\,DUU^{t-\Delta t}_{i-1,j,k}}{\Delta x_{i-\frac{1}{2}}} \\
&+ \frac{K_{M\,i-\frac{1}{2},j,k+\frac{1}{2}}^{t-\Delta t}\,DUV^{t-\Delta t}_{i-\frac{1}{2},j,k+\frac{1}{2}} - K_{M\,i-\frac{1}{2},j,k-\frac{1}{2}}^{t-\Delta t}\,DUV^{t-\Delta t}_{i-\frac{1}{2},j,k-\frac{1}{2}}}{\Delta y} \\
&+ \frac{K_{M\,i-\frac{1}{2},j+\frac{1}{2},k}^{t-\Delta t}\,DUW^{t-\Delta t}_{i-\frac{1}{2},j+\frac{1}{2},k} - K_{M\,i-\frac{1}{2},j-\frac{1}{2},k}^{t-\Delta t}\,DUW^{t-\Delta t}_{i-\frac{1}{2},j-\frac{1}{2},k}}{\Delta z_j}
\end{aligned}
\tag{2.41}
$$

$$
\begin{aligned}
\frac{Fy^{t-\Delta t}_{i,j,k-\frac{1}{2}}}{\bar{\rho}_j} = {}& \frac{K_{M\,i+\frac{1}{2},j,k-\frac{1}{2}}^{t-\Delta t}\,DUV^{t-\Delta t}_{i+\frac{1}{2},j,k-\frac{1}{2}} - K_{M\,i-\frac{1}{2},j,k-\frac{1}{2}}^{t-\Delta t}\,DUV^{t-\Delta t}_{i-\frac{1}{2},j,k-\frac{1}{2}}}{\Delta x_i} \\
&+ \frac{K_{M\,i,j,k}^{t-\Delta t}\,DVV^{t-\Delta t}_{i,j,k} - K_{M\,i,j,k-1}^{t-\Delta t}\,DVV^{t-\Delta t}_{i,j,k-1}}{\Delta y} \\
&+ \frac{K_{M\,i,j+\frac{1}{2},k-\frac{1}{2}}^{t-\Delta t}\,DVW^{t-\Delta t}_{i,j+\frac{1}{2},k-\frac{1}{2}} - K_{M\,i,j-\frac{1}{2},k-\frac{1}{2}}^{t-\Delta t}\,DVW^{t-\Delta t}_{i,j-\frac{1}{2},k-\frac{1}{2}}}{\Delta z_j}
\end{aligned}
\tag{2.42}
$$

$$\frac{F_{z\,i,j-\frac{1}{2},k}^{t-\Delta t}}{\bar{\rho}_{j-\frac{1}{2}}} = \frac{K_{M\,i+\frac{1}{2},j-\frac{1}{2},k}^{t-\Delta t}\, DUW_{i+\frac{1}{2},j-\frac{1}{2},k}^{t-\Delta t} - K_{M\,i-\frac{1}{2},j-\frac{1}{2},k}^{t-\Delta t}\, DUW_{i-\frac{1}{2},j-\frac{1}{2},k}^{t-\Delta t}}{\Delta x_i}$$

$$+ \frac{K_{M\,i,j-\frac{1}{2},k+\frac{1}{2}}^{t-\Delta t}\, DVW_{i,j-\frac{1}{2},k+\frac{1}{2}}^{t-\Delta t} - K_{M\,i-\frac{1}{2},j-\frac{1}{2},k-\frac{1}{2}}^{t-\Delta t}\, DVW_{i,j-\frac{1}{2},k-\frac{1}{2}}^{t-\Delta t}}{\Delta y} \quad (2.43)$$

$$+ \frac{K_{M\,i,j,k}^{t-\Delta t}\;\; DWW_{i,j,k}^{t-\Delta t} \;\; - K_{M\,i,j-1,k}^{t-\Delta t}\, DWW_{i,j-1,k}^{t-\Delta t}}{\Delta z_{j-\frac{1}{2}}}$$

Of course, boundary conditions are used to determine some of the values of the velocity gradients. For instance, when applying (2.41) at the top level for computing the u velocities ($j = M$) we have $DUW_{i-\frac{1}{2},M+\frac{1}{2},k} \equiv (\partial u/\partial z + \partial w/\partial x)_{i-\frac{1}{2},M+\frac{1}{2},k} \equiv 0$ since the top boundary conditions are that $\partial u/\partial z = 0$ and $w = 0$.

At the lower boundary, the stresses $\bar{\rho}\, K_{M_{i-\frac{1}{2},\frac{1}{2},k}}\, DUW_{i-\frac{1}{2},\frac{1}{2},k}$ and $\bar{\rho}\, K_{M\,i,\frac{1}{2},k}\, DVW_{i,\frac{1}{2},k}$ are computed by equating them with a drag force at an imaginary anemometer level of 10 m. If the anemometer wind has components u_a and v_a, the velocity components relative to the ground at $j = 1$ are u_1 and v_1, and the diagnosed eddy diffusion coefficient of momentum is K_M, then

$$\tau_x = \bar{\rho}\, C_D\, u_a \sqrt{u_a^2 + v_a^2}$$

in terms of a drag coefficient C_D, and

$$\tau_x = \bar{\rho}\, K_M\, \frac{u_1 - u_a}{z_1 - 10}$$

in terms of the velocity gradient. Similar equations can be written for the stress τ_y. By equating the stresses we can solve for the anemometer-level wind components:

$$u_a = \frac{1}{\alpha}\left(-1+\sqrt{1+2\alpha u_1}\right)$$

$$v_a = \left(\frac{v_1}{u_1}\right)u_a \tag{2.44}$$

$$\text{where } \alpha = 2\,\frac{C_D(z_1-10)}{K_M}\sqrt{1+\left(\frac{v_1}{u_1}\right)^2} \times \text{sign}(u_1)$$

and hence obtain the stress at the ground.

For example, if the velocity components at $z_1 = 250$ m are $u_1 = 15.0$ m s^{-1} and $v_1 = 5.0$ m s^{-1}, the drag coefficient C_D is 0.002, and the eddy diffusion coefficient is 100 m^2 s^{-1}, then u_a will be 14.0 m s^{-1} and v_a will be one-third of that (there is no wind direction change). For a lower eddy diffusion coefficient of 10 m^2 s^{-1} u_a will decrease to 10.0 m s^{-1}.

Note that if the domain is being translated at a speed UTRANS in the x direction relative to the ground, then the u velocity component relative to the domain must have UTRANS added to it to obtain u_1 relative to the ground in order to compute the correct stress.

(4) Solve the diagnostic pressure equation

To obtain the finite-difference version of the diagnostic pressure equation, we combine the continuous time derivative of the finite-difference continuity equation (2.30) with the three finite-difference versions of the equations of motion:

$$\frac{\partial u_{i-\frac{1}{2},j,k}}{\partial t} = A_{i-\frac{1}{2},j,k} - R_d\,\bar{\theta}_j\,\frac{P_{ijk}-P_{i-1,j,k}}{\Delta x_{i-\frac{1}{2}}} \tag{2.45}$$

$$\frac{\partial v_{i,j,k-\frac{1}{2}}}{\partial t} = B_{i,j,k-\frac{1}{2}} - R_d \overline{\Theta}_j \; \frac{P_{i,j,k} - P_{i,j,k-1}}{\Delta y} \tag{2.46}$$

$$\frac{\partial W_{i,j-\frac{1}{2},k}}{\partial t} = C_{i,j-\frac{1}{2},k} - R_d \overline{\Theta}_{j-\frac{1}{2}} \frac{P_{ijk} - P_{i,j-1,k}}{\Delta z_{j-\frac{1}{2}}} \tag{2.47}$$

to get

$$\begin{aligned} & al_i \, P_{i-1,j,k} + cl_i \, P_{i+1,j,k} + am_j \, P_{i,j-1,k} + cm_j \, P_{i,j+1,k} \\ & + \frac{1}{(\Delta y)^2}\left(P_{i,j,k+1} + P_{i,j,k-1}\right) \\ & - \left[al_i + cl_i + am_j + cm_j + \frac{2}{(\Delta y)^2}\right] P_{ijk} \quad = F_{ijk} \end{aligned} \tag{2.48}$$

where

$$al_i = \frac{1}{\Delta x_i \, \Delta x_{i-\frac{1}{2}}} \qquad cl_i = \frac{1}{\Delta x_i \, \Delta x_{i+\frac{1}{2}}}$$

$$am_j = \frac{\overline{\rho}_{j-\frac{1}{2}} \, \overline{\Theta}_{j-\frac{1}{2}}}{\overline{\rho}_j \; \overline{\Theta}_j} \times \frac{1}{\Delta z_j \, \Delta z_{j-\frac{1}{2}}} \qquad cm_j = \frac{\overline{\rho}_{j+\frac{1}{2}} \overline{\Theta}_{j+\frac{1}{2}}}{\overline{\rho}_j \; \overline{\Theta}_j} \times \frac{1}{\Delta z_j \, \Delta z_{j+\frac{1}{2}}}$$

and the forcing function F_{ijk} is

$$\begin{aligned} F_{ijk} = & \frac{1}{R_d \, \overline{\Theta}_j} \left(\frac{A_{i+\frac{1}{2},j,k} - A_{i-\frac{1}{2},j,k}}{\Delta x_i} \right) \\ & + \frac{1}{R_d \overline{\Theta}_j} \left(\frac{B_{i,j,k+\frac{1}{2}} - B_{i,j,k-\frac{1}{2}}}{\Delta y} \right) \\ & + \frac{1}{R_d \overline{\Theta}_j} \left(\frac{\overline{\rho}_{j+\frac{1}{2}} C_{i,j+\frac{1}{2},k} - \overline{\rho}_{j-\frac{1}{2}} C_{i,j-\frac{1}{2},k}}{\overline{\rho}_j \, \Delta z_j} \right) \\ & - \frac{1}{R_d \overline{\Theta}_j} \; \frac{\partial G_{ijk}}{\partial t} \end{aligned} \tag{2.49}$$

and we take

$$\frac{\partial G_{ijk}}{\partial t} = \frac{0 - G_{ijk}^{t-\Delta t}}{2\Delta t}$$

so that the solution for the pressure will tend to bring $G_{ijk}^{t+\Delta t}$ close to zero.

To solve (2.48) we first Fourier transform it in the y direction. Due to the imposed periodicity and symmetry the pressure and forcing functions must have the form

$$P_{ijk} = \sum_{kc=1}^{N} \mathbb{P}_{ij}^{kc} \cos\left[(kc-1)\omega(N-k)\right]$$

$$F_{ijk} = \sum_{kc=1}^{N} \mathbb{F}_{ij}^{kc} \cos\left[(kc-1)\omega(N-k)\right]$$

where $\mathbb{P}_{ij}^{kc}$ and $\mathbb{F}_{ij}^{kc}$ are the magnitudes of the kc-th components, and

$$\omega = \frac{2\pi}{N-1}$$

Substitution into (2.48) leads to a separate elliptic equation for each component,

$$\begin{aligned} al_i \mathbb{P}_{i-1,j}^{kc} + cl_i \mathbb{P}_{i+1,j}^{kc} + am_j \mathbb{P}_{i,j-1}^{kc} + cm_j \mathbb{P}_{i,j+1}^{kc} \\ - \left[\frac{2(1-\cos(\omega(kc-1)))}{(\Delta y)^2} + al_i + cl_i + am_j + cm_j\right] \mathbb{P}_{ij}^{kc} \\ = \mathbb{F}_{ij}^{kc} \end{aligned} \qquad (2.50)$$

We can now solve for the pressure by the following steps:

(a) Transform from $F_{ijk} \rightarrow \mathbb{F}_{ij}^{kc}$, for $kc = 1, 2, \ldots N$. Since there are so few components this is done using linear combinations rather than a fast Fourier transform.

(b) Call a package set of programs (Swartztrauber and Sweet, 1975) which solves for each field $\mathbb{P}_{ij}^{kc}$ using a direct solution method.

(c) Transform back from $\mathbb{P}_{ij}^{kc} \rightarrow P_{ijk}$, again using linear combinations.

In solving the equations, the boundary condition in z is that the pressure field must maintain zero vertical velocity at the top and bottom, i.e., $\partial w/\partial t = 0$. From the vertical equation of motion (2.47) we see that this will be satisfied by setting $C_{i,\frac{1}{2},k} = C_{i,M+\frac{1}{2},k} = 0$ and using as the boundary condition $\partial P/\partial z = 0$ (by setting $am_1 = cm_M = 0$). If we wish, we can later calculate the actual values of C at top and bottom (given by boundary conditions) and hence find the actual pressure gradient there, such that $\partial w/\partial t = 0$ is still satisfied.

The boundary conditions in x are that for $x = 0$ and x = LENGTH the pressure is exactly hydrostatic at all points, with $P = 0$ at the top right, and P set at the top left so that the net pressure gradient causes zero integrated momentum change over the domain. In practice this means that for $i = 2$ in (2.48) the term $al_i P_{i-1,j,k}$ is now known, so can be transferred to the right-hand side of the equation to become part of the forcing function. Similarly, for $i = L - 1$ the term $cl_i P_{i+1,j,k}$ is known and can be transferred across.

There are no boundary conditions to consider in y - they are implicitly handled by the cosine form of the solution.

(5) Predict new velocity components

Now that we have the pressure field diagnosed, it is a simple matter to predict the new velocity components at time $t + \Delta t$:

$$u^{t+\Delta t}_{i-\frac{1}{2},j,k} = u^{t-\Delta t}_{i-\frac{1}{2},j,k} + 2\Delta t \left(A_{i-\frac{1}{2},j,k} - R_d \bar{\theta}_j \frac{P_{ijk} - P_{i-1,j,k}}{\Delta x_{i-\frac{1}{2}}} \right)$$

$$v^{t+\Delta t}_{i,j,k-\frac{1}{2}} = v^{t-\Delta t}_{i,j,k-\frac{1}{2}} + 2\Delta t \left(B_{i,j,k-\frac{1}{2}} - R_d \bar{\theta}_j \frac{P_{ijk} - P_{i,j,k-1}}{\Delta y} \right)$$

$$w^{t+\Delta t}_{i,j-\frac{1}{2},k} = w^{t-\Delta t}_{i,j-\frac{1}{2},k} + 2\Delta t \left(C_{i,j-\frac{1}{2},k} - R_d \bar{\theta}_{j-\frac{1}{2}} \frac{P_{ijk} - P_{i,j-1,k}}{\Delta z_{j-\frac{1}{2}}} \right)$$

(6) Predict first-guess potential temperature and water quantities

The first-guess predictions are made using only advection and diffusion. The equation for θ' is

$$
\begin{aligned}
\theta'^{*}_{ijk} = \theta'^{\,t-\Delta t}_{ijk} + 2\Delta t \Big[& - \frac{\frac{1}{2}(\theta'_{i+1,j,k} + \theta'_{ijk})u_{i+\frac{1}{2},j,k} - \frac{1}{2}(\theta'_{ijk} + \theta'_{i-1,j,k})u_{i-\frac{1}{2},j,k}}{\Delta x_i} \\
& - \frac{\frac{1}{2}(\theta'_{i,j,k+1} + \theta'_{ijk})v_{i,j,k+\frac{1}{2}} - \frac{1}{2}(\theta'_{ijk} + \theta'_{i,j,k-1})v_{i,j,k-\frac{1}{2}}}{\Delta y} \\
& - \frac{\frac{1}{2}\bar{\rho}_{j+\frac{1}{2}}(\theta'_{i,j+1,k} + \theta'_{ijk})W_{i,j+\frac{1}{2},k} - \frac{1}{2}\bar{\rho}_{j-\frac{1}{2}}(\theta'_{ijk} + \theta'_{i,j-1,k})W_{i,j-\frac{1}{2},k}}{\bar{\rho}_j \Delta z_j} \\
& - \frac{1}{2}\left(W_{i,j+\frac{1}{2},k} + W_{i,j-\frac{1}{2},k}\right) \times \frac{\bar{\theta}_{j+\frac{1}{2}} - \bar{\theta}_{j-\frac{1}{2}}}{\Delta z_j} \\
& + \frac{1}{\Delta x_i}\left(K^{\,t-\Delta t}_{H\,i+\frac{1}{2},j,k} \frac{\theta'^{\,t-\Delta t}_{i+1,j,k} - \theta'^{\,t-\Delta t}_{ijk}}{\Delta x_{i+\frac{1}{2}}} - K^{\,t-\Delta t}_{H\,i-\frac{1}{2},j,k} \frac{\theta'^{\,t-\Delta t}_{ijk} - \theta'^{\,t-\Delta t}_{i-1,j,k}}{\Delta x_{i-\frac{1}{2}}} \right) \\
& + \frac{1}{\Delta y}\left(K^{\,t-\Delta t}_{H\,i,j,k+\frac{1}{2}} \frac{\theta'^{\,t-\Delta t}_{i,j,k+1} - \theta'^{\,t-\Delta t}_{ijk}}{\Delta y} - K^{\,t-\Delta t}_{H\,i,j,k-\frac{1}{2}} \frac{\theta'^{\,t-\Delta t}_{ijk} - \theta'^{\,t-\Delta t}_{i,j,k-1}}{\Delta y} \right) \\
& + \frac{1}{\bar{\rho}_j \Delta z_j}\left(\bar{\rho}_{j+\frac{1}{2}} K^{\,t-\Delta t}_{H\,i,j+\frac{1}{2},k} \frac{\theta'^{\,t-\Delta t}_{i,j+1,k} - \theta'^{\,t-\Delta t}_{ijk}}{\Delta z_{j+\frac{1}{2}}} - \bar{\rho}_{j-\frac{1}{2}} K^{\,t-\Delta t}_{H\,i,j-\frac{1}{2},k} \frac{\theta'^{\,t-\Delta t}_{ijk} - \theta'^{\,t-\Delta t}_{i,j-1,k}}{\Delta z_{j-\frac{1}{2}}} \right) \Big]
\end{aligned}
\tag{2.51}
$$

The prediction equations for the water quantities (Q_V, Q_C, and Q_R) are analagous to those for θ', except:

(a) There is no term corresponding to $W\partial\bar{\theta}/\partial z$.

(b) For rain-water there is no diffusion, but a terminal velocity diagnosed for time $t-\Delta t$ is included.

(c) The diffusion of water vapour in the vertical is in terms of Q_V' rather than Q_V; we do not smooth the base-state profile of water vapour.

Note that the advection terms in these equations are in linearly conservative form. Since simple averages are used for the advected quantities the advection is also almost quadratically conservative, but not quite, since the equation of continuity doesn't hold exactly (see part (a) of Step (3)).

(7) Optionally filter the temperature and water vapour fields

In initial experiments with the model, small-scale noise with a predominantly $2\Delta x$ component developed in the temperature and moisture fields after about an hour of simulated time. This was a consequence of aliasing error on the smallest scales; the noise remained bounded because of the quadratically conservative scheme.

Rather than control the noise with stronger diffusion we apply a sixteenth order Shapiro filter (Shapiro, 1970) in the direction to the fields of θ'^* and Q_v^*. This can be considered as a continuation of the diffusion calculations, although, unlike the parameterized diffusion, the filter applied is very selective in its frequency response. One application removes completely the $2\Delta x$ component, 10% of the $3\Delta x$ component, and less than 0.4% of components of period $4\Delta x$ and longer. Even after 100 applications, only 2% of the $5\Delta x$ component has been filtered out.

Comparison runs conducted with a preliminary, small version of the model both with and without the filter indicated little difference in the results after an hour's simulated time, _except_ that the very-small-scale noise had been well controlled.

The computational details of the filter application are discussed in Appendix C.

(8) Correct any negative values of cloud- or rain-water

An unfortunate characteristic of the numerical advection scheme is that, unlike the forward-upstream scheme, it can produce negative amounts of cloud- or rain-water. This is usually produced by a net flux of water out of a grid box which had none to start with.

To correct for this, we could just bring the negative values back up to zero, but that would spuriously increase the total amount of water in the model. Clark (1973) suggested a "hole-filling" approach of bringing water back from surrounding grid boxes into which there had been a flux, in proportion to that flux, to just reach zero water. We use the similar, but computationally easier, technique of bringing back water in proportion to the amount in the surrounding grid boxes rather than the flux into them.

Occasionally there is no water in any of the surrounding grid boxes - it has presumably been advected farther afield. In this case we simply increase the value to zero; the total amount of extra water added is tiny.

(9) Adjust cloud and rain for autoconversion and accretion

The autoconversion and accretion rates are diagnosed for time $t-\Delta t$ using equations (2.13) and (2.9). If they are instead diagnosed for time t, then a numerical instability can develop which is similar to that when centred time differences are used on a diffusion equation. The reason for this is that accretion and autoconversion each act as negative feedbacks on the local amount of cloud-water; increase Q_c and each rate will also increase, tending to bring Q_c back towards its original value. But if the negative feedback applied depends on the value of Q_c at the central time then the solutions at alternate time-steps will diverge.

To illustrate this, consider a process with an exactly linear feedback:

$$\frac{dQ}{dt} = -a\left(Q - Q_\infty\right)$$

where a is a positive constant, and Q_∞ is any value. The mathematical solution for this equation with any starting value Q_0 is

$$Q(t) = Q_\infty + \left(Q_0 - Q_\infty\right)e^{-at}$$

so Q tends exponentially towards the limit value, Q_∞. But if we try using the leapfrog scheme on the equation we have for two consecutive times:

$$Q^{t+\Delta t} = Q^{t-\Delta t} + 2\Delta t\left(-aQ^{t} + aQ_\infty\right)$$
$$Q^{t+2\Delta t} = Q^{t} \quad + 2\Delta t\left(-aQ^{t+\Delta t} + aQ_\infty\right)$$

Taking the difference between these two equations:

$$Q^{t+2\Delta t} - Q^{t+\Delta t} = \left(1 + 2a\Delta t\right)\left(Q^{t} - Q^{t-\Delta t}\right)$$

So any initial separation between the values at consecutive times will increase exponentially, by a factor of $1+2a\Delta t$ every two time-steps. This is a highly unstable scheme!

Similar problems could arise with the diagnosis of the rain terminal velocity (acts as a negative feedback on the local mixing ratio of rain-water, so W_R is diagnosed at time $t-\Delta t$), and with the diagnosis of rain evaporation (acts as a negative feedback on the amount of rain-water and on the amount of water vapour; this is diagnosed at time $t+\Delta t$ for convenience since that is when the adjustments for condensation and evaporation are also made).

The adjustment to cloud-water then consists of

$$Q^*_{C\,ijk} = Q^*_{C\,ijk} - 2\Delta t \times AA^{t-\Delta t}_{ijk} \qquad (2.52)$$

where AA is the sum of the autoconversion and accretion rates. The adjustment is of course stopped if Q_C^* becomes zero. The amount of water taken from Q_C^* is added to Q_R^*.

(10) Adjust for condensation and evaporation

Using the pressure field at time t, the temperature T^* is calculated from θ^*,[1] and from that is obtained the saturation

---

[1] The pressure at time $t+\Delta t$ should strictly be used, but is not yet known. Wilhelmson and Ogura (1972) have shown that the dynamics are not seriously affected by using the previous pressure value.

mixing ratio Q_{vs}^* using (2.12). If this is smaller than Q_v^*, an amount of water is condensed to bring the air just to saturation. In a manner similar to Asai (1965), the effect of the addition of latent heat on increasing the saturation mixing ratio is included. We approximate the saturation mixing ratio as a locally linear function of temperature:

$$Q_{vs}(T^* + \Delta T) = Q_{vs}^* + \beta \Delta T$$

where

$$\beta = \frac{\partial Q_{vs}}{\partial T}$$

is determined using the formulae for saturation vapour pressure in Appendix B. Then for a change of Q_v^* to $Q_v^* + \Delta Q_v$, and of Q_{vs}^* to $Q_{vs}^* + \Delta Q_{vs}$, we have the following three equations:

$$\begin{aligned} Q_v^* + \Delta Q_v &= Q_{vs}^* + \Delta Q_{vs} && \text{exact saturation} \\ -C_p \Delta T &= L_{vw} \Delta Q_v && \text{latent heat release} \\ \Delta Q_{vs} &= \beta \Delta T && \text{change in } Q_{vs} \end{aligned} \tag{2.53}$$

The solution for the change in water vapour mixing ratio is

$$\Delta Q_v = \frac{Q_{vs}^* - Q_v^*}{1 + \beta \frac{L_{vw}}{C_p}} \tag{2.54}$$

Since Q_{vs} is not a linear function of temperature the new values of Q_v and T will not represent exact saturation, but will be very close.

In the case of subsaturation - Q_{vs}^* larger than Q_v^* - we must allow cloud and rain to evaporate. If any cloud is present, it is immediately evaporated until all gone or until saturation is reached. (The above equations are applicable here, too.) If the air is still subsaturated then the evaporation rate for rain based on Q_R^*, Q_V^* and T^* is calculated from (2.10) and applied for a time of $2\Delta t$ again subject to evaporating all the rain or reaching saturation. If the mixing ratio of rain-water is smaller than 2×10^{-8} - corresponding to a median radius of 50 μm for the Marshall-Palmer distribution - it is just treated as cloud and evaporated immediately. Otherwise, tiny amounts of rain-water spread throughout the entire model and never evaporate completely.

3. MODEL VALIDATION AND COMPARISONS AMONG DIFFERENT DOMAIN GEOMETRIES

This chapter has the following three objectives:

(1) To validate the model.

(2) To compare results among various two-dimensional and three-dimensional versions of the model.

(3) To compare results between uniform and nonuniform grid spacings in x.

The model validation is required because after designing and programming such a large model (almost five thousand lines of code) we can never be quite sure that there are no mistakes in the program, let alone the mathematics or physics. Gross errors are easily detected, but to truly have confidence in the model it must be compared either with the real world or with results from some other apparently valid model. We will compare our simulations of a cumulus cloud with those of Soong and Ogura (1973), hereafter referred to as SG.

SG were interested in the differences between two-dimensional models of the slab-symmetric and axisymmetric kind. This conveniently allows us to combine objectives (1) and (2) by comparing the results from our two- and three-dimensional models amongst themselves and with SG's results. Objective (3) can be achieved using any one of our models.

3.1 Models Used

The SG models will be called SG2 for the slab-symmetric, and SG3 for the axisymmetric since it has fully three-dimensional geometry.

Our main models will be called 2D for the two-dimensional slab-symmetric, and 3D(2) and 3D(3) for the three-dimensional models having respectively 2 and 3 computed pressure points in the y direction. These 3D models have domain WIDTHS of 12 km. Two other models, called 3D(2)-W6 and 3D(2)-W24 have domain WIDTHS of 6 km and 24 km respectively. A final model, 3D(2)-DX400, differs from 3D(2) only in that it uses a uniform grid spacing of 400 m in x rather than the nonuniform spacing used for all our other models.

The SG2 and SG3 models use essentially the same set of equations as we do. The main differences in the mathematics and numerics are enumerated below:

(1) Their equations are formulated in terms of a vorticity equation rather than individual velocity components. Because they neglect one pressure term, claimed to be of small magnitude, they need not diagnose the pressure field explicitly.

(2) Kessler's (1969) scheme also forms a basis for their microphysics, though with slightly different expressions for rain-water evaporation and terminal velocity. Their autoconversion threshold is 1.0 g kg^{-1} compared with our 1.0 g m^{-3}.

(3) Their numerical scheme uses forward time-stepping and upstream or modified-upstream space differencing. This introduces strong implicit diffusion into the model.

(4) Their parameterization of <u>explicit</u> diffusion is similar to ours, but with a coefficient k_D of 0.20. We found it necessary to use a k_D of 0.50 in order to get comparable results between 2D and SG2 - showing how strong their implicit diffusion is. In fact, a higher value could have been used to reduce the peak vertical velocity for 2D, but 0.50 seemed quite high enough.

(5) SG use rigid, free-slip conditions on both horizontal and vertical boundaries. We use the same (taking the drag coefficient, C_D, as zero), except on the lateral boundaries in x where $\partial w/\partial x$ is set zero, and u is only approximately zero.

(6) They use a domain of 12.8 km height and 26.0 km length (SG2) or diameter (SG3), with a constant grid spacing of 400 m in both the vertical and horizontal. We use a domain of 12.4 km height and 26.8 km length,[1] with constant Δz of 400 m, but stretched co-ordinates in x with a central spacing of 400 m increasing to about 1400 m at each end. (This reduces the number of grid-points in x to

---

[1] In our models the u velocity components at each end of the domain in x are given by boundary conditions and not predicted. A LENGTH of 26.8 km and uniform spacing of 400 m in x allows the first predicted u velocity components, which are approximately zero, to be spaced 26.0 km apart, as are the rigid lateral boundaries in SG.

35 from the required 67 for the constant spacing of 400 m, used only in model 3D(2)-DX400.)

For our main three-dimensional runs the domain WIDTH is only 12 km, rather than 25.6 km, so that the next grid-point away from the central plane is not too far from the cloud. However, models 3D(2)-W6 and 3D(2)-W24 use WIDTHs of 6 km and 24 km respectively.

(7) They and we both use a time-step of twenty seconds; we restart after every thirty time-steps and average the fields from the latest two times. We integrate to 39.3 minutes and compare that with their results out to 40.0 minutes.

The base-state profiles of relative humidity, temperature, and equivalent potential temperature are shown in Fig. 3.1. From 25°C at the ground, the temperature decreases dry-adiabatically to a height of 800 m, and then at the rate of 6.0°C per kilometre. This gives conditional instability below about 4 km. The relative humidity increases from 70% at the ground to 90% at 800 m, then decreases at the rate of 7.5% per kilometre to a minimum of 30% at 8.8 km and above. The resulting θ_e profile shows potential instability below about 3.5 km.

To set off the cumulus cloud, the models are all initialized with an excess potential temperature perturbation of the form

$$\theta' = 0.5\left[1 - \left(\frac{z_0 - z}{z_0 - \frac{\Delta z}{2}}\right)^2\right]\left[1 - \left(\frac{x - x_c}{x_0}\right)^2\right]$$

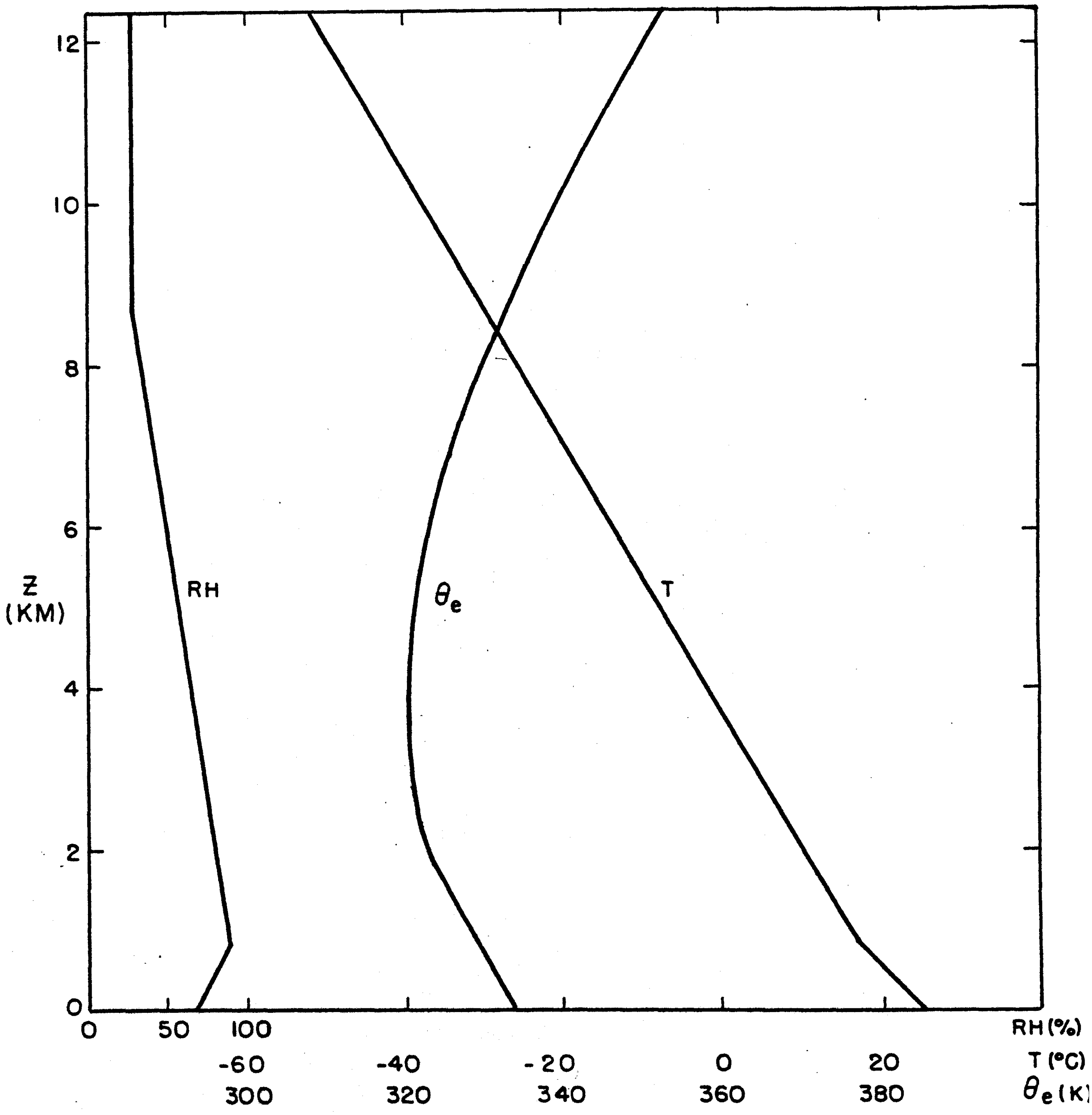

Figure 3.1. Base-state profiles of relative humdity (RH), equivalent potential temperature (θ_e) and temperature (T) used for the runs in Chapter 3.

which has a peak value of 0.5 K at $z = z_0$ (1000 m) and $x = x_c$ (the centre of the model). The perturbation falls off to zero at a horizontal distance of x_0 (1200 m) from the centre. Within this excess temperature region, and one grid-point beyond it in x and z (but not in y for our 3D models) for $z \geqslant 1000$ m, the relative humidity is set to 100%. Thus, condensation will occur immediately as the bubble starts to rise.

3.2 Results

For all runs a cumulus cloud did develop, reaching its peak vertical velocity after about twenty minutes. Thereafter, a combination of water loading and entry into a comparatively dry and conditionally stable environment weakened the updraft and the thermal buoyancy. The rain fell out and there were weak Brunt-Väisälä oscillations in the vicinity of the original cloud base. A complete description of the results will not be given here, since they are similar to those described by SG. Rather, we will concentrate on comparing the time variations of the maximum values of w, θ' and Q_R on the central axis of the cloud for the various models, thus accomplishing objectives (1) and (2) together.

Fig. 3.2 shows the variation of the maximum vertical velocity. In spite of the large value of 0.50 for k_D, the peak of 8.6 m s^{-1} for 2D is still significantly larger than the peak of 6.9 m s^{-1} for SG2.[1] However, the similarity between the 2D

---

[1] In initial tests, a value for k_D of 0.42 had been used, resulting in an even higher peak w of 9.9 m s^{-1} for the 2D model.

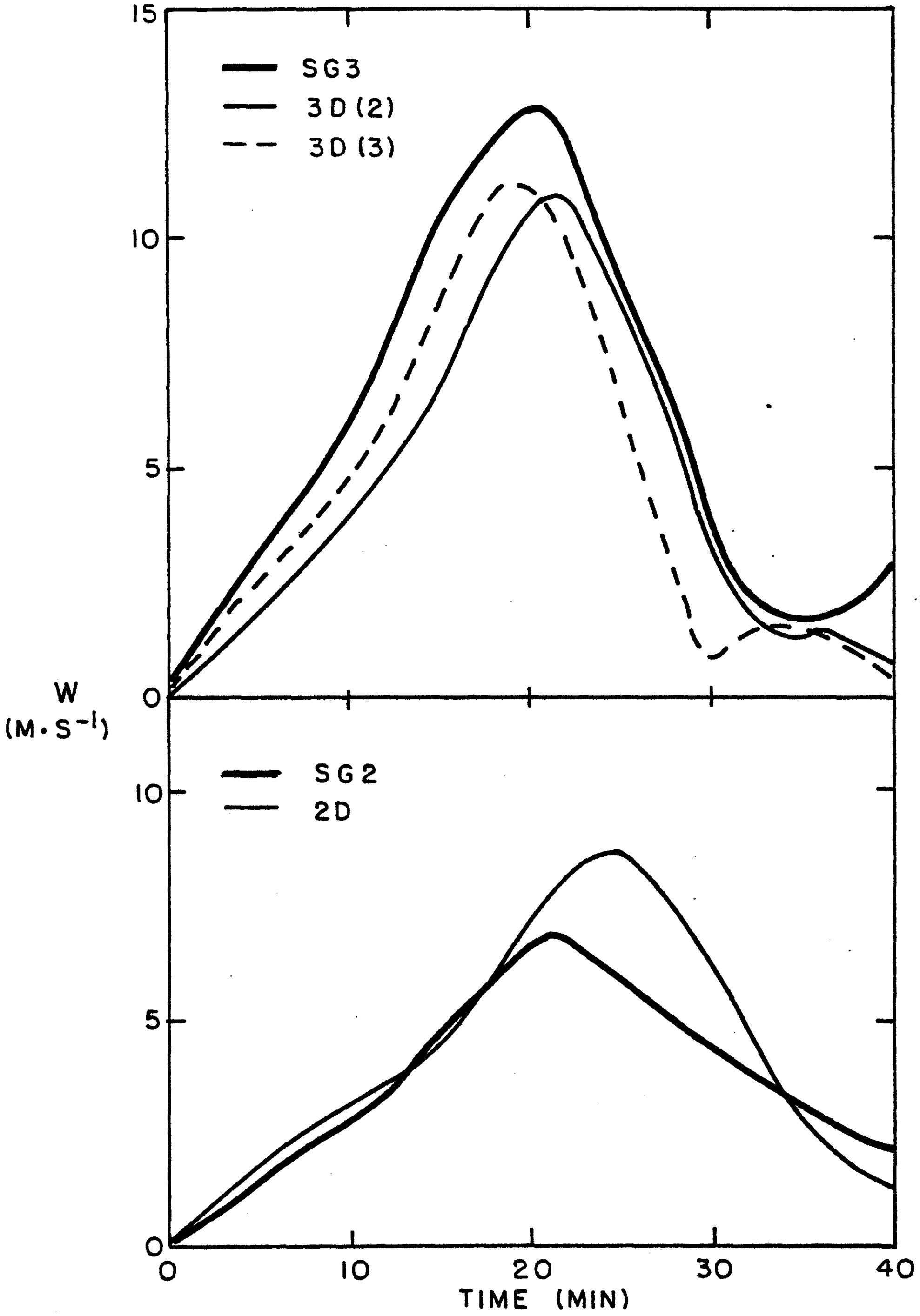

Figure 3.2. Time variation of maximum vertical velocity on the central axis of the cloud for the various models.

and SG2 results is heartening. The three-dimensional results, in the top of the figure, are also encouragingly similar. The 3D(2) peak w is 10.9 m s^{-1}, an increase of 2.3 m s^{-1} over the 2D value, yet the 3D(3) peak is only 0.3 m s^{-1} higher. This suggests that there is a significant improvement in going from the model 2D to the crudely three-dimensional model 3D(2), while further increases in complexity by increasing the number of points in y give somewhat smaller incremental improvements. The 3D(2) model is still significantly worse than SG3, though, with a peak of 2 m s^{-1} less.

Fig. 3.3 shows the variation with time of the maximum θ'. Again, the graphs are very similar for the comparable models. The disparity after 30 minutes may be due to our using a maximum θ' in the region of the original cloud base, where Brunt-Väisälä oscillations are occurring, rather than at the top of the cloud which SG seem to have used. It is not known why the 3D(2) and 3D(3) peak temperatures are higher than for SG3, but possibly the implicit diffusion in the SG model more strongly smooths out the local maximum in the cloud.

The time variation of the maximum rain-water mixing ratio is given in Fig. 3.4. The higher peak of 2D over SG2 is due to the stronger and longer updraft in 2D. The reason for the higher 3D(2) peak than 3D(3) is probably the later occurrence of the peak updraft for 3D(2), allowing more time for more rain to form.

As SG pointed out, the difference in initial acceleration

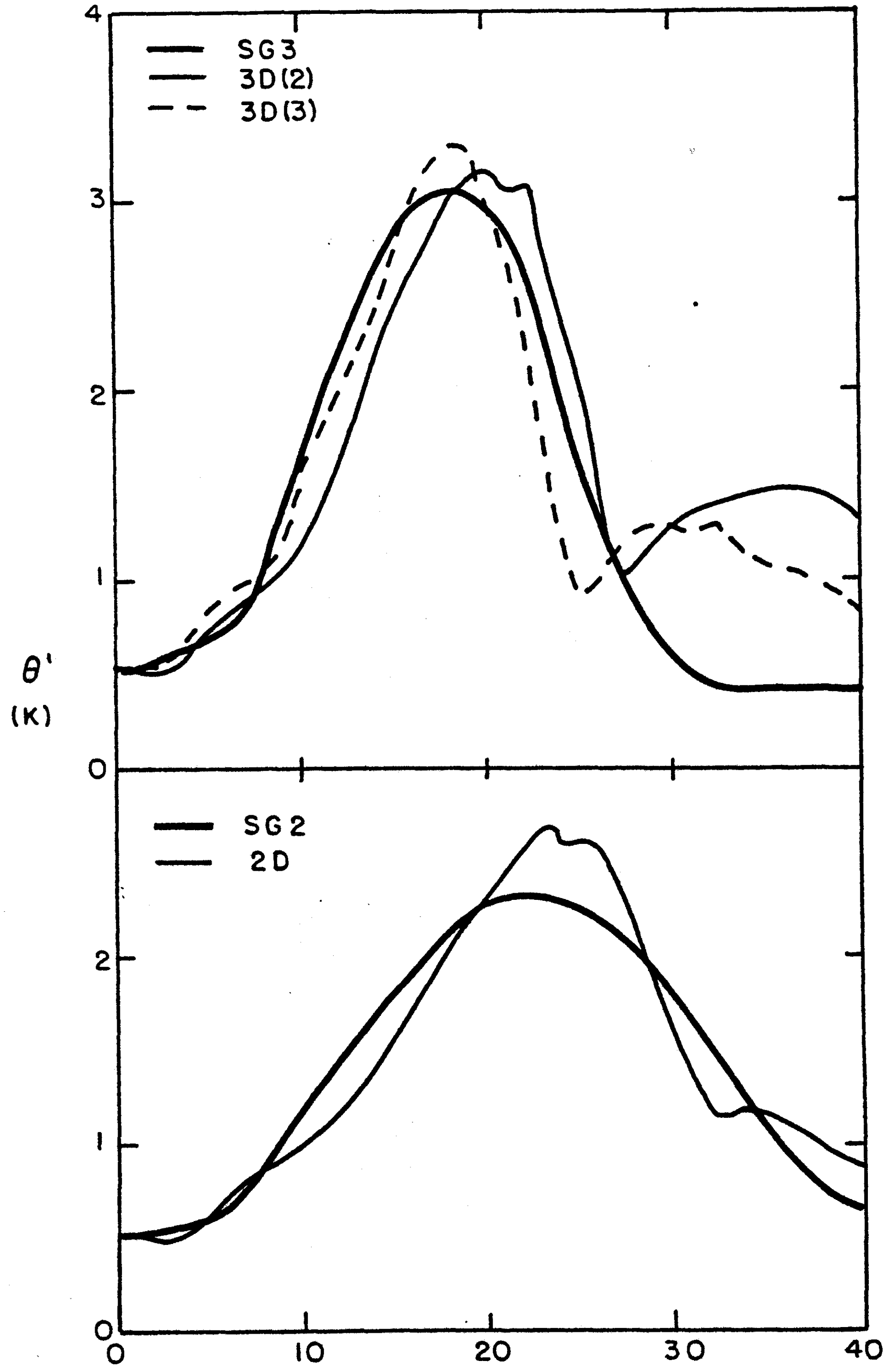

Figure 3.3. Time variation of maximum potential temperature perturbation on the central axis of the cloud for the various models.

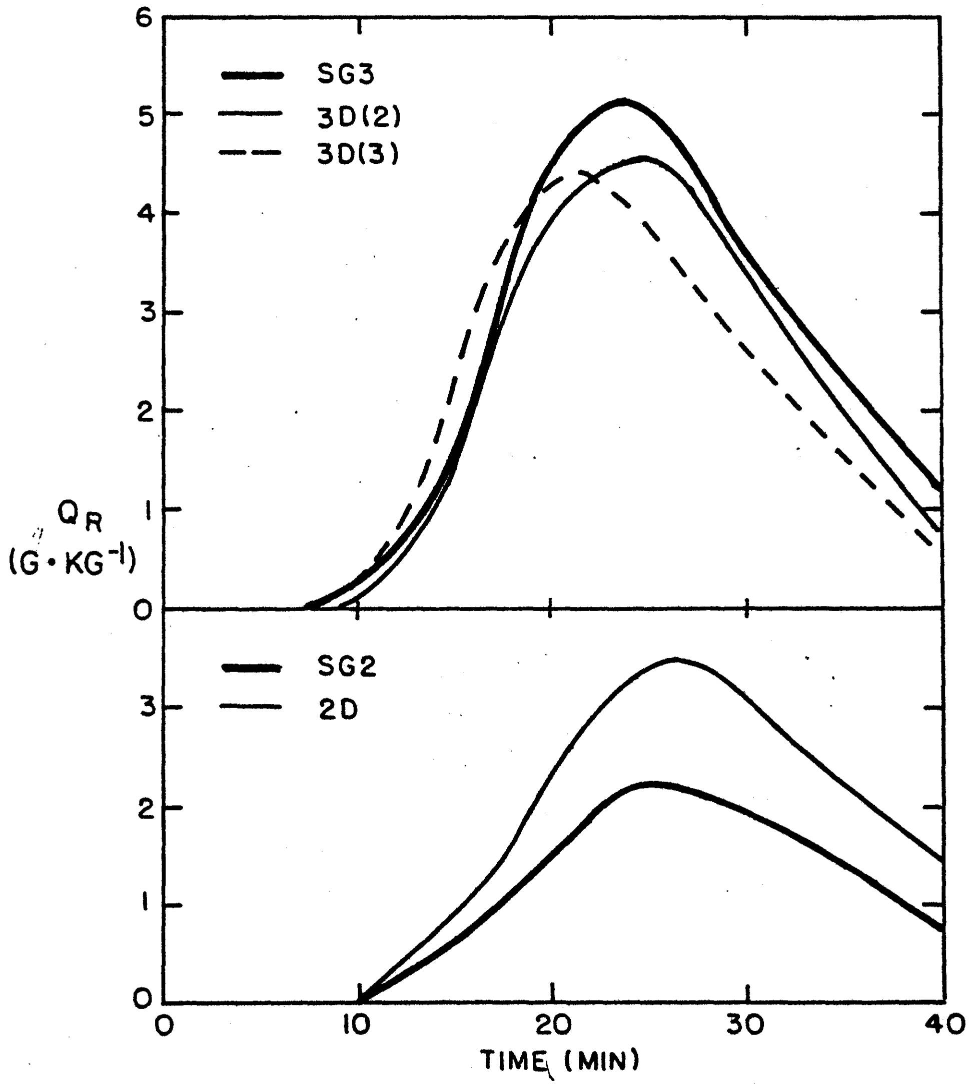

Figure 3.4. Time variation of maximum rain-water mixing ratio on the central axis of the cloud for the various models.

upwards of the bubble can only be due to the different pressure forces for the different geometries. For the slab-symmetric geometry, as compared to the axisymmetric, there is a stronger retarding pressure-gradient force (PGF) which both lessens the upward acceleration and forces a stronger compensating subsidence and environmental warming. Even our crude three-dimensionality lessens the retarding PGF and allows the cloud to develop more strongly.

To illustrate this effect, Table 3.1 gives the values of the PGF at the initial time, in units of equivalent degrees kelvin, on the axis of the cloud at a level of 1.2 km where the vertical velocity develops its initial maximum. (For comparison, the initial net buoyancy force at that level including the virtual temperature effect is +0.755 K.) Note that SG computed the PGF for their models as a residual in the vertical equation of motion; ours was computed explicitly.

We see that as expected the strongest retarding PGF is for the two-dimensional models. It is almost as strong for model 3D(2)-W24; this has its first vertical velocity and pressure grid-point a distance of 8 km in the third dimension away from the initial perturbation - so far away that there tends to be little interaction between the two planes. (For a very large WIDTH we would essentially have two independent 2D models side by side.) Proceeding down Table 3.1 we find that the retarding PGF lessens as this first grid-point outside the initial perturbation comes closer.

TABLE 3.1. The PGF at the initial time, the vertical velocity at 10 min, and the time and value of the peak vertical velocity, for all the models.[a]

Model	WIDTH (km)	Δy (km)	PGF (K)	$w_{10\ \mathrm{min}}$ ($\mathrm{m\ s^{-1}}$)	t_{peak} (min)	w_{peak} ($\mathrm{m\ s^{-1}}$)
SG2	-	∞	-0.55	2.7	21	6.9
2D	-	∞	-0.522	2.8	24.7	8.4
3D(2)-W24	24	8	-0.516	3.1	22.7	10.3
3D(2)	12	4	-0.496	3.8	22.0	10.9
3D(3)	12	2.4	-0.463	4.9	18.8	11.2
3D(2)-W6	6	2	-0.444	5.0	18.8	10.4
SG3	26.0[b]	1.2[c]	-0.42	5.8	20	12.9

[a] Model 3D(2)-DX400 has essentially identical results to 3D(2).

[b] The diameter of a cylinder rather than the width of a box.

[c] This number corresponds to the other Δy's since it is the distance in all horizontal directions to the first grid-point outside the initial perturbation.

Those models with the smaller initial retarding PGF's have a correspondingly faster initial increase in vertical velocity. This can be seen in the fifth column of Table 3.1 which gives the maximum vertical velocities at ten minutes. Thereafter, non-linear effects take over, and the upward motion is limited by a combination of liquid water drag, loss of buoyancy due to penetration into a stable layer, and loss of buoyancy due to mixing and dynamic entrainment of dry, subsided environmental air. The clouds which initially grow faster tend to reach their peak velocities earlier, as shown in the last two columns of Table 3.1. But the values of the peaks are dependent on other factors. In particular, model 3D(2)-W6 has a lower peak than model 3D(3) although at the same time. Apparently the closeness of the side walls in 3D(2)-W6 encourages recirculation of the dry subsided environmental air into the cloud more than in 3D(3), thus reducing the latent heat release. Both models have a peak temperature perturbation at 17.8 min, but the former is 2.97 K and the latter 3.23 K.

Comparing the peak vertical velocities among models 3D(2)-W6, 3D(2), and 3D(2)-W24, we see that there is a trade-off between using a small WIDTH which reduces the retarding PGF but increases recirculation and mixing of the environmental air into the cloud, and using a large WIDTH which has the opposite effects. Somewhere in the region of a WIDTH of 12 km the peak vertical velocity is maximized.

Finally, to accomplish objective (3) we must compare the results of 3D(2) and 3D(2)-DX400. Since both models have the same resolution at the centre of the cloud we would expect the smallest differences there, and the largest differences at each end of the domain in x where 3D(2) has the poorest resolution. This was the case. Within the cloud the fields were virtually identical after 20 min - the maximum vertical velocities were both 10.3 m s^{-1} and the maximum temperature perturbations were 3.10 K and 3.13 K for 3D(2) and 3D(2)-DX400 respectively. Far away from the cloud there was naturally more detail in the fields of the latter model. There was also less subsidence and environmental warming than for the nonuniform model; this may have been due to the approximately rigid lateral boundary in x being a kilometre farther away in the uniform model.

At 39.3 min, the end of the run, the fields were still very similar in the cloud region, although there were now Brunt-Väisälä oscillations occurring which were out of phase in the two models. To indicate how small the differences had been, the accumulated rainfall beneath the cloud centre at this time was 20.62 mm for 3D(2) and 21.19 mm for 3D(2)-DX400, a difference of less than 3%.

3.3 Conclusions

The conclusions of this chapter may be stated in terms of the original objectives:

(1) On the basis of comparisons with the published cumulus cloud simulations of Soong and Ogura (1973) our model in its various versions appears to be valid; that is, it is producing reasonable and realistic results.

(2) In terms of peak vertical velocity reached, the simplest three-dimensional version of the model is significantly better than the two-dimensional version at simulating a cumulus cloud, but still significantly worse than a fully three-dimensional model. A further increase in the number of grid-points in the third dimension produces less incremental improvement.

Because of a tradeoff between the effects of the retarding pressure gradient force and of mixing and recirculation of environmental air there is a broad maximum of peak development of the simulated cloud for a domain WIDTH of around 12 km in a model with N = 2.

(3) There is very little difference between clouds simulated using uniform and nonuniform grid spacings in x.

4. SIMULATION OF THE CONVECTIVE SYSTEM OF 14 MAY 1970

This is the system on which the observational studies of Sanders and Paine (1975) and Sanders and Emanuel (1977) were made, motivating this modelling study. Section 4.1 will briefly describe the synoptic situation, and the results obtained in those observational studies (hereafter referred to as SP and SE, respectively). In Section 4.2 the model setup and initialization for the simulation will be discussed. The results will be presented in Section 4.3. Section 4.4 considers some sensitivity tests.

4.1 Observations

The surface synoptic situation for 1800 CST on 14 May 1970 is shown in Fig. 4.1, taken from SP. A cold front was just entering the northwest corner of the National Severe Storms Laboratory (NSSL) mesonetwork; its associated frontal surface wind shift (SWS) moved steadily southeastwards through the network at about 24 km h^{-1} or 6.7 m s^{-1}, followed by a monotonic temperature fall from about 25°C to 15°C over an hour. At 40 kPa a pronounced short-wave trough was moving through the upper Great Plains with a weak extension into western Oklahoma and Texas.

The convective system associated with the front was observed by radar, by 44 surface stations within the network, and by a total of 42 upper air soundings (mostly to only 40 kPa)

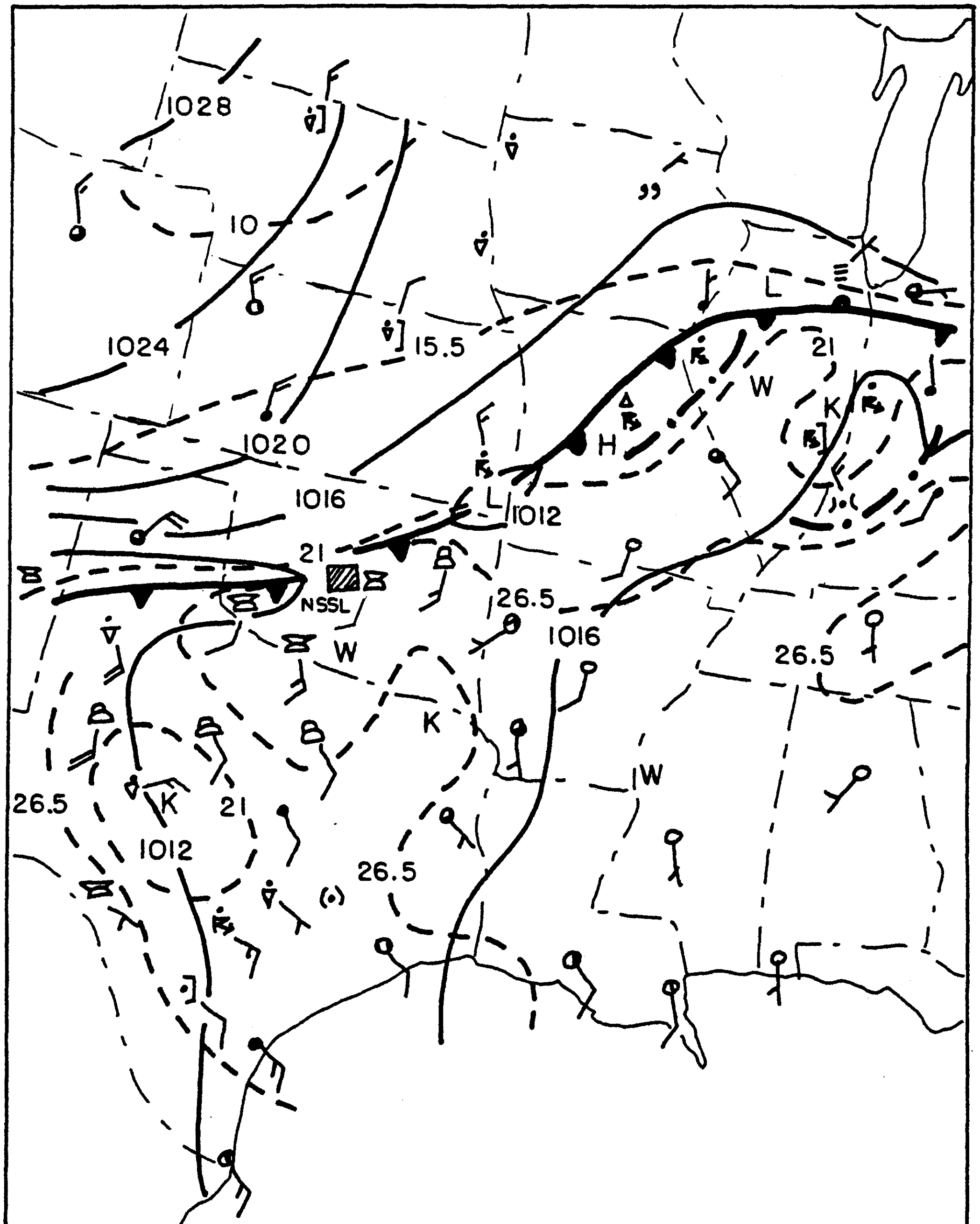

Figure 4.1. Synoptic situation at 1800 CST, 14 May 1970. Hatched area indicates location of NSSL mesonetwork. Solid lines are isobars (mb) of sea-level pressure; dashed lines are surface isotherms (°C). Letters L, W, and K indicate, respectively, centres of low pressure and warm and cold temperature. Front, instability line, wind, cloud amount, and present weather are indicated in standard synoptic notation. (Taken from Sanders and Paine (1975)).

during the five-hour passage of the front.

The radar observations indicated that lines of thunderstorms developed above the frontal surface. The cells were typically spaced about every 12 km along the lines, at least in the early stages of the system. Each line lagged behind the movement of the SWS, so once it was far enough back a new line would form, at intervals of forty-five minutes to an hour. But with time a large amount of precipitation debris from the lines accumulated, until by 2115 CST (almost seven hours after the first echoes) the radar detected precipitation of at least moderate intensity spanning a distance of 45 km behind and normal to the front. After that, "the echo area tended to broaden further and to lose the strong reflectivity gradient characteristic of the leading edges, while moving little as a whole" (SE).

SP located upper air sounding data in x[1] and p relative to the SWS, then took averages over 5 kPa layers in the vertical and over blocks of about ten balloons in the horizontal. The resulting data were subjectively analyzed over a grid with spacings of 5 kPa vertically and 8 km horizontally. The observations within the region up to 30 km behind the SWS were thought to be biased by representing too high a proportion of cumulus updrafts (not only would the balloons tend to be drawn into an updraft, but also they may have been intentionally launched to do this). The analyses made by SP and SE attempted to correct

---

[1] SP and SE actually used a co-ordinate system rotated 90° anticlockwise from ours. Our x is their $-y$, our u is their $-v$.

for such a bias.

Although direct estimates of the vertical velocity were available from the balloon ascent rates, the vertical velocity field obtained by the use of the continuity equation on the analyzed field of u, together with an assumption of two-dimensionality, was found to be much more reliable. Fig. 4.2, adapted from SE, shows the field of u and the corresponding field of ω. (SE's analysis technique differed from SP's in that linear trends in time were removed, all the data being adjusted to a time of 2000 CST).

The most striking feature is the updraft/downdraft doublet near 40 kPa and within 30 km behind the SWS, with the peak values corresponding to +2.7 m s^{-1} and -2.0 m s^{-1}. The second updraft area in the upper left corner is probably spurious since all data for that region came from after 2000 CST and needed to be extrapolated backwards in time, resulting in the large positive region in the u field near 55 kPa.

In the u field the vertical structure ahead of the SWS is apparently due to some kind of gravity wave and will be commented on later. Strong convergence is evident near the ground in the region of the SWS, yet the divergence aloft, ahead of the maximum leftwards motion of about 10 m s^{-1}, is enough to produce the downdraft over the SWS. Inspection of the individual soundings in this region showed the divergence to be a persistent feature, and not an artificial result of the analysis techniques.

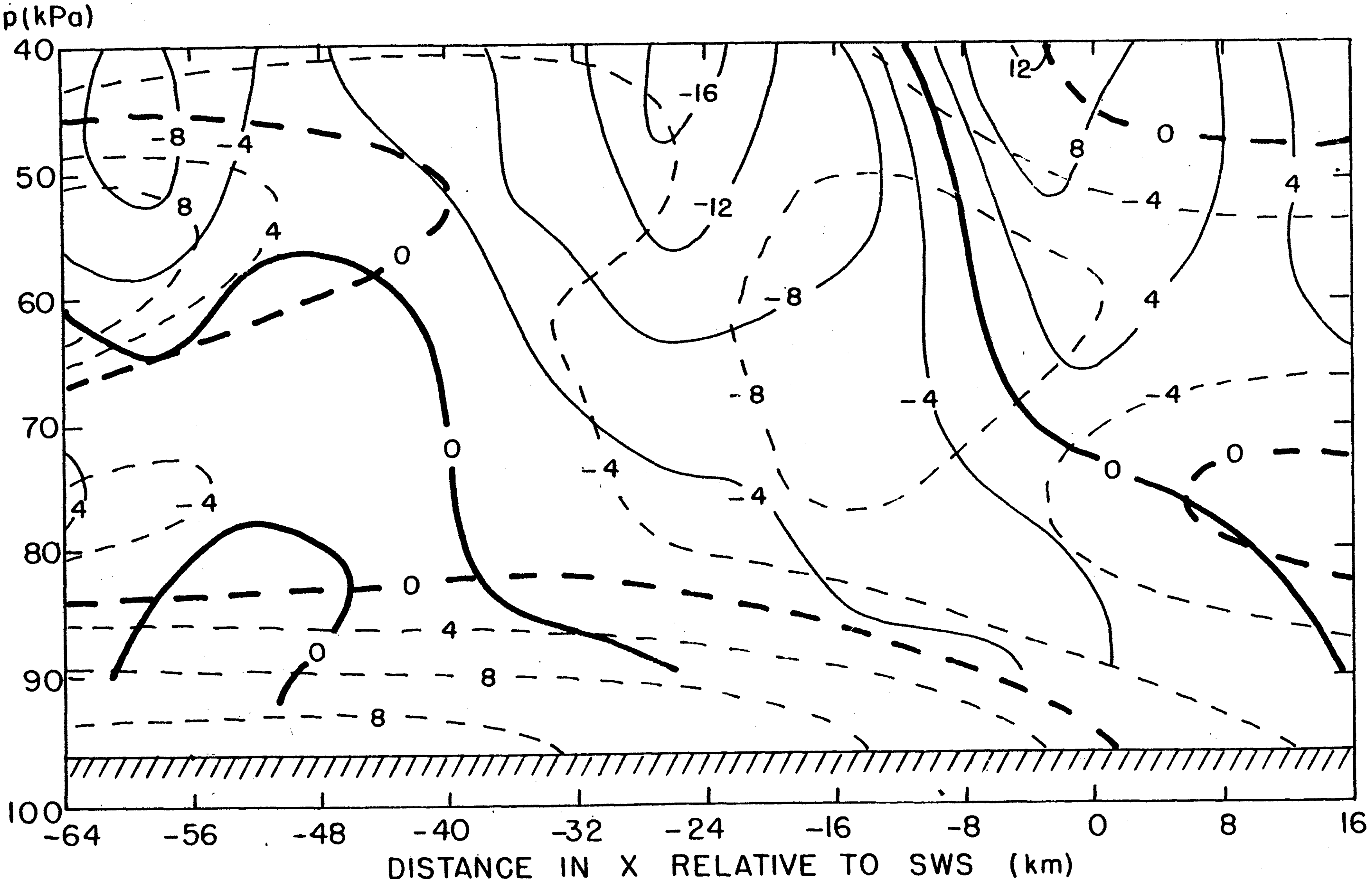

Figure 4.2. Fields of u (relative to the ground) and ω for 14 May 1970. u contours are dashed and in units of m s^{-1}. ω contours are solid and in units of Pa s^{-1}. Adapted from Sanders and Emanuel (1977).

SP conjectured, on the basis of an apparent source of water vapour and sink of potential temperature following the mesoscale motion, that the downdraft aloft was being driven by evaporative cooling at the tops of initial deep cumulus clouds set off by the surface convergence at the SWS. The accompanying updraft was driven by latent heat release in a region supposedly saturated on the mesoscale. In other words, they pictured the system as being like an "elevated sea-breeze circulation", with the updraft/downdraft doublet driven by the corresponding heating/cooling doublet.

SE further examined the time-dependent behaviour of the system. They noted the periodic development of new lines of convection already mentioned, and a change in character of the system in its later stages, with the development in its rear (about 20 to 60 km behind the SWS) of a strong circulation of air feeding forwards at about 75 kPa and rearwards at about 55 kPa. This circulation was near the base of an extensive mass of middle cloud debris from the system; its rear branch must have been a mesoscale downdraft aided by evaporation of precipitation from the middle cloud deck into relatively dry air (similar to that described for a tropical system by Zipser (1969)), and the forward branch was in the mesoscale updraft. With this recycling of air from the rear, the system apparently became disconnected from the SWS and its associated supply of high θ_e air, and slowly died.

It must be emphasized that there was little evidence of strong penetrative downdrafts from the convective cells in the system. The air beneath the frontal surface was not affected by the convection aloft, except perhaps for a small amount of in situ cooling by evaporation of rain, so the propagation of the SWS was frontal. For many other mesoscale convective systems the SWS is at the leading edge of penetrating downdraft air from the convection, so its propagation and the behaviour of the convective system are strongly interdependent.

4.2 Model Setup and Initialization

For the main simulation of the case of 14 May 1970 the following values for model parameters were used:

L = 100
M = 31
N = 2
LENGTH = 150 km (with stretching as shown in
HEIGHT = 15 km Figs 2.3 and 2.4)
WIDTH = 12 km
$k_a = 10^{-3}\ \mathrm{s}^{-1}$
$\rho_{CT} = 1.005\ \mathrm{g\ m}^{-3}$
$k_D = 0.42$
$d = 1.0$
$C_D = 0.002$

Other parameters and constants were given the values noted in either Chapter 2 or Appendix A.

The base-state profiles of temperature, relative humidity and equivalent potential temperature are shown in Fig. 4.3. From the surface pressure level of 97.5 kPa up to 40 kPa the profiles were based on the radiosonde sounding from Chickasha, released at 1831 CST; above that up to 12 km the sounding from

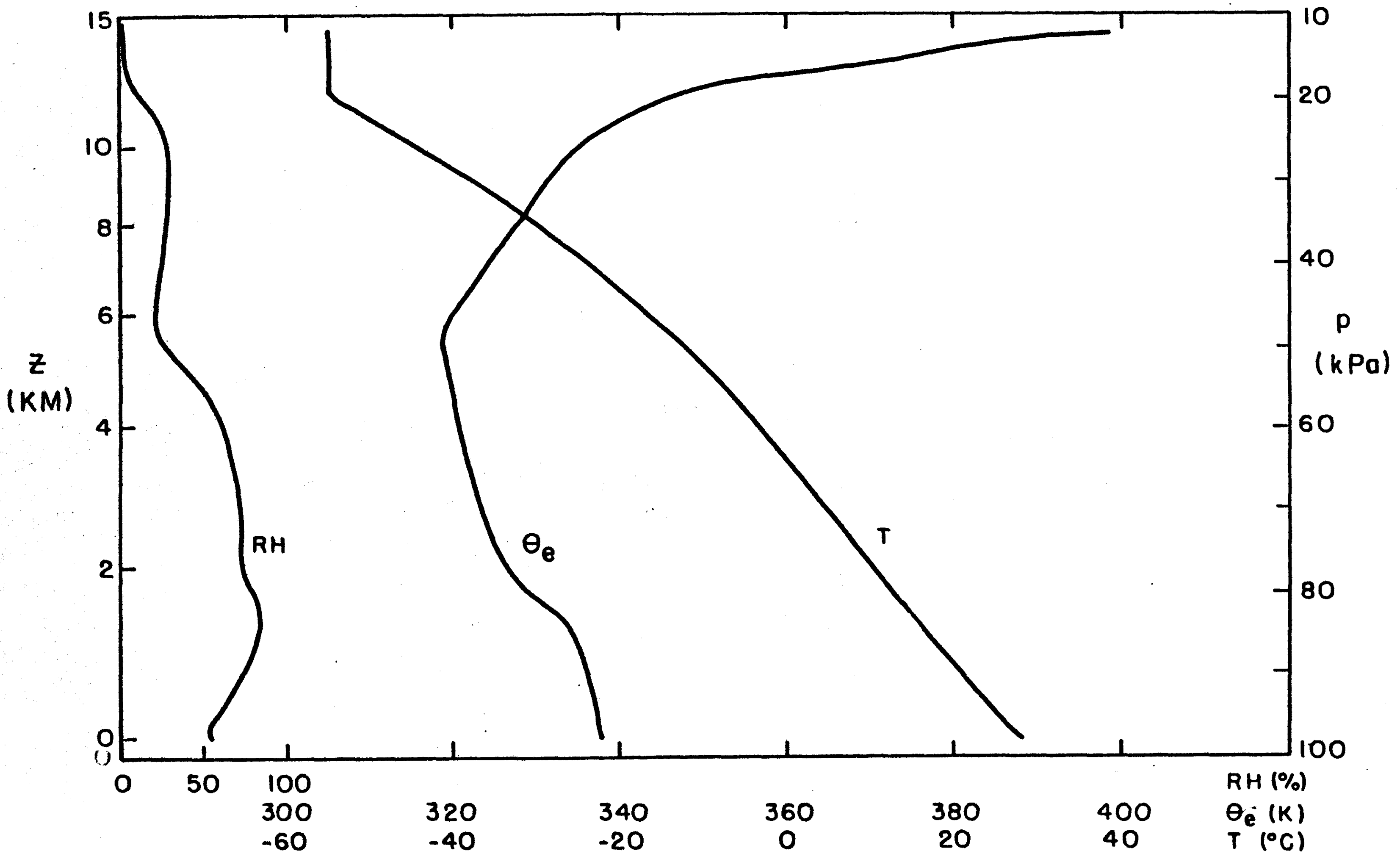

Figure 4.3. Base-state profiles used for simulation of the case of 14 May 1970. RH is relative humidity, θ_e is equivalent potential temperature, T is temperature.

Tinker Air Force Base for a nominal time of 1800 CST (00Z on 15 May) was used;[1] above 12 km an isothermal layer of -55°C was imposed to keep any convection from penetrating near the top of the model. (The actual tropopause was at a height of 12.65 km with a temperature of -64.2°C).

The profiles have conditional and potential instability up to about 50 kPa. It is only at that level that the air dries out significantly, so the sounding does not exhibit the dryness at a lower level of about 70 kPa that is often associated with severe convection. Below the lifting condensation level of about 1300 m the potential temperature is constant, as is characteristic of a subcloud convective boundary layer.

The measured wind components in the direction of 145° (transverse to the front) from the above soundings were all of small magnitude - the largest being about 6 m s^{-1} towards the front - so the base-state profile of u was taken to be zero everywhere.

The model was initialized with a crude representation of the pool of cold air beneath the frontal surface, based on observations of the structure of the actual front. Fig. 4.4

---

[1] For both soundings the rawinsondes were released an hour before the passage of the SWS so the profiles were typical of the air ahead of the system. Comparing them with SP's mean profiles (up to 40 kPa) centred about 40 min or 16 km ahead of the SWS, we find that the model temperature profile is almost the same near the ground but generally 0.5 K to 1.5 K colder aloft, and the model relative humidity profile is the same except for a region around 1500 m which is up to 15% more moist. (This moisture increase was intentional because the measured values were thought by SP to be too low in this region.)

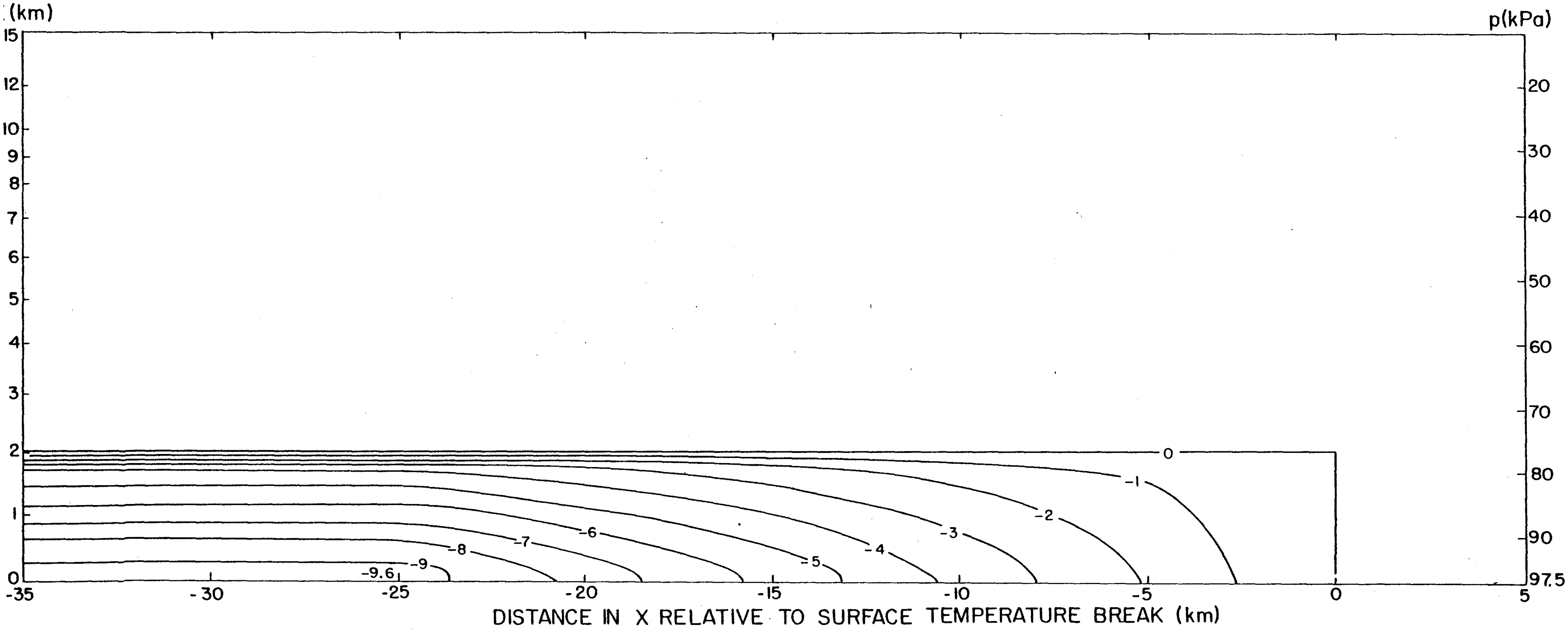

Figure 4.4. Initial field of θ'. Contour interval is 1 K. The point X = 0 in this figure was actually x = 110 km in the model.

shows the field of θ' used. From the leading edge of the cold air, at x = 110 km, θ' varied linearly over a distance of 25 km to a value of -10°C at the surface and -3°C at 2000m,[1] with a linear variation in z as well. Behind that, θ' remained constant with x. Simulating the relatively moist air behind the front, the relative humidity varied linearly from its base-state value at the leading edge to a value of 90% at x = 85 km, and was constant at 90% behind that.

To introduce some three-dimensional structure into the fields, and to help set off initial convection, a small area of excess moisture was added on the central plane only, just ahead of the cold air. The area was 2500 m long in x, and had Q_v set to its surface value of 12.5 g kg^{-1} up to a height of 1165 m, with the next level of 1443 m set to the saturation value of 12.3 g kg^{-1}.

Rather than attempting to initialize the model with a frontal wind structure, we simply set all velocity components to zero and allowed the model to develop its own wind fields in response to the strong forcing of the temperature fields.

4.3 Results

The model was run for a total time of 251.1 minutes, using

---

[1] Because the first temperature grid-point in the model is at 123 m the coldest perturbation temperature used there was actually -9.56°C. Similarly, the highest temperature grid-point below 2000 m is 1728 m, at which the coldest perturbation temperature was -3.95°C.

a time-step which varied due to numerical stability requirements in the range of 7 s to 20 s, but which was mostly 10 s. After every thirty time-steps the model was restarted from an average of the fields for the last two times to prevent the separation of solutions at alternate time-steps that is characteristic of the leapfrog method. These restart fields were saved on magnetic tape, at 51 separate times approximately five minutes apart.[1] All analysis was done on these.

Section 4.3.1 will describe the results overall, concentrating on the movement of the cold air, and the quasi-periodic development of convective cells at its leading edge. The time period from 107.3 min to 165.4 min will be examined in detail in Section 4.3.2. Space- and time-averaged fields for that period will be considered in Section 4.3.3.

4.3.1 Overall Description

As expected, the cold air immediately began to spread forward, with the horizontal temperature gradient at its leading edge strengthening considerably and a strong convergence zone developing there. Above 1300 m a compensating rearward flow (relative to the ground) developed, resulting in a wind shear in the lowest 2 km of about 4.4 m s^{-1} km^{-1} by 10 min, and 7.6 m s^{-1} km^{-1} by 17 min, after which it remained almost constant.

---

[1] Each restart cycle took approximately 1.5 min to compute on an IBM 360/95 computer, so the model was running at about one-third of real time.

The leading edge of the cold air exhibited a temperature break[1] (TB) structure, with little temperature variation ahead of the TB but a rapid drop of typically 4 K in the first 3 km behind it. The TB will be used as a reference point for the system. For computing purposes an objective definition of its position was: the first point x_i proceeding from right to left, at which

$$\frac{\theta'_{i+1,j,k} - \theta'_{i-1,j,k}}{x_{i+1} - x_{i-1}} > 1{\cdot}0 \text{ K km}^{-1}$$

was satisfied, for $j = 1$ (the surface) and $k = 2$ (the central plane).

Fig. 4.5 graphs the movement of the TB with time, relative to the ground. Over the entire run the speed averaged 8.4 m s^{-1} (compared with 6.7 m s^{-1} for the frontal SWS on 14 May) with not much variation in time. This speed was not of course known a priori, so the translation speed of the model domain (UTRANS) was intermittently varied during the run, in the range of 7 to 10 m s^{-1}, to keep the TB position near $x = 110$ km.

To some extent the pool of cold air can be considered to be a density current, so it is interesting to compare its speed with that given by laboratory investigations. Simpson (1969)

---

[1] A temperature break is often observed in surface thermograph observations during the passage of a cold front or thunderstorm-induced gust front. It is the point where the thermograph trace shows a sudden change in slope with the temperature commencing to fall quite rapidly.

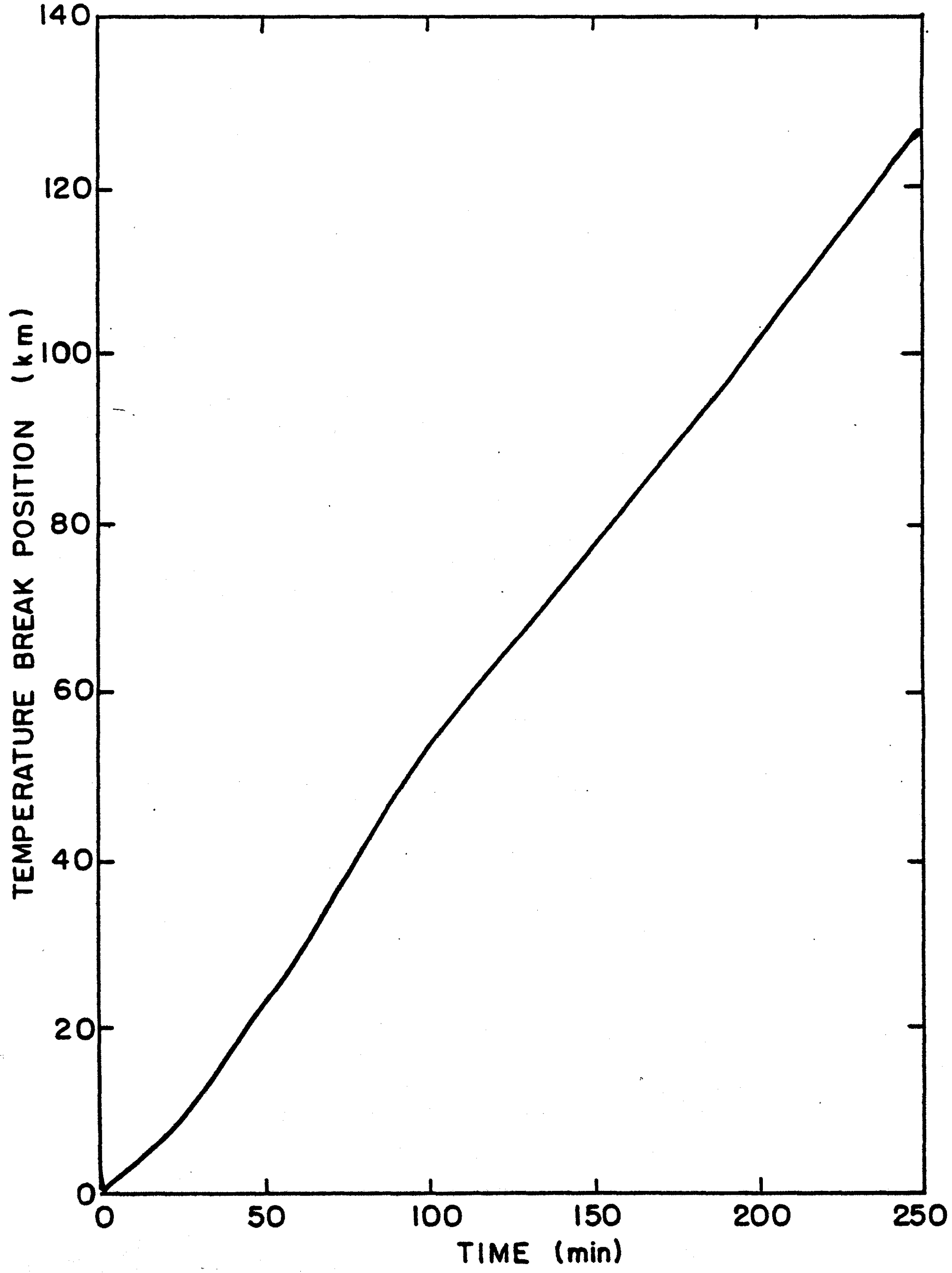

Figure 4.5. Position of the model temperature break in time, relative to the ground.

gave a formula

$$U = 0.78\left[\frac{\Delta\rho}{\rho} g d\right]^{\frac{1}{2}}$$

for the speed of a density current of depth d and excess density $\Delta\rho$ over the ambient density of ρ. Averaged fields over the period 107.3 min to 165.4 min of θ' (Fig. 4.26) and u (Fig. 4.20) show that the coldest surface air was about 14 km behind the TB, with an average θ' of -3.3 K in the 1300 m deep layer moving forwards relative to the ground. Substitution in the formula, using $\Delta\theta/\bar{\theta}$ as $\Delta\rho/\rho$, gives a speed of 9.2 m s^{-1}. This is reasonably close to the actual speed of 7.8 m s^{-1} over that time period, considering that the cold pool was more complicated than a classical density current with a homogeneous fluid of one density spreading out.

Above the cold air, a series of convective cells developed just behind the TB, primarily on the central plane, moved back relative to the TB, rained out, and merged into an anvil region well to the rear with a general cloud base of 6 or 7 km and top of 13 km.[1] To show the development and movement of the cells, updraft maxima embedded in cloud were located for each time that the model fields had been saved, and tracked in z and x relative to the TB. The paths of those maxima which showed continuity in time and reached at least 2 m s^{-1} are plotted in the x-t plane in Fig. 4.6. Significant convective cells are

---

[1] The 14 May system apparently generated more cloud debris since the middle cloud base observed visually behind it was only about 3 km.

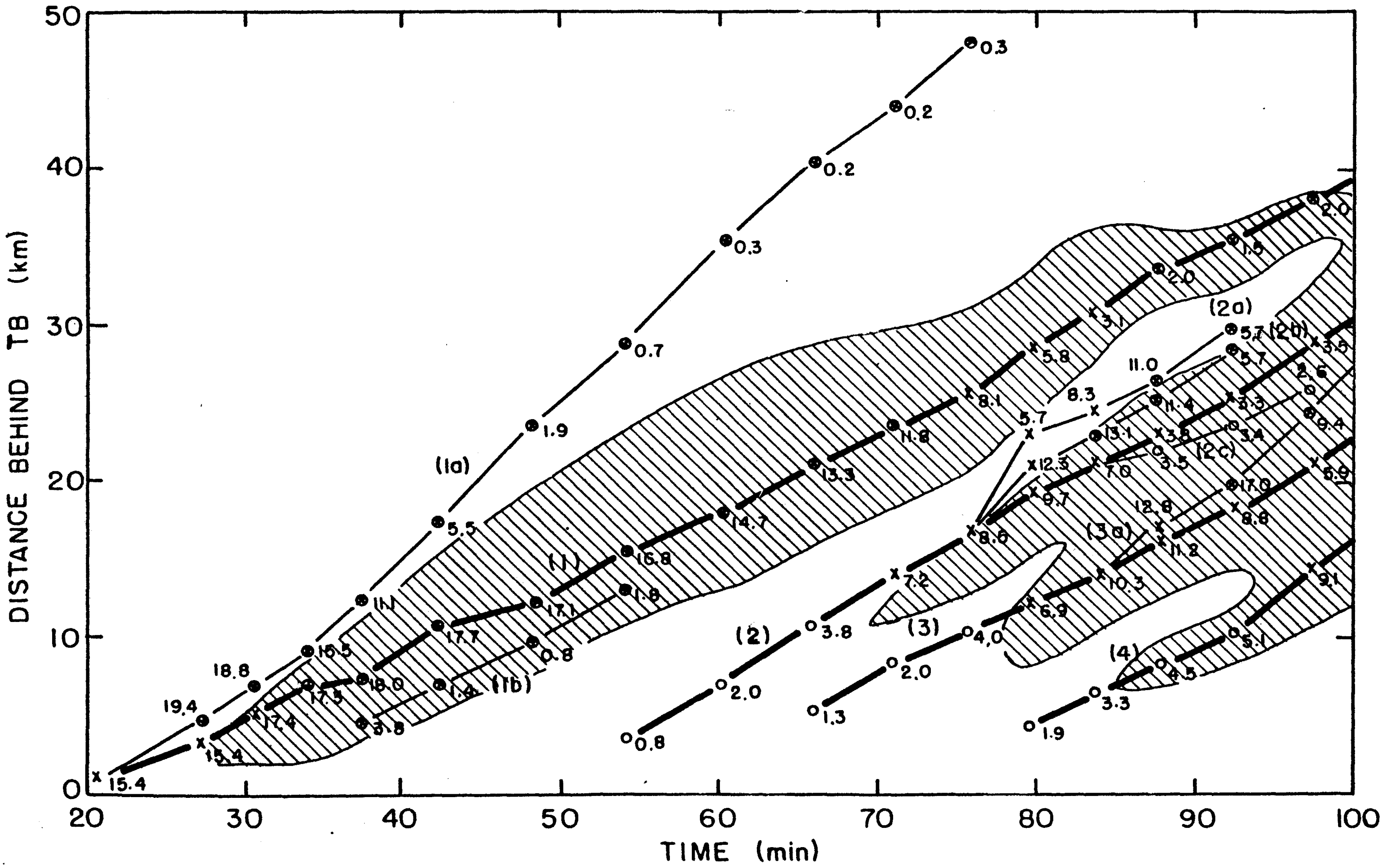

Figure 4.6. Movement of cell updrafts with time relative to the TB. Main cells are labelled (1), (2), etc., and connected with heavy lines (solid for central plane, dashed for side plane). Subsidiary updrafts are labelled (1a), etc., and connected with thin lines. Updrafts are in units of m s^{-1} with the position given by o for an updraft below 3 km, x for 3-6 km, and ⊗ for above 6 km. Areas of precipitation on the central plane with radar reflectivity > 20 dbz at the ground are cross-hatched.

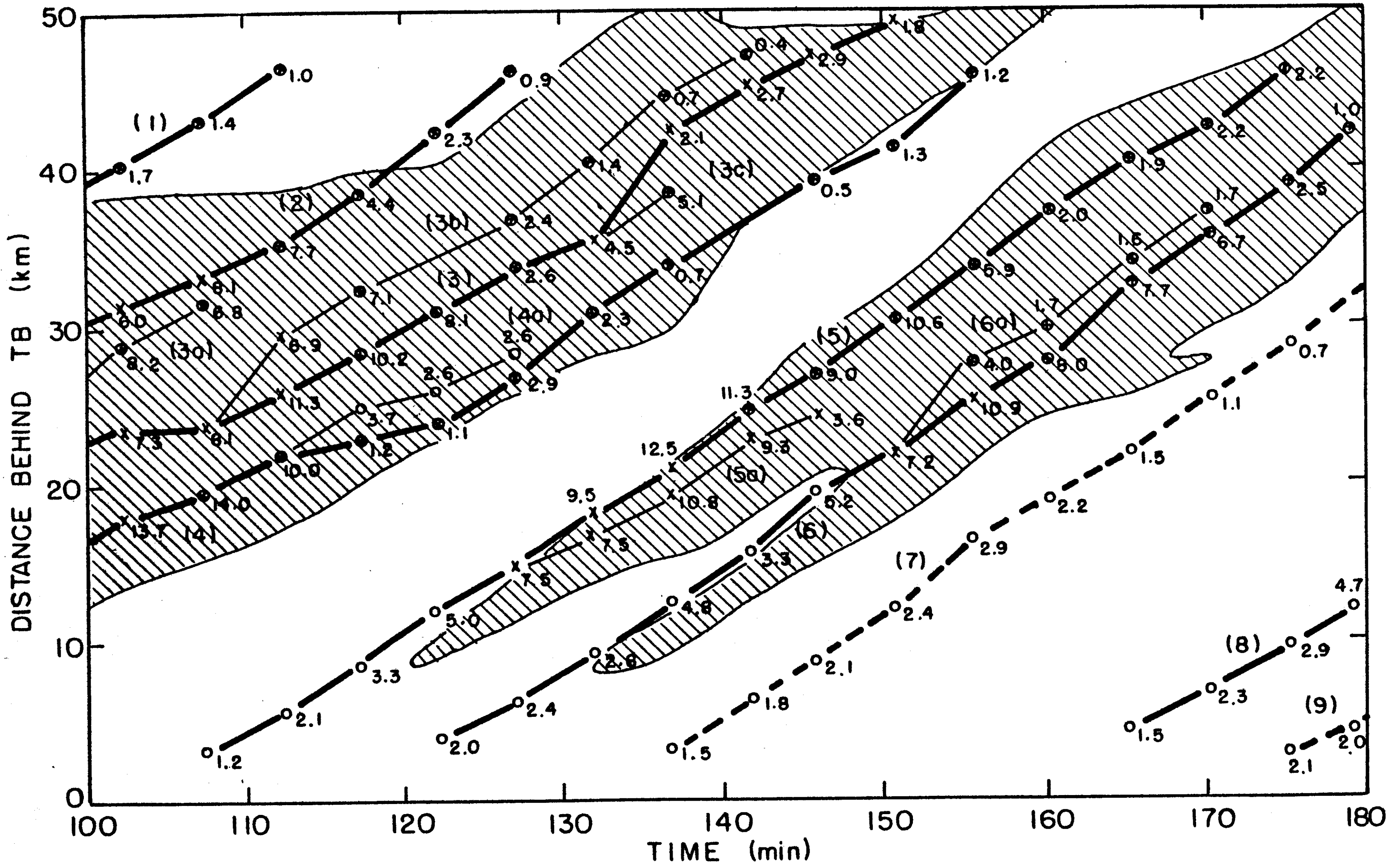

Figure 4.6 (continued)

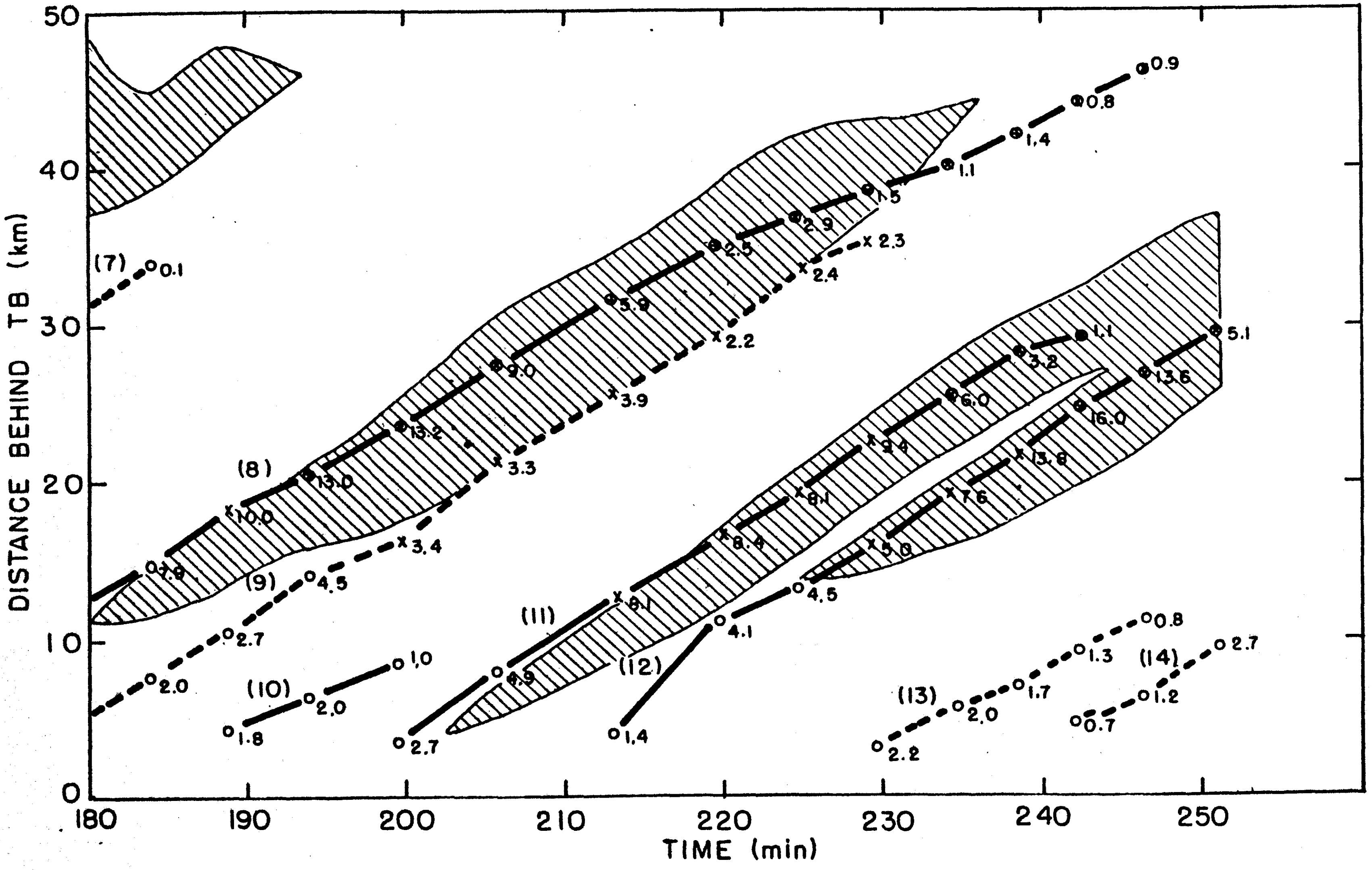

Figure 4.6 (continued)

numbered; subsidiary updraft maxima associated with the same cell (often caused by rain splitting the original maximum in two) are labelled as (2a) and so on.

The first cell, not shown before 20 min because the location of the TB was not yet well-defined, was the strongest. It reached a peak vertical velocity of 19.4 m s^{-1} at 27.2 min in a subsidiary maximum which rose into the anvil outflow behind the cell and moved rapidly back. Subsequent cells developing on the central plane were of rather uniform strength, reaching peak velocities of 11 to 17 m s^{-1} in the region 20 to 25 km behind the TB. Cells developing on the side plane were much weaker with peak updrafts reaching no more than 4.5 m s^{-1}. This is to be expected from theory. Without diffusion, cumulus clouds develop most strongly if they are narrow and cover a small area relative to the environment. As the fractional coverage increases, retarding pressure forces become stronger and the conversion of latent and potential energy to kinetic energy becomes less efficient. So the side plane developments, covering two-thirds of the domain in y, could not develop as strongly as those on the central plane covering only one-third.

The striking feature of Fig. 4.6 is that significant new cells formed at intervals of about 15 min, except that at intervals of about an hour (at 45 min, 95 min, 155 min, and 220 min) there were gaps and no significant cells developed.[1] The

---

[1] At 188 min cell (10) developed but only attained an updraft of 2.0 m s^{-1} and soon died. In the other gaps there were even weaker attempts at new cells which are not shown as they did not reach 2.0 m s^{-1}.

spacing in time of 15 min arises from a backwards movement of about 10.5 m s^{-1} relative to the TB and a spacing in x of about 9 km (if the old cell was closer it suppressed development of the new cell). This can be contrasted with the radar observations on 14 May which indicated lines to be spaced about 18 km apart in x, moving back at 5 m s^{-1} relative to the SWS, and developing at intervals of about 60 min. (Periodic cell developments have been reported elsewhere; for instance, Chalon et al (1976) described a multicellular hailstorm with new radar cells triggered by its gust front at intervals of 15 min in time and 5 km in space.)

Fig. 4.6 also includes hatching to indicate the regions on the central plane with radar reflectivity at the ground of greater than 20 dbz ($Q_R > 0.05$ g kg^{-1}, based on Kessler's (1969) expression for the Marshall-Palmer distribution). We see that the rain from successive cells tended to merge, particularly before 180 min, producing echo areas that were as much as 25 km across in x, in spite of the much smaller size of the individual cells. If we consider only these regions, then we have approximately the same periodicity in time (an hour) as was observed on 14 May, although they are more widely spaced because of the faster movement of the cells. The agreement in time may be fortuitous, however, since it is based on the hourly gap in simulated cell development which is shown in Section 4.4.3 to be sensitive to the magnitude of the parameterized diffusion. And examination of the original 14 May radar data showed little evidence of the echo lines being formed from smaller scale cells developing more frequently than an hour.[1]

The simulation was stopped at 251.1 min because it appeared that nothing further of interest would happen. New cells were continuing to develop with the same periodicity, but with a tendency for decreasing strength even though cell (12) did reach 16.0 m s^{-1}. The last two cells to develop were both on the side plane and the first had already succumbed.

The general weakening of the system in spite of a continuing supply of moist unstable air with base-state profiles was caused by gradual warming up of the pool of cold air and hence lessened convergence and upward motion at the TB. For instance, at 107.3 min the coldest surface temperature perturbation on the central plane was -8.4 K, by 251.1 min the coldest was only -5.8 K. This warming was due to vertical diffusion and will be discussed further in Section 4.3.3.

If it were not for the warming up of the cold pool the system would probably have maintained a quasi-steady state, with new base-state air continually feeding into the model from the right, interacting with the cold pool to produce convection, then streaming out at the left. (The anvil debris from the convection reached the left edge of the domain, 110 km behind the TB, by 165.4 min.)

---

[1] Meneeley's (1972) Fig. 13, showing cell developments and motions on 14 May, does have an example of new cells developing at approximately 15 min intervals: near 290°/40 nm at 1830, 1840, 1900, and 1920 CST.

4.3.2 The Period From 107.3 to 165.4 Minutes

This time period has been chosen for detailed study because it is long enough after the initial time to be little affected by the transient adjustments due to the unbalanced state of the initial fields, and because the events during it are typical of the entire simulation, including three new cell developments (the third being on the side plane), a gap, then a fourth cell just developing at 165.4 min.

To show what happens during the time period we will use a series of figures at approximately 15 min intervals, depicting for each plane the vertical velocity field, cloud extent, and rain (Section 4.3.2.1). We will then concentrate on the particular time of 136.8 min and examine other fields such as temperature, pressure, and horizontal velocities (Section 4.3.2.2). Mostly the region from 5 km ahead of the TB to 35 km behind the TB will be considered, since this encompasses the most interesting phenomena. However, some fields will also be shown for 35 km to 75 km behind the TB. Little of interest happens elsewhere in the model domain.

4.3.2.1 Cloud, Rain, and Vertical Velocity Fields

Fig. 4.7 shows the situation for the first time of 107.3 min, (a) being for the central plane and (b) for the side plane. The vertical velocity component is in units of m s^{-1} with some spot values marked; the heavy scalloped lines enclose

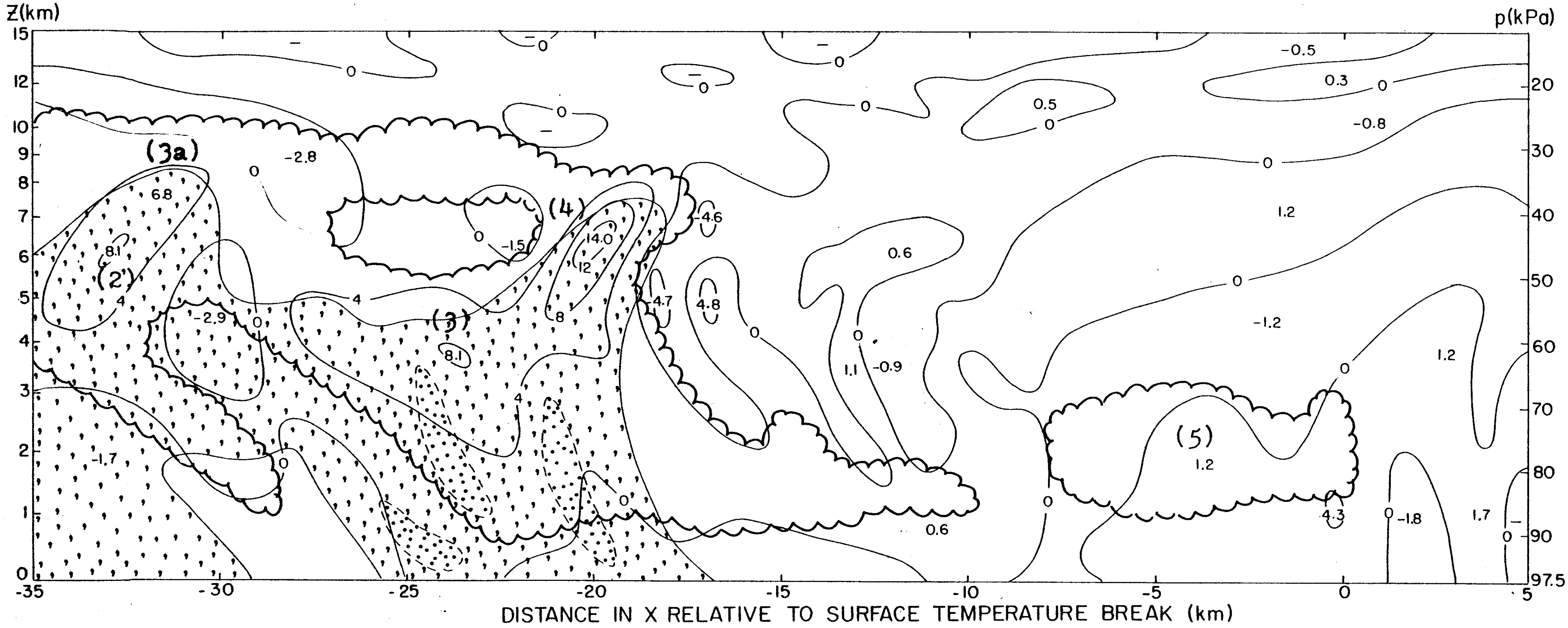

Figure 4.7. (a) Cloud, rain, and vertical velocity fields on the central plane at 107.3 min. Cloud outlines (enclosing $Q_c > 0$) are scalloped, areas of rain > 50 dbz are dotted and from 30 to 50 dbz covered in commas. The vertical velocity is in m s^{-1} with contour intervals of 4 m s^{-1} (solid) and optional intervals of 1 m s^{-1} (dashed). Updraft maxima are labelled with numbers corresponding to Fig. 4.6.

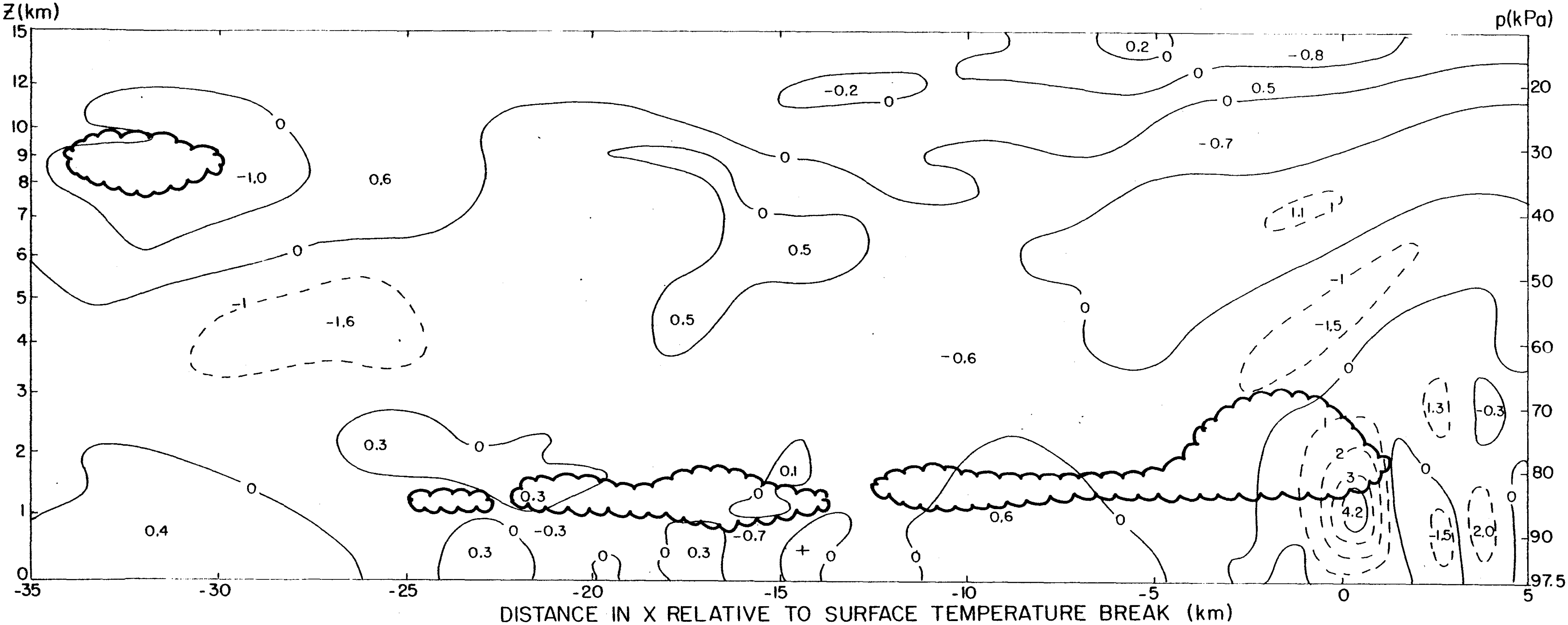

Figure 4.7. (b) As in (a) but for the side plane at 107.3 min.

cloudy areas (positive Q_c); areas of rain with radar reflectivity (based on Kessler's (1969) expression for the Marshall-Palmer raindrop distribution) greater than 50 dbz are covered in large dots, and from 30 dbz to 50 dbz covered in commas.

In the region of the TB we note:

(i) Strong updrafts, about 1 km above the ground, of 4.3 m s^{-1} on the central plane and 4.2 m s^{-1} on the side plane.

(ii) Cloud above and to the rear of these updrafts; this cloud is a permanent feature.

(iii) An updraft maximum of 1.2 m s^{-1} in the cloud, 3 km behind the TB on the central plane. This is the beginning of cell (5).

(iv) A downdraft above the TB of 1.2 m s^{-1} on the central plane and 1.5 m s^{-1} on the side plane, at a height of 4.5 km. Above that the sign of w continues to oscillate with generally decreasing amplitude. The phase lines slope down to the left and the temperature field (not shown) shows a similar structure, only shifted in phase so that the peak θ' is on the $w = 0$ line to the left of the peak downdraft. All this suggests that the structure is a gravity wave (lee wave) similar to that produced by air flowing over a mountain barrier - in this case the "barrier" is the pool of cold air. The gravity wave is a permanent feature of the simulation. It will be discussed in detail in Section 4.3.3 when we consider the averaged fields.

(v) Noise in the W field near the ground and ahead of the TB. This of rather large amplitude in W but not in the temperature field because the vertical potential temperature gradient is essentially zero here. The noise has no noticeable effect on the simulation.

Since there was no new cell development 15 min earlier we must move back a distance of 17 km on the central plane from new cell (5) to the old cell (4). This has a strong updraft of 14.0 m s^{-1} and a shaft of greater than 50 dbz rain beneath it. Cell (4) has grown so strongly that the cloud associated with it has grown up into forward-overhanging anvil cloud from cells (2) and (3a), leaving a strange-looking hole in the cloud mass. Cell (3) has an updraft of 8.1 m s^{-1}; in the last 5 min it has not moved very far left (see Fig. 4.6) as it has come under the influence of the circulation of (4). In fact, note that cells (3) and (4) are well merged in both cloud and rain. The cloud and rain mass also merges into the updraft area on the far left, which contains cell (2) at 8.1 m s^{-1} and cell (3a) (which broke away from (3) 20 min previously) at 6.8 m s^{-1}.

Within the leftmost area of rain there is a downdraft of 1.7 m s^{-1}, with a sloping updraft to its right. The rightmost area of rain has not been falling long enough to produce a very large or strong downdraft region.

Note the oscillations in the W field to the right of cell (4). These are more gravity waves and occur near all of the cells. They will be discussed in detail when we look at the temperature fields for 136.8 min.

On the side plane there is little happening at this time away from the TB. There is some shallow cloud near the surface which is to a large extent in downward motion regions and so currently evaporating. There is also a small amount of cloud aloft near -33 km. This has been "thrown out" by strong outflow from the top of cell (3a). Similarly, some rain has been advected from the central plane to both side planes but not enough to produce more than 30 dbz radar reflectivity.

At 122.1 min (Fig. 4.8) the vertical velocity field above the TB is much the same. But cell (5) has moved back to -12 km, far enough to allow the new development of cell (6) just behind the TB with an updraft of 2.0 m s^{-1}. Cell (5) now has an updraft of 5.0 m s^{-1} and already has a shaft of $>$30 dbz rain. This rain first appeared at a height of 2 km, in contrast to the height of over 6 km of new radar echoes on 14 May (SE). Note the tilt of cell (5) due to its growing in a vertical wind shear.

Farther back, at -30 km, cell (3) with an 8.1 m s^{-1} updraft clearly dominates the weak 1.1 m s^{-1} in the anvil which is all that remains of cell (4). (Below (4) is a small patch of $>$30 dbz rain from the previously strong updraft.) A new updraft maximum of 2.6 m s^{-1} called cell (4a) since it is about the same distance back from the TB as (4), has developed in the sloping updraft into the conglomerate of cells (3) and (4). In the extensive rain area to the left there is a peak downdraft

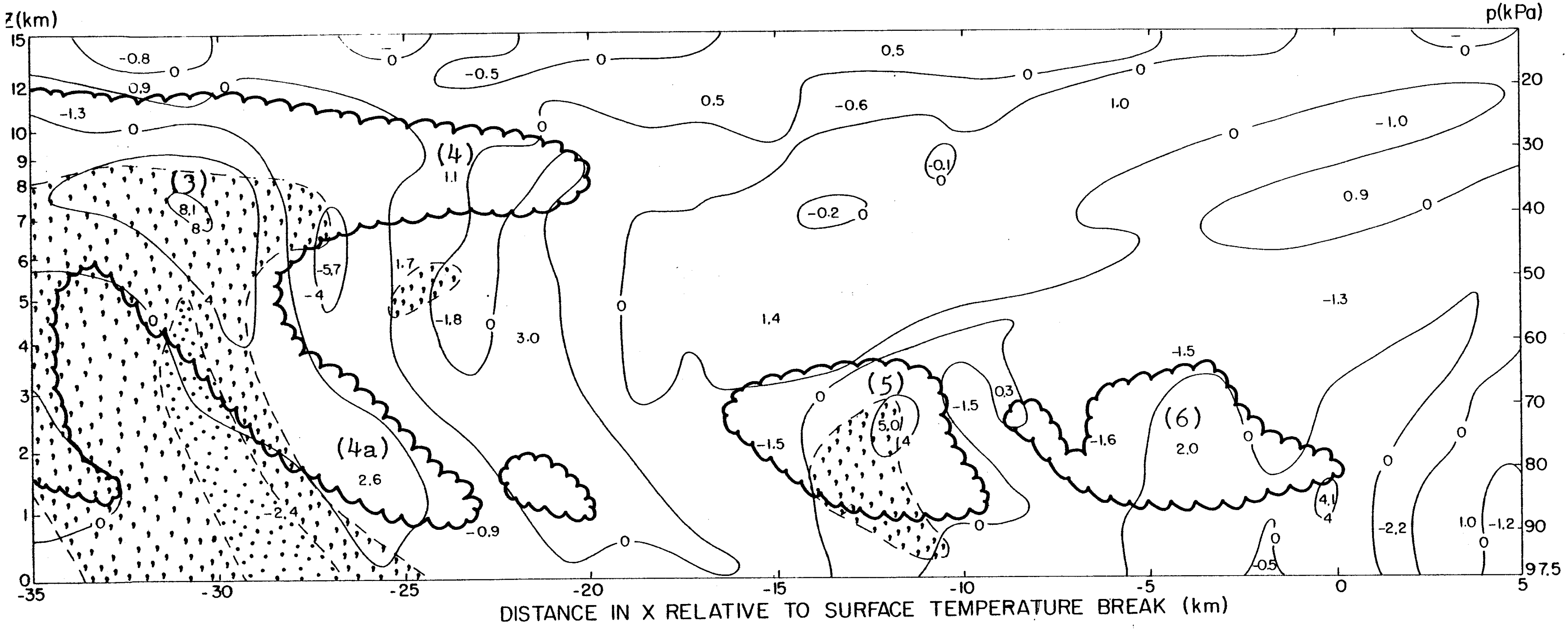

Figure 4.8. (a) Cloud, rain, and vertical velocity fields on the central plane at 122.1 min. Contouring conventions and units as in Fig. 4.7 (a).

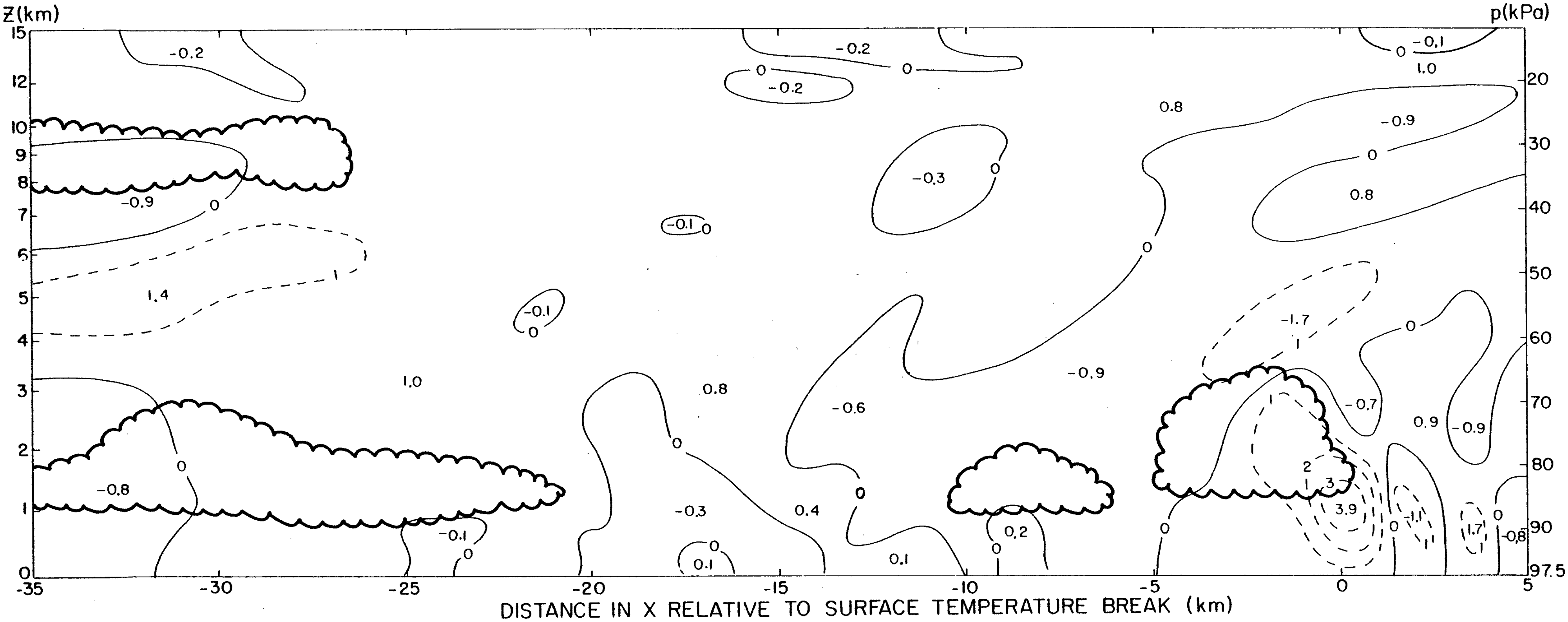

Figure 4.8. (b) As in (a) but for the side plane at 122.1 min.

of -2.4 m s^{-1}. A portion of the cloud associated with cell (2) is visible on the far left - this cell now has an updraft of only 2.3 m s^{-1} at -42 km and is becoming absorbed into the general anvil debris trailing off to the rear.

On the side plane at 122.1 min (Fig. 4.8 (b)) there is more low-based layer cloud than for the previous time - this resulted from downdraft air from all the rain on the central plane spreading out and forcing up air on the side plane. At higher levels, there is more cloud that has been thrown out from the convection on the central plane.

By 136.8 min (Fig. 4.9) the updrafts over the TB on both planes have increased by about 1.3 m s^{-1} over their previous values at 122.1 min. This increase is due to enhanced convergence at the TB as a result of the arrival of forward-spreading cold air produced by the rainfall from cells (2), (3), and (4); the significance of this will be shown in Section 4.3.3.2.

Just behind the TB on the side plane, cell (7) is now developing and has an updraft of 1.5 m s^{-1}.

On the central plane, cell (6) has reached an updraft of 4.8 m s^{-1} and is already raining out. Comparison with Fig. 4.8 (a) shows (6) to be in a very similar stage of development to (5) 15 min earlier. There is a difference in that (6) has an associated small cloud on the side plane.

Cell (5) has reached its peak updraft and is producing some heavy rain, though of less horizontal extent than the previous conglomerate of cells (2), (3), and (4). A separate

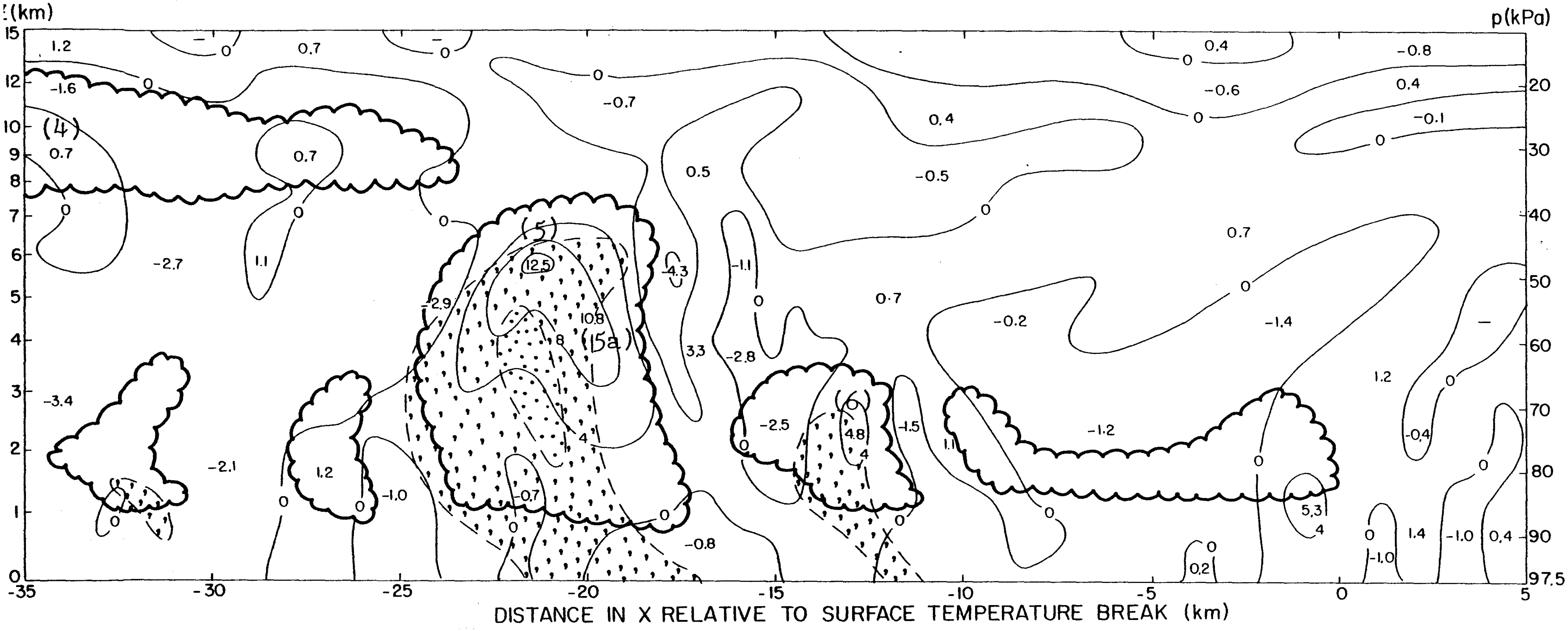

Figure 4.9. (a) Cloud, rain, and vertical velocity fields on the central plane at 136.8 min. Contouring conventions and units as in Fig. 4.7 (a).

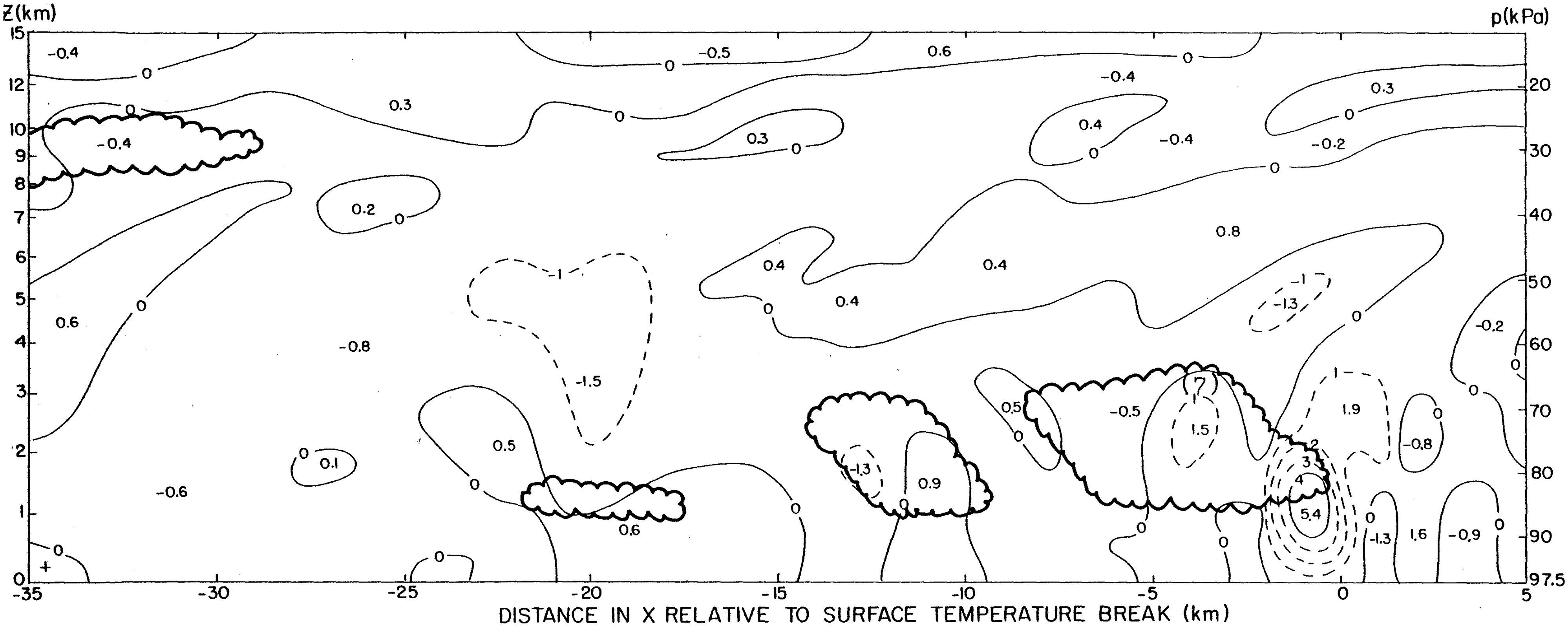

Figure 4.9. (b) As in (a) but for the side plane at 136.8 min.

updraft maximum of 10.8 m s^{-1}, cell (5a), has developed below and to the right, but will not last long. Note that the heaviest rain is almost aligned with a minimum of vertical velocity which extends between the two maxima, suggesting that in this case the rain caused a split to appear within the previously single updraft maximum. The cloud associated with (5) tilts to the left below 4 km and to the right above, in response to the change in sign of the wind shear (Fig. 4.14).

At -32 km on the central plane there is a small cloud with some residual rain. This is all that remains of cell (4a) which had previously developed in the sloping updraft region into cells (3) and (4). It was apparently cut off from the main cloud system by rain falling to its left. High above it, at a height of 9 km, is the remaining small updraft of cell (4), embedded in the forward-overhanging anvil of cell (3).

For this time of 136.8 min we also have the region from -35 km to -75 km depicted (Fig. 4.10). On the central plane the updraft of 5.1 m s^{-1} is denoted as cell (3c); it subsequently dies while the updraft of 2.1 m s^{-1} to its left persists and is tracked as (3). Falling from these is a broad area of rain with a peak downdraft within it of 1.6 m s^{-1}. (Paradoxically the strongest downdraft of 3.4 m s^{-1} is to the right of the heaviest rain, at about -34 km on Fig. 4.9 (a).)

All that remains of cell (2) is a 0.7 m s^{-1} updraft at -45 km. Farther back is an extensive area of cloud debris, on both planes, with generally weak upward motion. There is some

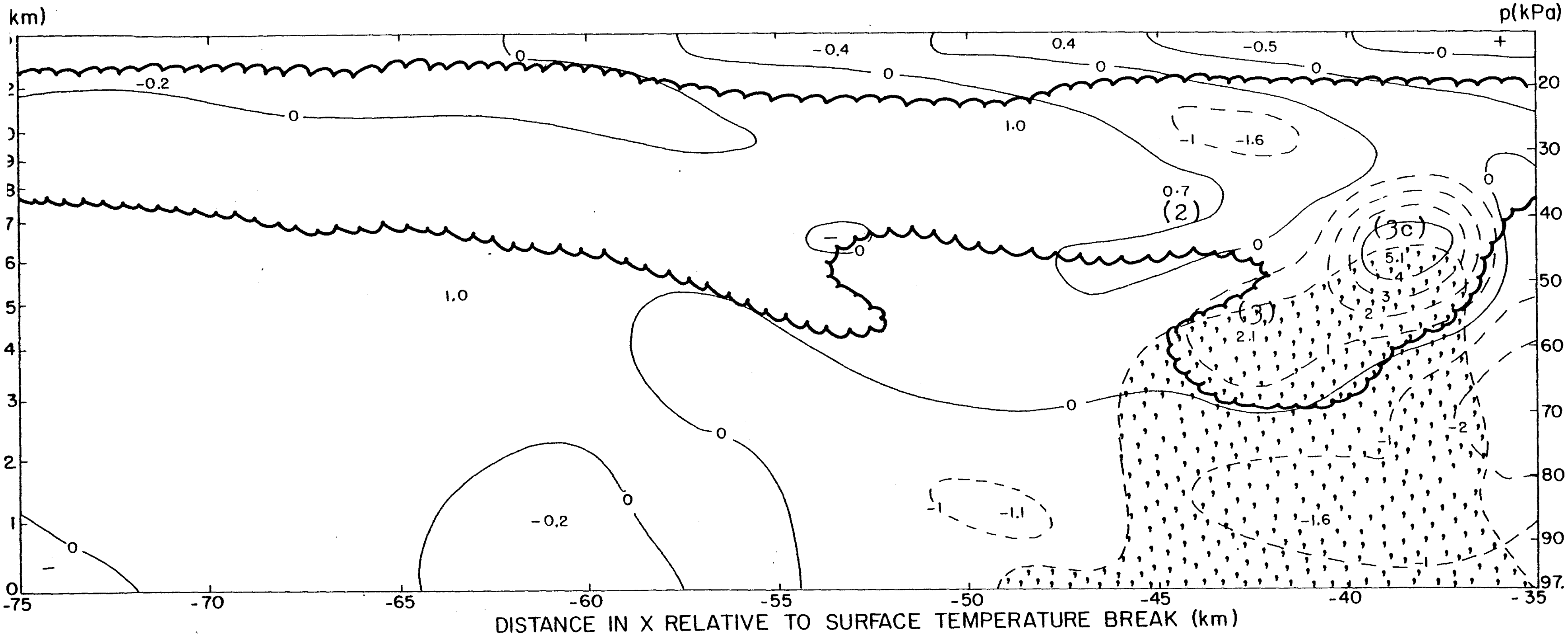

Figure 4.10. (a) Central plane fields at 136.8 min as in Fig. 4.9 (a) but for 35 km to 75 km behind the TB.

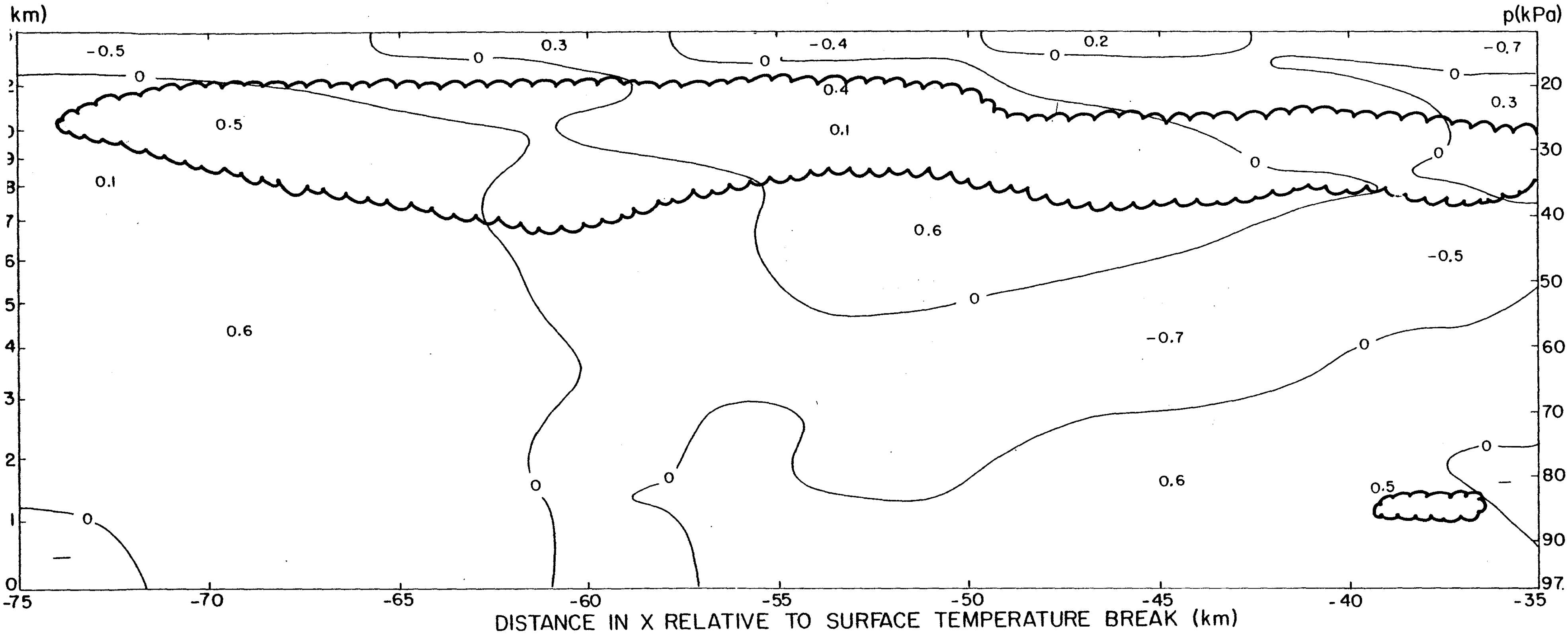

Figure 4.10. (b) Side plane fields at 136.8 min as in Fig. 4.9 (b) but for 35 km to 75 km farther behind the TB.

rain falling from this, but with less than 30 dbz radar reflectivity.

At 150.6 min (Fig. 4.11) we would expect the next cell to be developing. There is a very small cloud on the central plane at -7 km with an updraft of 0.4 m s^{-1}, but it will never develop further. Significantly, the downdraft aloft over the TB is stronger than it has been previously. This downdraft region slopes down towards the small cloud and must have a detrimental effect on its development.

On the side plane, cell (7) now has an updraft of 2.4 m s^{-1} (only half as strong as cell (6) in this position) and has produced only a small amount of rain. The central plane cell (6) has strengthened to a 7.2 m s^{-1} updraft, but is nowhere near as strong as cell (5) was in this position. The cell (5) updraft has decreased a little to 10.6 m s^{-1}. Almost the entire lower half of the cloud has been washed out by rain, thus cutting the cell off from the supply of high θ_e air.

For the final time shown of 165.4 min (Fig. 4.12) we see that the downdraft over the TB has decreased again, from -1.8 m s^{-1} on the central plane 15 min ago to -1.0 m s^{-1} now. Cell (8), with a 1.5 m s^{-1} updraft now, can therefore develop and will grow to reach a peak updraft of 13.2 m s^{-1}, 35 min later.

On the side plane, cell (7) now has an updraft of only 1.5 m s^{-1} and will soon die. There is a lot of noisy structure near it. The central plane cell (6), with a 7.7 m s^{-1} updraft,

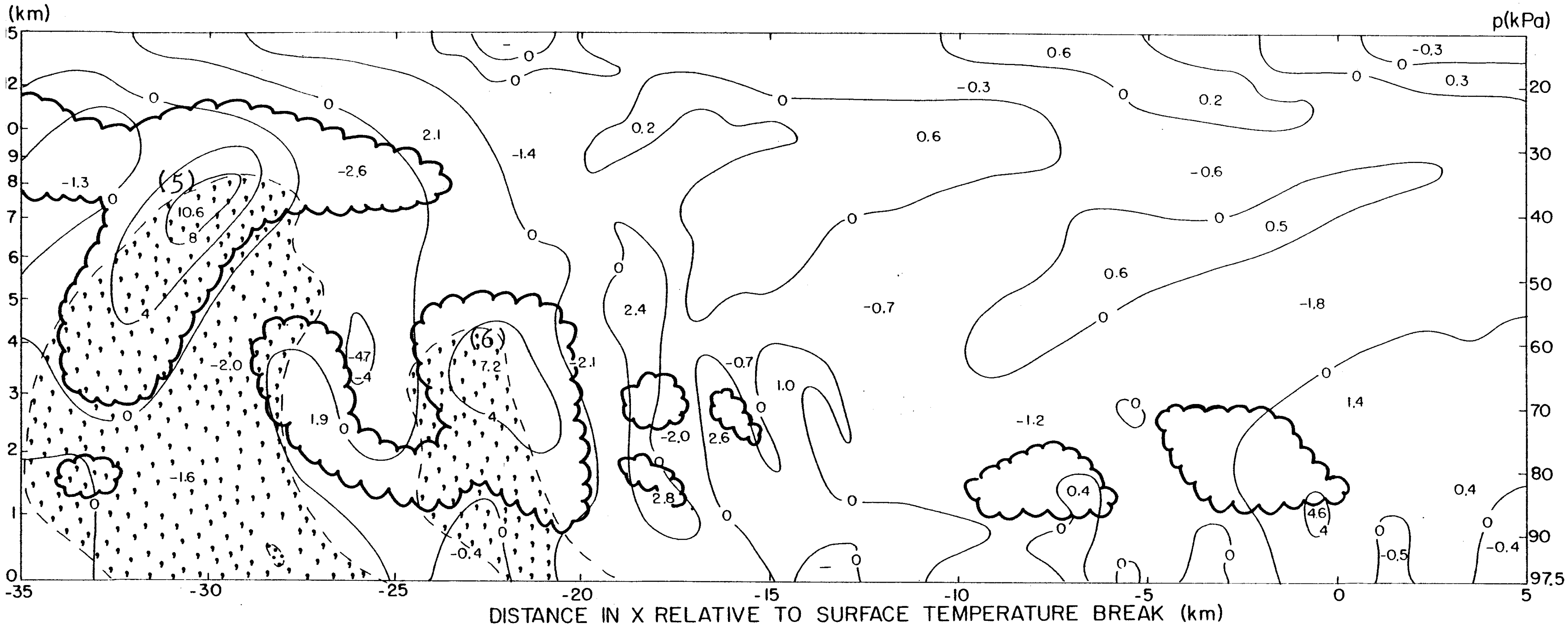

Figure 4.11. (a) Cloud, rain, and vertical velocity fields on the central plane at 150.6 min. Contouring conventions and units as in Fig. 4.7 (a).

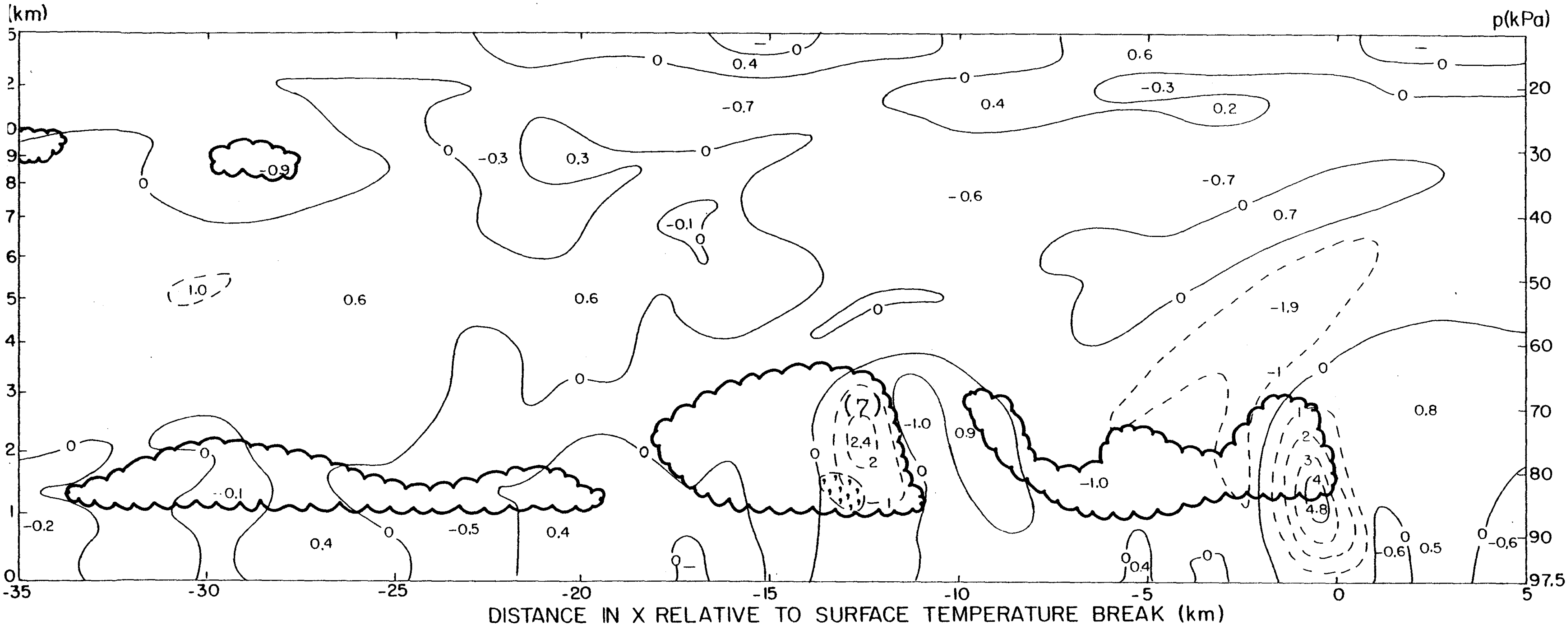

Figure 4.11. (b) As in (a) but for the side plane at 150.6 min.

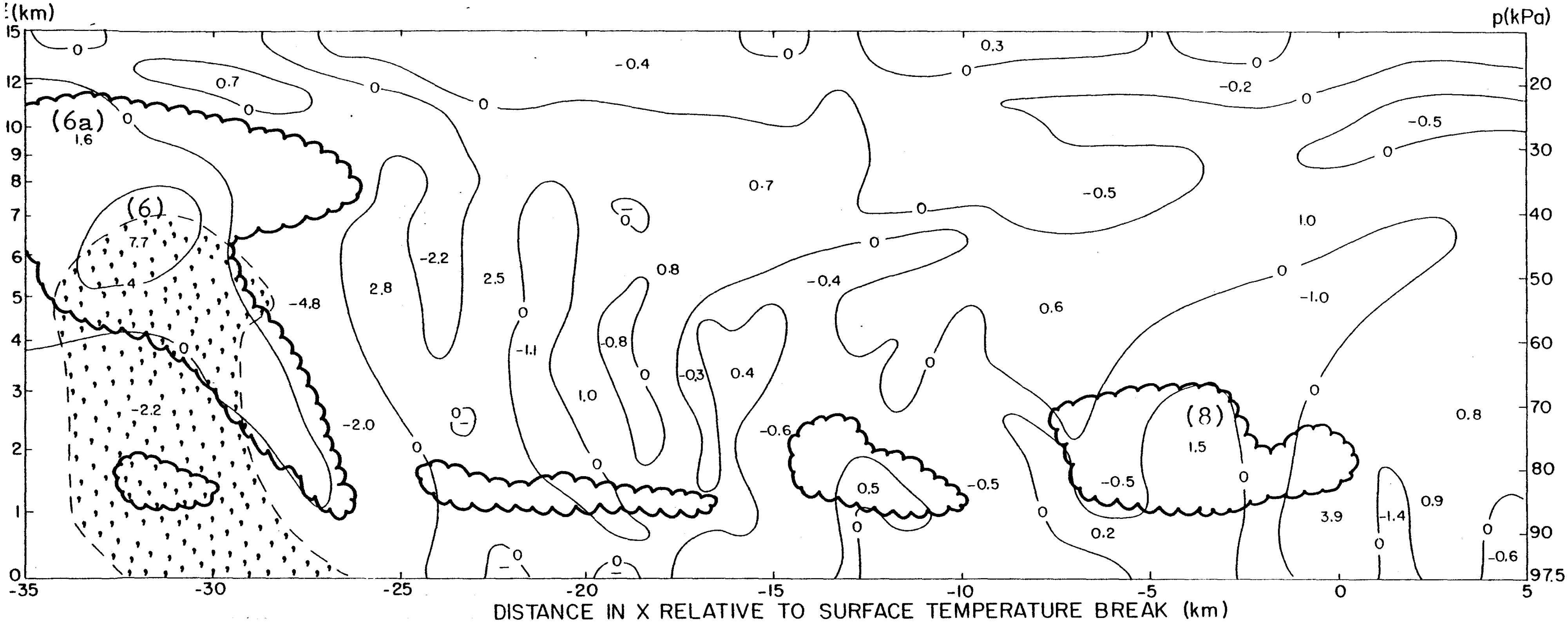

Figure 4.12. (a) Cloud, rain, and vertical velocity fields on the central plane at 165.4 min. Contouring conventions and units as in Fig. 4.7 (a).

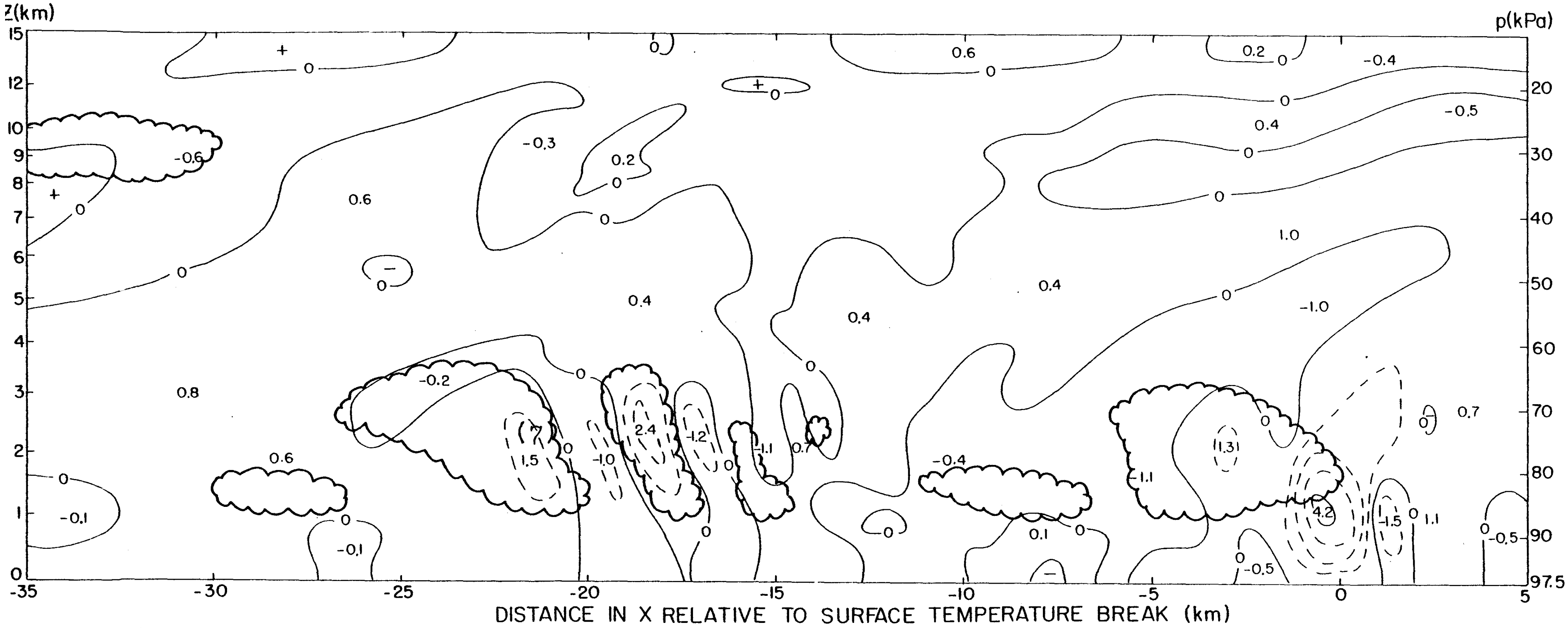

Figure 4.12. (b) As in (a) but for the side plane at 165.4 min.

is now past peak development. (Cell (6a) has split off to its left with a weak updraft of 1.6 m s^{-1}.) Rain has washed out much of the cloud in the lower half of (6), leaving a sloping updraft to the right. Gravity waves and noise cover the region to the left of about -10 km.

This series of figures of cloud, rain, and vertical velocity fields, together with Fig. 4.6 showing the cell tracks, has revealed major differences between the simulated cells and those on 14 May:

(1) The simulated cells moved back at twice the speed, were spaced twice as closely, and hence new ones developed at four times the frequency.

(2) The simulated new radar echoes first appeared at a height of about 2 km rather than over 6 km on 14 May, and subsequently reached no more than 55 dbz compared to over 65 dbz on 14 May. Simulated echo top heights (if defined by 30 dbz) reached only 9 km while the observed were 11 or 12 km.

(3) Typical strongest simulated updrafts were 15 m s^{-1} at a height of about 7.5 km. The strongest observed updraft on 14 May (estimated from balloon ascent rates) was 16.2 m s^{-1}, but that was at a relatively low height of 4 km, suggesting that peak updrafts could have been 20 or 25 m s^{-1}.

The faster movement of the simulated cells can likely be attributed to their being rooted in air that was moving faster than that for the observed cells (see the averaged u field in

Fig. 4.20). The disparity in initial echo heights will be discussed shortly. All the other differences indicate that the simulated cells were smaller and weaker than the observed ones. Possible contributing causes of this weakness were the slight stabilizing of the inflow air as it approached the system (see Section 4.3.2.2) and the omission of the ice phase and its associated additional latent heat release. The main cause is thought to be the crude three-dimensionality of the model. Recall from Chapter 3 that a change in the model from two-dimensional geometry to the quasi-three-dimensionality used here did allow a simulated cumulus cloud to develop more strongly, but it was still significantly weaker than for a fully three-dimensional model. Had better resolution been used in the third dimension (y) then the cells should have been stronger, larger, and spaced farther apart.

Further evidence of the stronger updrafts on 14 May is given by the level of the initial radar echo; this was unusually high for ordinary cumulonimbi (e.g., Battan, 1963) but not for severe storms with very strong updrafts (e.g., Browning and Atlas, 1965) which can carry the cloud particles to high levels in the time they take to reach radar-detectable size. This calls into question the applicability to strong cumulonimbi of microphysical parameterization schemes like Kessler's (1969) or Manton and Cotton's (1977) which use fixed autoconversion thresholds and do not allow some time delay mechanism (as, for instance, in Cotton, 1972) for the cloud particles to grow to raindrop size. (Another problem is that on 14 May the initial echo appeared at a temperature level of -20°C, suggesting that ice processes may have played a part in its formation.) Fortunately, the inability of our model to produce strong updrafts in the first place means that the cloud particles did have time to grow at low levels and the assumption of a fixed autoconversion threshold was perfectly reasonable.

4.3.2.2 Other Fields at 136.8 Minutes

We now return to the time of 136.8 min, in the middle of the period under consideration, and examine some of the other model fields. Firstly, Fig. 4.13 shows the v velocity component halfway between the side and central planes, with positive values directed towards the central plane. Away from the convective cells the magnitude of v is generally small, but there are strong inflow/outflow doublets in association with the updrafts of cells (5) and (6) at -22 km and -13 km. (See Fig. 4.9.) Even our crude three-dimensional representation allows a strong circulation to develop in the third dimension.

At the left of the figure there is a 3.2 m s^{-1} flow towards the central plane; this feeds into the anvil updraft of cell (4) and a downdraft below. Near the surface the flow is generally outwards from the central to side planes: this is the colder central plane air spreading out (see Fig. 4.15).

To illustrate further the three-dimensional character of

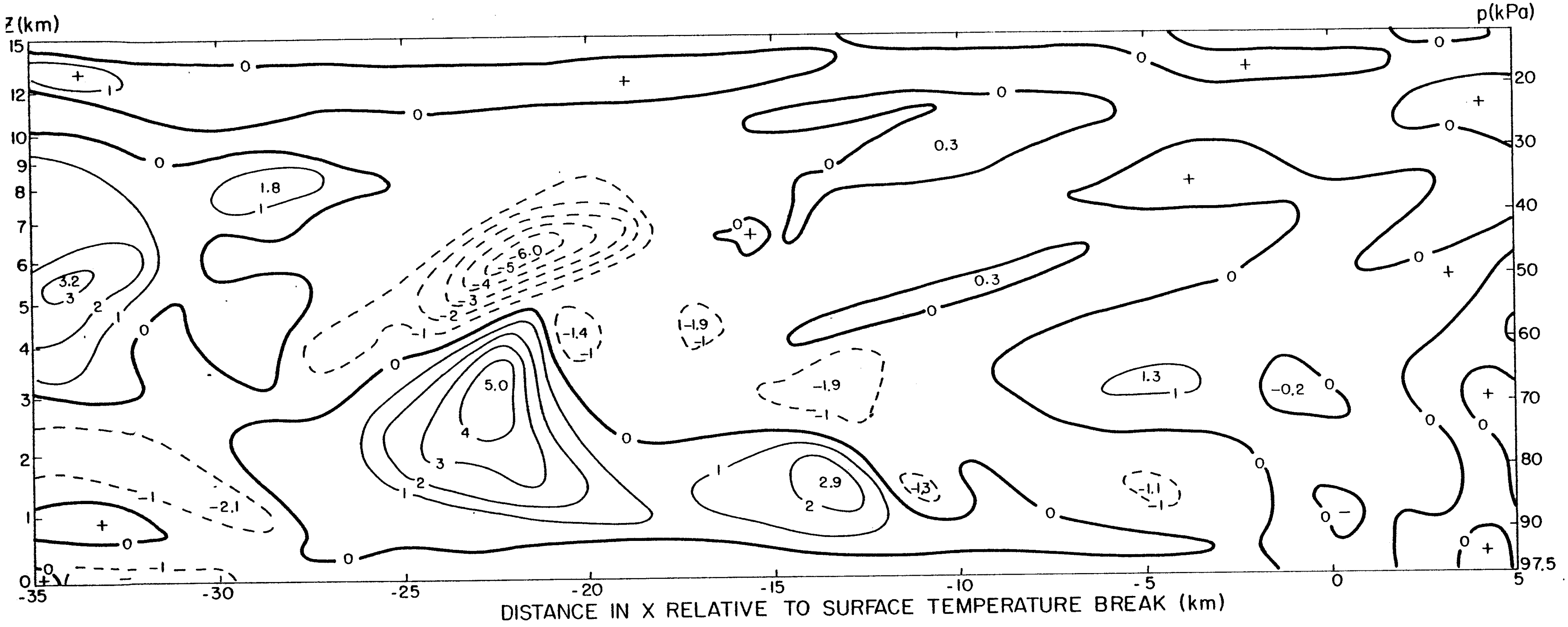

Figure 4.13. The v velocity component at 136.8 min. The v field is located halfway between the central and side planes with positive values directed towards the central plane. Units are in m s^{-1} with negative isotachs dashed.

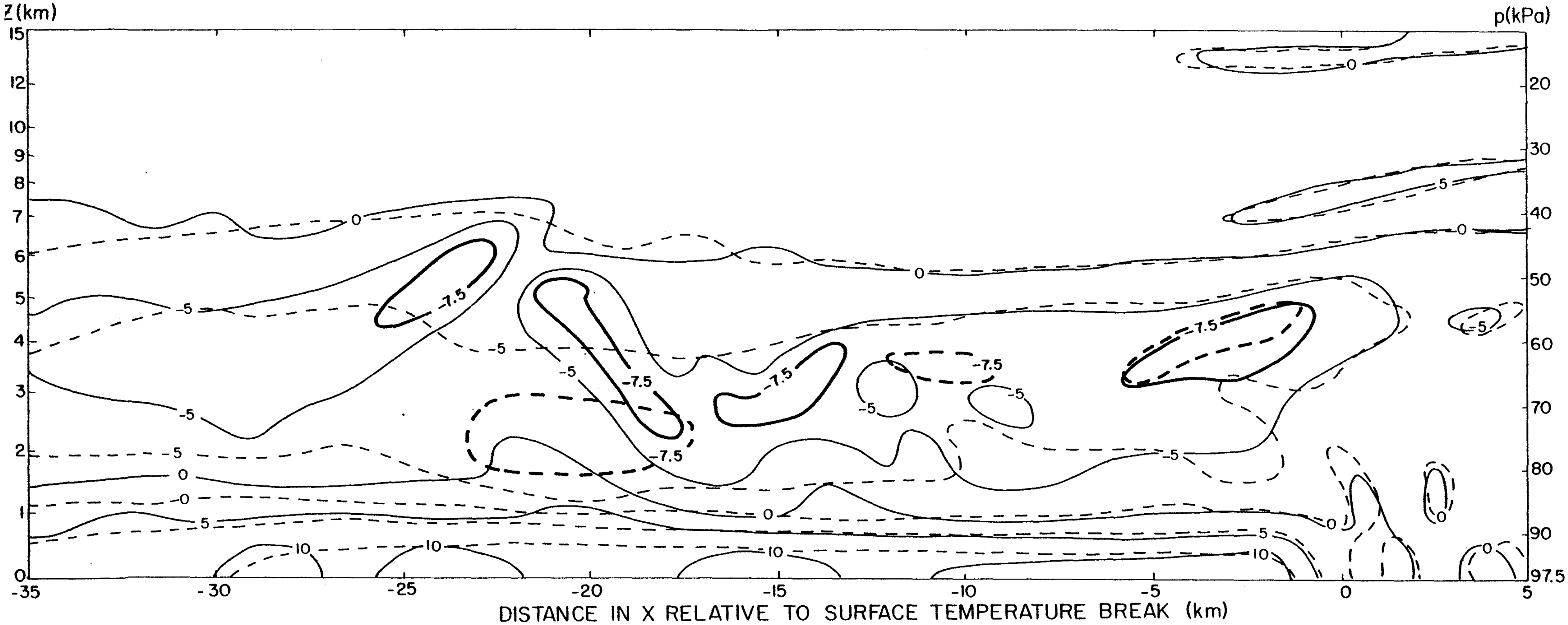

Figure 4.14. The u velocity components (relative to the ground) on both planes at 136.8 min. Central plane values are solid and side plane dashed. Units are m s^{-1} with contours at 5 m s^{-1} intervals, except that the -7.5 m s^{-1} isotachs are included as heavy lines.

the cells and system Fig. 4.14 shows the u velocity components (relative to the ground) for both central (solid) and side (dashed) planes. In order to visualize relative inflow and outflow patterns it is helpful to know that the cells are moving at about -3 m s^{-1} relative to the ground.

The right-hand edge of cell (5) is at -18 km, so the central plane u field indicates relative inflow between the heights of 1.5 km and 5 km, with a tongue of high negative values extending up into the cloud. Above 5 km there is outflow into the gravity wave region associated with the cloud (see the schematic streamlines in Fig. 4.16). On the left-hand edge at -24 km there is inflow below 2.5 km with strong outflow above it.

However, cell (6) has inflow on its right-hand edge at -12 km everywhere above 1.5 km. It is entraining air on its upshear side and detraining on the downshear side, just like the clouds growing in shear that were studied by Malkus (1952).

Now look at -20 km and a height of about 1.7 km; here u is zero on the central plane (due to the effects of the cloud) but -7.5 m s^{-1} on the side plane. Clearly the "environmental" air of the side plane is flowing past the cell and not being blocked by it as would occur in a two-dimensional model. Of course it isn't _just_ flowing past - it is also feeding into the lower part of cell (6). Aloft we have the opposite situation where the central plane air flowing out rearwards from the cell is moving faster than the side plane air.

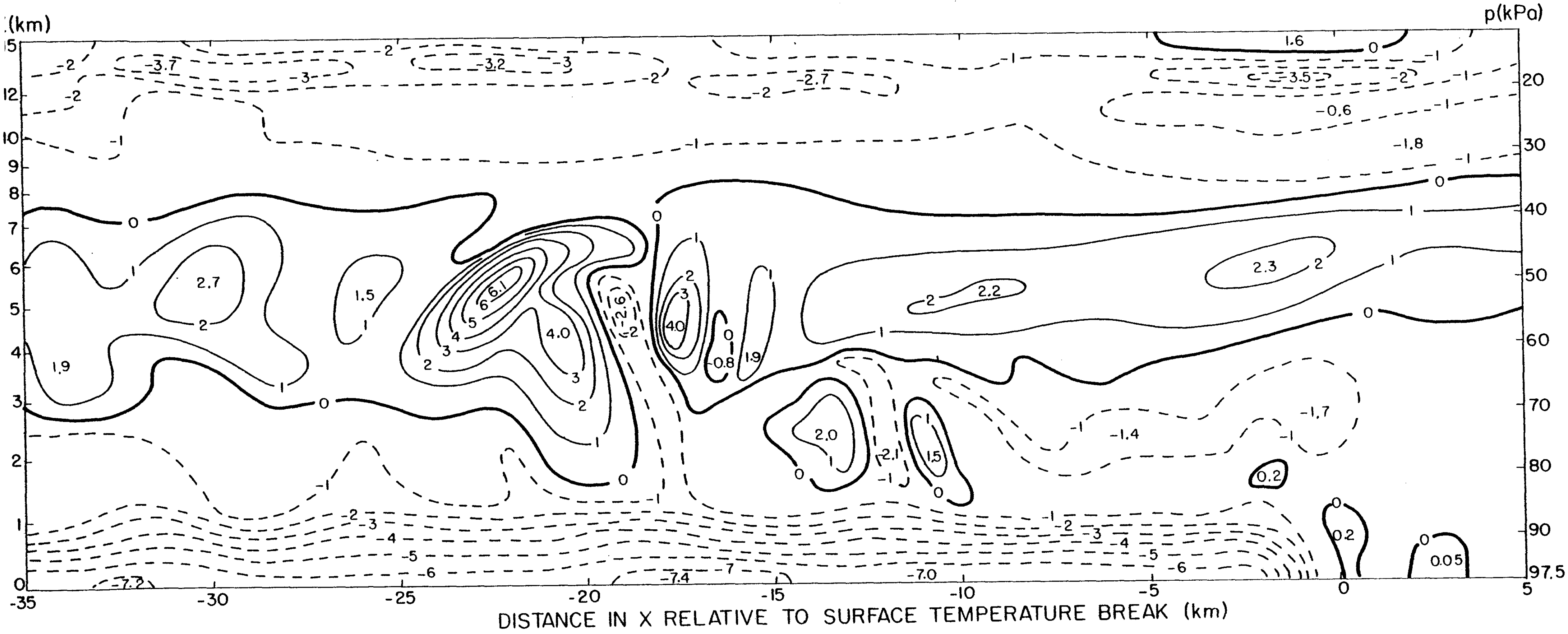

Figure 4.15. (a) The field of potential temperature perturbation (θ') on the central plane at 136.8 min. Units are degrees kelvin with contours at 1 K intervals, negative isotherms dashed.

Away from the convective cells the fields from the two planes match well, indicating quasi-two-dimensionality. There is a very strong surface convergence zone at the TB with a change in u of 10 m s^{-1} over only 3 km.

The temperature perturbation fields for the central and side planes are given in Fig. 4.15. On both planes the surface pool of cold air is obvious, with a strong temperature gradient behind the TB.[1]

The strongest gradient and coldest temperatures are on the central plane as a consequence of most of the rain and associated evaporative cooling occurring there.

Although the air flowing in from the right-hand edge of the domain (40 km ahead of the TB) is given base-state profiles of temperature and moisture by the boundary conditions, it has already been quite strongly modified by the time it reaches +5 km. The modification has the same vertical structure as the gravity waves over the TB so the effect of these must extend upstream (through pressure gradients) and produce mean rising and sinking motions. Although the vertical velocities to the right of +5 km are no more than 0.4 m s^{-1} in magnitude they act over a long distance to produce the modifications. The modified profiles persist through the system apart from modulations due to the gravity waves and convection.

---

[1] In drawing all the figures in this section the movement of the TB was taken to be 8.0 m s^{-1} from its initial position at 107.3 min. It actually moved a little slower so the TB in the temperature field appears at about -1 km for this time.

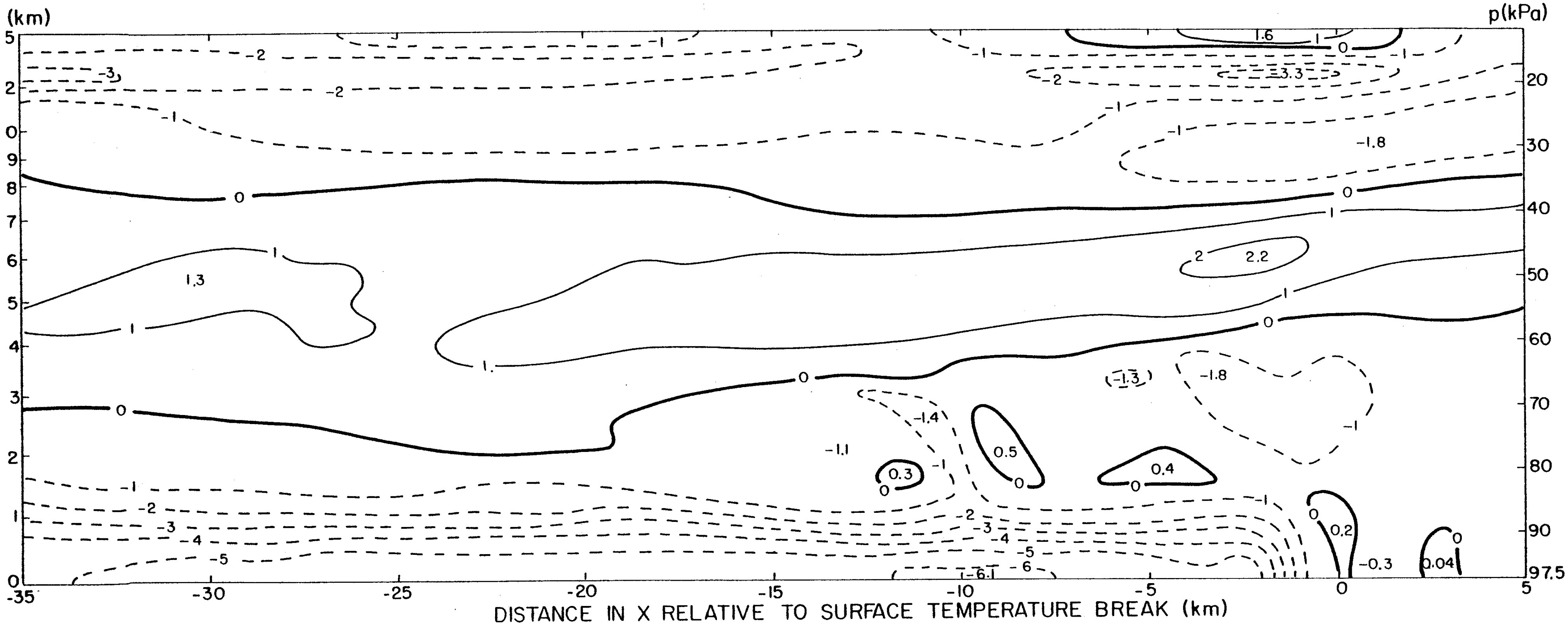

Figure 4.15. (b) As in (a) but on the side plane at 136.8 min.

There are only small positive temperature perturbations associated with the permanent cloud over the TB - the air moves through its associated updraft too quickly ($\sim 8 \text{ m s}^{-1}$) for any substantial net vertical displacement and consequent latent heat release.

Cell (6) on the central plane at -13 km is associated with a +2.0 K perturbation. To its right is some cold air produced by mixing and evaporative cooling of the air entraining at the cloud edge. The warm air to the right of that has apparently been produced by subsidence between cell (6) and another small cloud tower. (A tongue of lower θ_e air extends down between them in Fig. 4.17.)

To the right of cell (5) at about -20 km is an oscillatory structure which is roughly 90° out of phase with the vertical velocity field (see Fig. 4.9 (a)), indicating that it is a gravity wave[1] feature with air flowing through it from left to right. To show what appears to be happening, Fig. 4.16 is a schematic diagram of streamlines in the central x-z plane relative to cell (5), based on the actual fields of u and w at 136.8 min. The air which participates most strongly in the gravity wave rises near the right-hand edge of the cloud, exits to the right and sinks due to a combination of pressure forces (which drive the compensating subsidence) and strong evapora-

---

[1] A this point Δx is about 700 m so the wave has a wavelength of $3\Delta x$, marginally resolved by the model. Hence, although the physical explanation given for it is plausible, the wave should not be considered to be quantitatively exact.

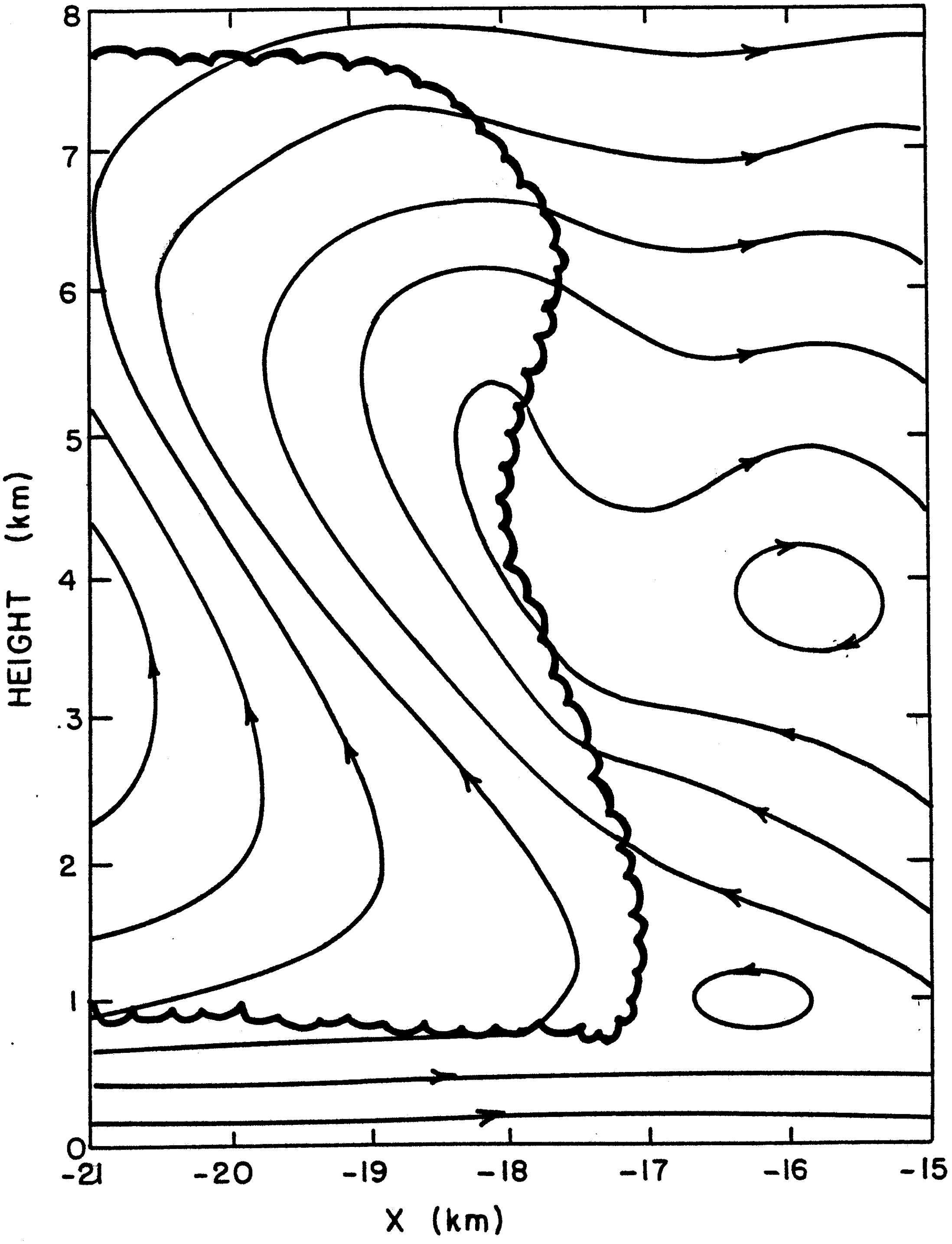

Figure 4.16. Schematic streamlines of flow in the central x-z plane relative to cell (5) at 136.8 min. The cloud outline is scalloped.

tive cooling because of mixing at the cloud edge. (Note the -2.6 K and associated cold tongue along the cloud edge in Fig. 4.15 (a).) But the air overshoots and warms up, then continues to oscillate vertically with decreasing amplitude as it moves away from the cloud. So the gravity wave is due to air exiting from the cloud being perturbed, rather than to an upward push on a stable layer radiating waves as if from a stone thrown in a pond.

Associated with cell updrafts (5) and (5a) are the peak warm perturbations of +6.1 K and +4.0 K. For comparison, the temperature perturbation for moist adiabatic ascent to 5.5 km would be about +7 K so the air ascending within the cloud has been only slightly diluted. The orientation of the warmest area, sloping down from right to left, reflects air having reached its highest vertical displacement, hence most latent heat release, before coming into contact with the air around the top and left-hand edge of the cloud which is much cooler due to a combination of forced dry adiabatic ascent (at the top of the cloud only) and evaporative cooling as the cloud mixes into the dry environment. Both temperature maxima are displaced a little (one grid-point) to the left of the updraft maxima.

There are also rather large temperature perturbations near the top of the model, in association with gravity waves of weak amplitude in vertical velocity in the very stable air up there.

Figure 4.17 gives the field of equivalent potential tem-

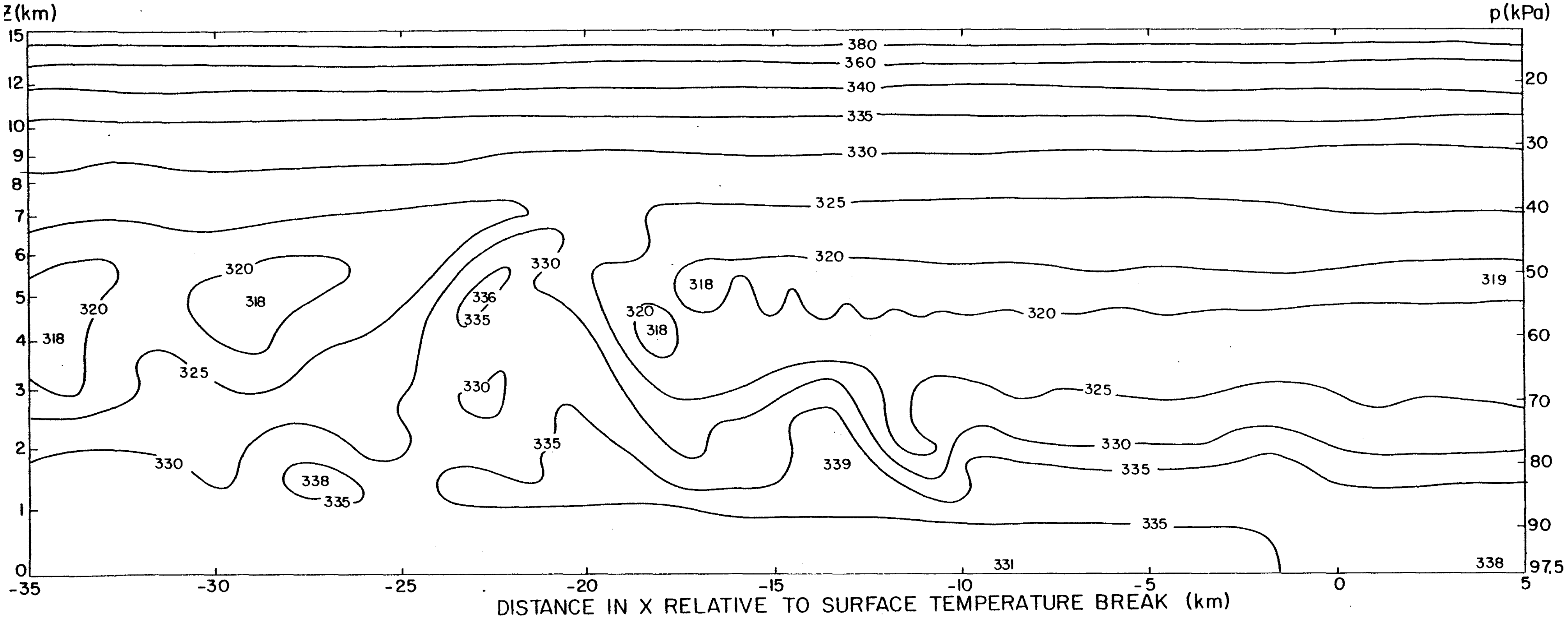

Figure 4.17. The field of equivalent potential temperature (θ_e) on the central plane at 136.8 min. Units are degrees kelvin with contours at 5 K intervals except above 340 K where they are at 20 K intervals.

perature (θ_e) on the central plane. Because of the very stable air aloft the contours are spaced at intervals of 20 K above 340 K rather than 5 K below. Coincidentally, the 320 K isotherm is located in a position to show the damped gravity wave oscillations to the right of cell (5). The air feeding up into cell (5) around -20 km and cell (6) at -13 km is shown clearly. As already noted, smaller values of θ_e have been brought down by the downdraft to the right of cell (6).

The 336 K maximum in cell (5) at -23 km and a height of 5 km is again indicative of the almost undiluted ascent of air in the updraft core, since the cloud-base air (above the cold pool) also has θ_e of about 336 K.

The vertical structure of θ_e feeding in from the right, with a minimum at around 50 kPa, is considerably disturbed by the convection, while farther to the left air which has not actively participated in the convection retains the θ_e minimum. Consequently, the "processed" air leaving the mesoscale system at the rear will still be conditionally unstable, though less than when it entered.

In spite of the base-state profile of θ_e having a maximum surface value of 338 K and minimum value of 319 K, the field for this time has a maximum of 339 K at -13 km and several minima of 318 K. The explanation is that just as the advective scheme can produce negative water by advecting it out of a grid box which had none, so it can produce spuriously larger or smaller values than previously existed. However, these spurious differences are small enough to be tolerable.

The final field we will consider for 136.8 min is the pressure perturbation field (p') averaged over the central and side planes (Fig. 4.18). There is a pressure jump at the TB, with an increase of 25 Pa (0.25 mb) over a distance of a kilometre, which would take about two minutes to occur at a fixed point on the ground as the TB passed. The excess pressure near the ground is due to the pool of cold air, with the nearly horizontal isobars indicating that the pressure field is nearly hydrostatic. Similarly, the pressure structure above 50 kPa seems mostly hydrostatic and due to the deviation of the temperature field from the base-state.

The switchover in sign of the horizontal pressure gradient at 90 kPa at the TB corresponds well with SE's estimated geopotential profiles through the 14 May system. The doublet of -70 Pa and +45 Pa at -21 km is related to cell (5), producing the well-known retarding pressure force on the cell itself and compensating subsidence in the environment. The broad feature of a trough in the neighbourhood of -20 km and a generally rearwards pressure gradient force in the 90 to 50 kPa layer ahead of that persists throughout the run, and again corresponds to SE's results.

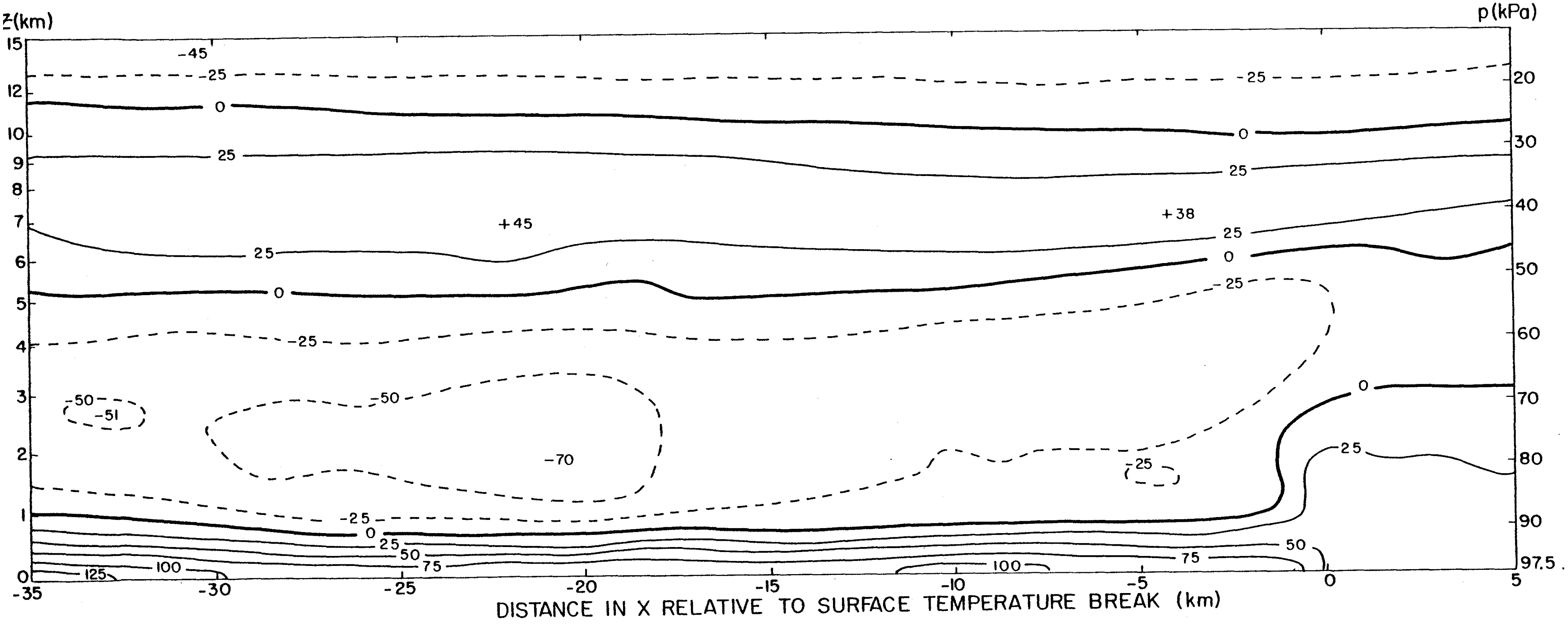

Figure 4.18. The field of pressure perturbation (p') averaged over the domain in y at 136.8 min. Units are Pascals, with contour intervals of 25 Pa (0.25 mb) and negative isobars dashed.

4.3.3 Space- and Time-Averaged Fields over 107.3 to 165.4 Minutes

Having seen the behaviour of the convective system at a number of points in time we will now examine model fields averaged in time and space so that the fluctuations due to cumulus and other small-scale phenomena have been smoothed out, leaving essentially the mesoscale fields. We can then compute (among other things) flux divergences due to deviations from the averaged fields, thus determining the effects of the smaller scales on the mesoscale.

The methodology of computing the averages and other derived fields (sources) is given in Section 4.3.3.1, together with the terminology used to describe them. The averaged fields of u and w are presented and discussed in Section 4.3.3.2. Then the averaged field of θ and source fields for that and other quantities are given in Section 4.3.3.3.

4.3.3.1 Methodology and Terminology

Consider a quantity, Q, governed by the equation

$$\dot{Q} + D_Q = \frac{\partial Q}{\partial t} + \frac{\partial}{\partial x}(uQ) + \frac{\partial}{\partial y}(vQ) + \frac{1}{\bar{\rho}}\frac{\partial}{\partial z}(\bar{\rho} w Q) \quad (4.1)$$

where $\dot{Q} + D_Q$ is the rate of change of Q following the resolvable motion given by the velocity components (u, v, w). $\dot{Q}$ is the "real" rate of change due to such effects as latent heat release for potential temperature and pressure gradients for horizontal velocity. D_Q represents the effects of small, unresolvable scales and must be expressed as a parameterized subgrid diffusion.

Now define an average in y and in time over the period from $t = t_1$ to t_2 by

$$[Q](x,z) = \frac{1}{t_2 - t_1}\int_{t_1}^{t_2}\left(\frac{1}{\text{WIDTH}}\int_0^{\text{WIDTH}} Q(x,y,z,t)\,dy\right)dt \qquad (4.2)$$

Further, apply a filter in the x direction defined by:

$$\{[Q]\}(x,z) = \int_{-\infty}^{\infty} a_F(x')[Q](x+x',z)\,dx' \qquad (4.3)$$

where a_F is the function comprising the filter weights.

Suppose each quantity to be a sum of this filtered average[1] plus a deviation:

$$Q(x,y,z,t) = \{[Q]\}(x,z) + \tilde{Q}(x,y,z,t) \qquad (4.4)$$

where the tilde denotes the deviation.

Consider a nonlinear term of the form

$$\begin{aligned} uQ &= (\{[u]\} + \tilde{u})(\{[Q]\} + \tilde{Q}) \\ &= \{[u]\}\{[Q]\} + \tilde{u}\tilde{Q} + \tilde{u}\{[Q]\} + \{[u]\}\tilde{Q} \end{aligned}$$

---

[1] We will usually call the filtered, averaged fields simply the averaged fields.

Apply the averaging operator $[\ ]$, then the filtering operator $\{\ \}$, for

$$\begin{aligned}\{[uQ]\} &= \{[u]\}\{[Q]\} + \{[\tilde{u}\tilde{Q}]\} \\ &\quad + \{[\tilde{u}]\{[Q]\}\} + \{\{[u]\}[\tilde{Q}]\} \\ &\quad + \left(\{\{[u]\}\{[Q]\}\} - \{[u]\}\{[Q]\}\right)\end{aligned}$$

Since $\{[\tilde{u}]\}$ and $\{[\tilde{Q}]\}$ are both identically zero by definition, we would expect the third and fourth terms to be small, and could neglect them. The last term should also be small since it is the difference between a filtered and unfiltered product of two already filtered fields. In practice we will only compute $\{[uQ]\}$ and $\{[u]\}\{[Q]\}$, obtaining the sum of the last four terms as a residual and denoting the result as $\{[\tilde{u}\tilde{Q}]\}$, the flux component due to the resolvable deviations from the averaged fields.

Application of the averaging and filtering operators to the original equation (4.1) results in

$$\begin{aligned}\{[\dot{Q}]\} + \{[D_Q]\} = \{[\tfrac{\partial Q}{\partial t}]\} + \{\tfrac{\partial}{\partial x}([uQ])\} + \{[\tfrac{\partial}{\partial y}(vQ)]\} \\ + \frac{1}{\bar{\rho}}\frac{\partial}{\partial z}\left(\bar{\rho}\,\{[wQ]\}\right)\end{aligned}$$

It is easily shown that $[\frac{\partial}{\partial y}(vQ)] = 0$, and since the filtering operator $\{\ \}$ and partial derivative $\partial/\partial x$ are both linear operators in x, their order may be interchanged to give

$$\{[\dot{Q}]\} + \{[D_Q]\} = \{[\frac{\partial Q}{\partial t}]\} + \frac{\partial}{\partial x}(\{[uQ]\}) + \frac{1}{\bar{\rho}}\frac{\partial}{\partial z}(\bar{\rho}\{[wQ]\})$$

Substituting for the nonlinear terms we obtain

$$\dot{Q}^A = \dot{Q}^R + \dot{Q}^V + \dot{Q}^D$$

where

$$\dot{Q}^A = \{[\frac{\partial Q}{\partial t}]\} + \frac{\partial}{\partial x}(\{[u]\}\{[Q]\}) + \frac{1}{\bar{\rho}}\frac{\partial}{\partial z}(\bar{\rho}\{[w]\}\{[Q]\}) \qquad (4.5)$$

is the <u>apparent source</u> of Q following the averaged (mesoscale) motion,

$$\dot{Q}^R = \{[\dot{Q}]\} \qquad (4.6)$$

is the <u>real source</u> of Q (for example, latent heat release when Q is potential temperature),

$$\dot{Q}^V = -\frac{\partial}{\partial x}(\{[\tilde{u}\tilde{Q}]\}) - \frac{1}{\bar{\rho}}\frac{\partial}{\partial z}(\bar{\rho}\{[\tilde{w}\tilde{Q}]\}) \qquad (4.7)$$

is the <u>virtual source</u>[1] of Q due to resolvable deviations of u, w and Q from the averaged fields, and

$$\dot{Q}^D = \{[D_Q]\} \qquad (4.8)$$

is the <u>diffusive source</u> of Q due to parameterized subgrid-scale processes.

---

[1] This terminology corresponds to SP's except that their virtual source is the sum of our virtual and diffusive sources.

To compute the required averages it was first necessary to define a new grid that moved in x relative to the ground at a constant speed - that of the TB during the time period (8 m s^{-1}). This grid had the same spacings in y and z as the old grid but used a constant spacing in x of 400 m. For each of the thirteen times that the fields had been saved the new grid was located relative to the old one and fields linearly interpolated from the old to the new.

Using the fields defined on the new grid all the terms in the above equations were computed directly, except for two special cases. First, as noted already, the eddy flux divergence terms were computed as residuals, e.g.,

$$\frac{\partial}{\partial x}\left(\{[\tilde{u}\tilde{Q}]\}\right) = \frac{\partial}{\partial x}\left(\{[uQ]\}\right) - \frac{\partial}{\partial x}\left(\{[u]\}\{[Q]\}\right)$$

rather than computing all the deviations $\tilde{u}$ and $\tilde{Q}$. Second, D_Q, and hence $\dot{Q}^D$, was computed by diagnosing the field of K_H on the old grid, interpolating to the new grid, then using

$$D_Q = \frac{\partial}{\partial x}\left(K_H \frac{\partial Q}{\partial x}\right) + \frac{\partial}{\partial z}\left(K_H \frac{\partial Q'}{\partial z}\right) \qquad (4.9)$$

in the standard finite difference form. (Diffusion in y did not need to be calculated because averaging in y would have eliminated it.)

The integration in y was simply a matter of adding one-third of the central plane value to two-thirds of the side plane value. Trapezoidal integration was used in time.

Filtering was found to be necessary in x because of the noisiness of the raw averages - mostly due to the coarse resolution in time (5 min). The filter used was a symmetric Gaussian filter (Holloway, 1958) truncated after 18 terms (or 7.2 km) away from the centre. As shown in Fig. 4.19 the filter passed only 20% of the 8 km wavelength (approximately the spacing between consecutive cells), 50% of the 12 km wavelength, and over 95% of the 50 km wavelength (approximately the scale of the mesoscale updraft/downdraft doublet on 14 May).

4.3.3.2 Averaged Velocity Fields

Fig. 4.20 shows the field of $\{[u]\}$, relative to the movement of the TB, over the usual range in x of -35 km to +5 km. Note the very shallow positive region between the ground and about 92 kPa; everywhere else the air is moving to the left through the system. In comparison, SE's analysis for 14 May (Fig. 4.2) shows a slightly deeper layer to 88 kPa of forward motion[1] because the air had the benefit of synoptic-scale forcing from the rear. As a result of that and the strong vertical shear the cells on 14 May were apparently rooted in air that was moving back more slowly than in our simulation, and the cells themselves moved back more slowly.

Because of the horizontal filtering the leading edge of the forward motion in the field of $\{[u]\}$ is 2 km behind the TB.

---

[1] The top of the forward motion is defined by the isotach of $+6.7\ \mathrm{m\ s^{-1}}$, the speed of the SWS, since that u field is relative to the ground.

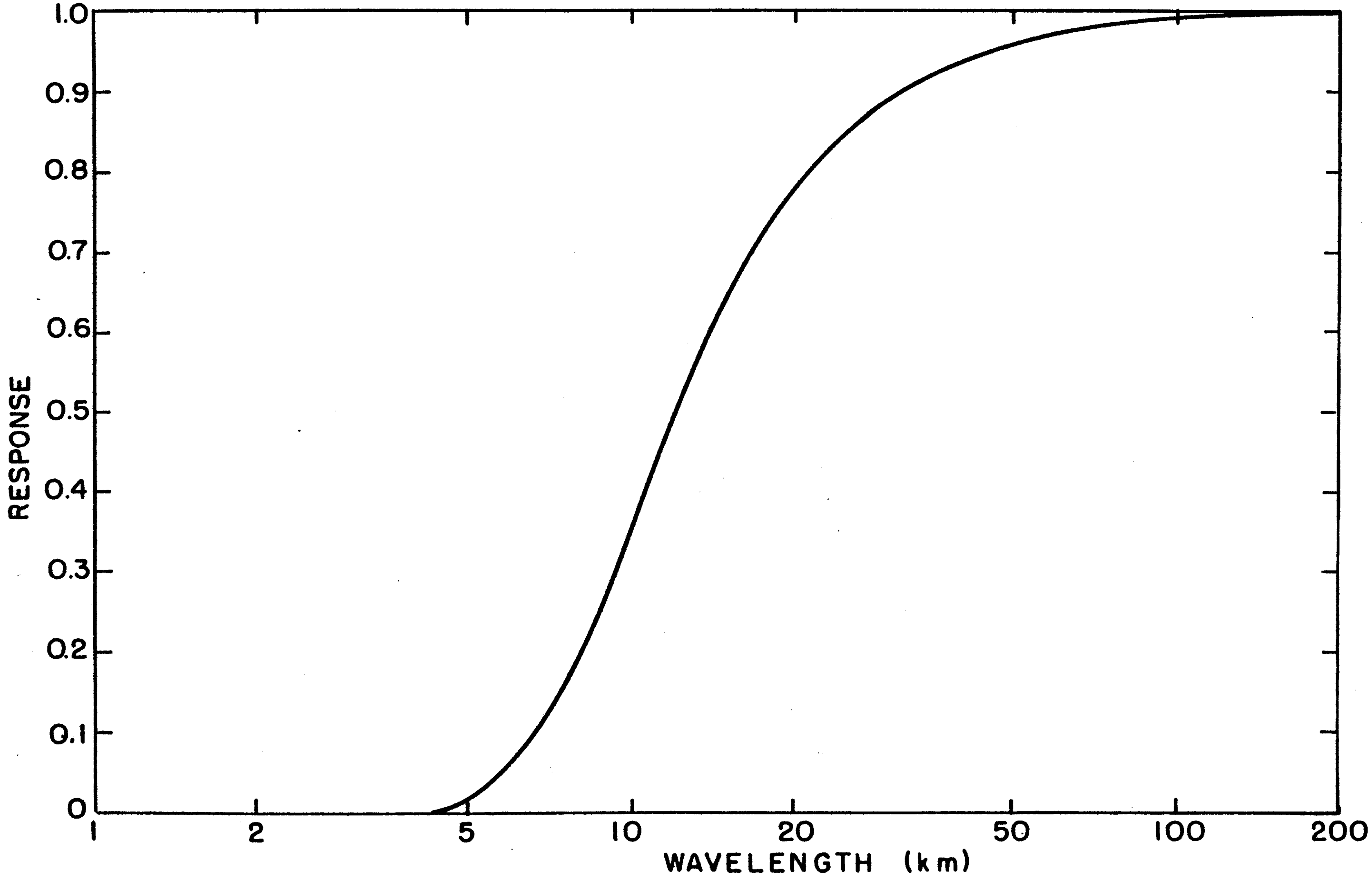

Figure 4.19. Response versus wavelength for the low-pass, normal-weighting filter used in the x direction.

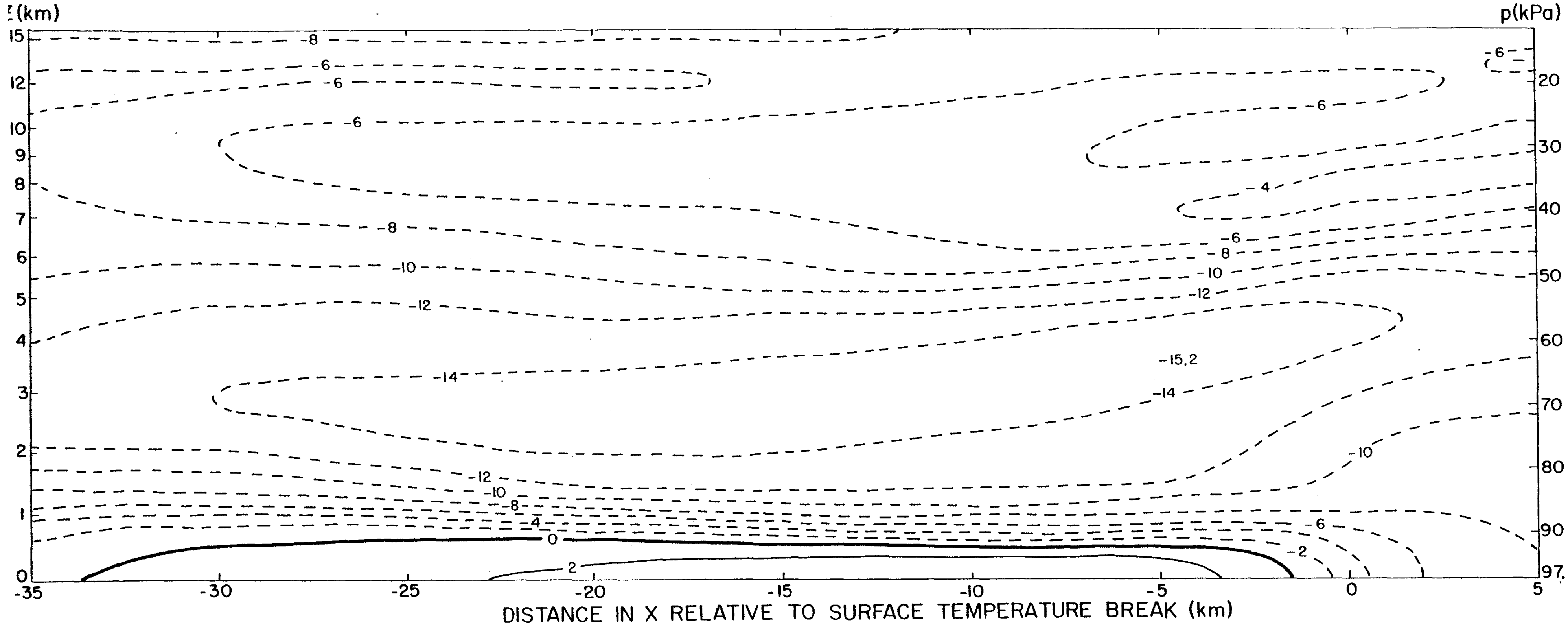

Figure 4.20. The field of $\{[u]\}$ (relative to the movement of the TB) averaged over 107.3 min to 165.4 min. Units are m s^{-1}, with contours at intervals of 2 m s^{-1} and negative isopleths dashed.

The same thing happened with SE's analysis - the leading edge of their forward motion is back at -10 km.

The oscillatory structure over and ahead of the TB is associated with the lee wave there. Comparing this structure with SE's field of u (Fig. 4.2) we see that ahead of the SWS they have essentially the same structure, with maximum leftwards motion at about 60 kPa and local minima of leftwards motion at about 40 kPa and 80 kPa. (Our field shows a change in gradient at 80 kPa but not quite a local minimum.) Evidently, there was some sort of gravity wave ahead of the system on 14 May that had the same structure as ours. Yet over the SWS their isotachs slope up to the left, in exactly the wrong direction for a lee wave. Consequently, their downdraft increases upwards to reach its maximum at or above 40 kPa. In our field of $\{[u]\}$ the isotachs in the same region slope down to the left, producing a vertical oscillation in the sign of w. We will have more to say about the differences over the SWS/TB.

In other regions the two fields compare reasonably well. In particular, our peak motion to the left is -15.2 m s^{-1} at 60 kPa and -4 km while SE's is about -17 m s^{-1} at the same level but a little farther back at -16 km.

The field of $\{[w]\}$ over the same range in x is given in Fig. 4.21. Over the TB we again have the lee wave structure, but the amplitude is markedly smaller than for individual times (see Fig. 4.12, for example). This is a result of the filtering in x; the unfiltered field $[w]$ has a 3.1 m s^{-1} updraft near the

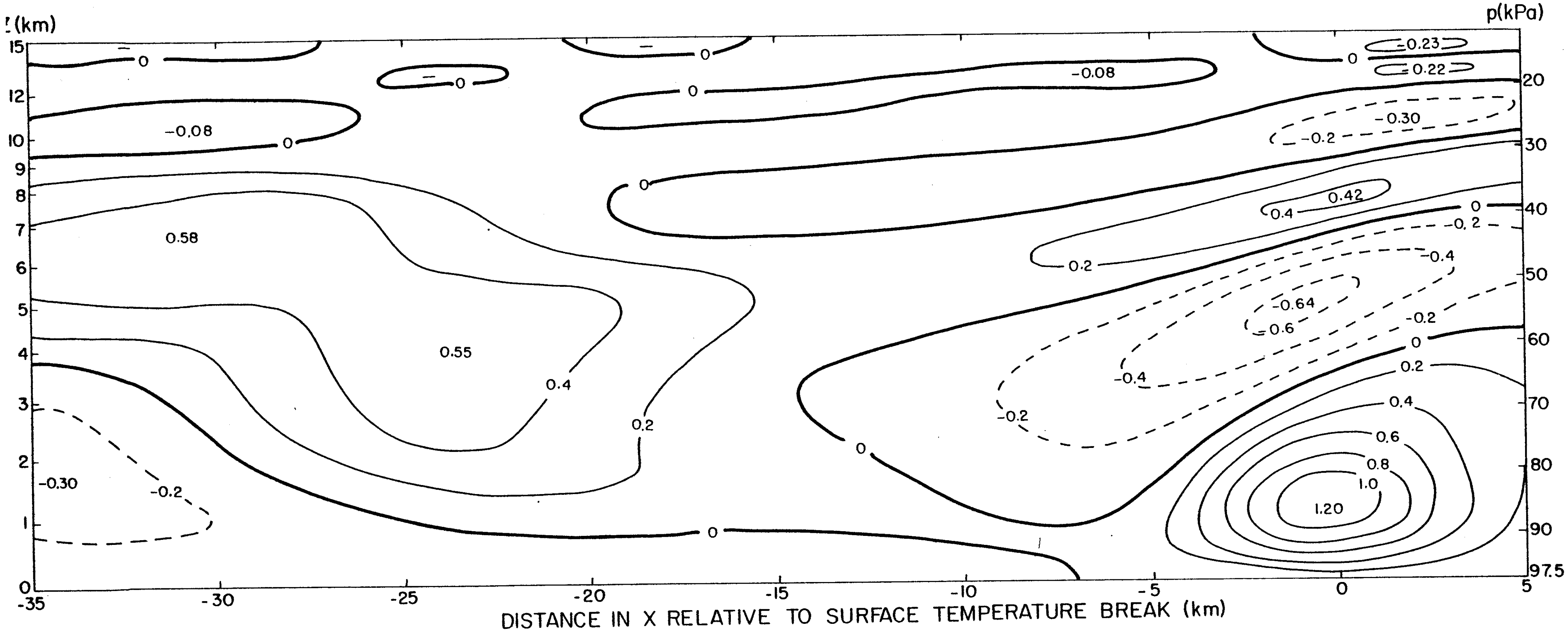

Figure 4.21. The field of {[w]}, averaged over 107.3 min to 165.4 min. Units are m s^{-1}, with contours at intervals of 0.2 m s^{-1} and negative isopleths dashed.

ground and a -1.2 m s^{-1} first downdraft aloft. Judging from the graph of the filter response (Fig. 4.19) this indicates that the effective wavelength of the lee wave is about 12 km, for a 50% response.

The averaged effect of the convective cells moving back and growing taller and stronger is evident in the broad area of upward motion sloping up and back, starting at -7 km. The peaks within this of almost 0.6 m s^{-1}, 25 to 30 km behind the TB, correspond to the average position of peak development of the cells. Between the ground and the zero isopleth is a region of downward motion which deepens towards the left; this is the downdraft air associated with the rain. The peak downdraft is about -0.3 m s^{-1} at -35 km.

Fig. 4.22 shows both $\{[u]\}$ (light) and $\{[w]\}$ (heavy) from 35 km to 75 km behind the TB. The $\{[u]\}$ field has little interesting structure; in particular, there is no hint of any midlevel inflow into the system from the rear as occurred on 14 May. The $\{[w]\}$ field has generally upward motion above 4 km or 60 kPa, in association with anvil cloud based at about 6 km, and downward motion below 4 km. This downward motion is helped by light rain falling from the anvil, but the absence of rain to the left of -65 km, in a region of continuing subsidence, suggests that there is also dynamic forcing from divergence in the cold air beneath, as Miller and Betts (1977) found in their squall line simulation.

In comparison with the mesoscale updraft analyzed for

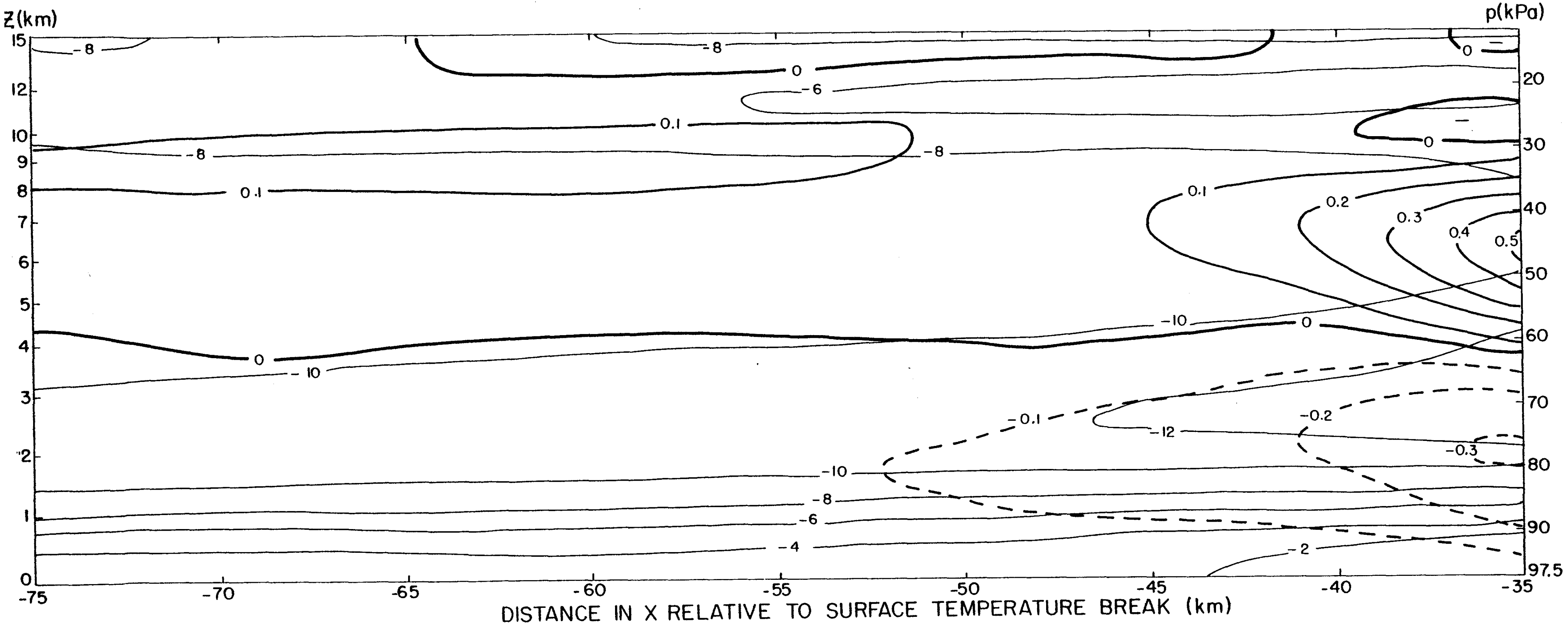

Figure 4.22. The fields of $\{[u]\}$ and $\{[w]\}$ for 35 km to 75 km behind the TB, averaged over 107.3 min to 165.4 min. Units are m s^{-1}, with $\{[u]\}$ contours (light) at intervals of 2 m s^{-1} and $\{[w]\}$ contours (heavy) at intervals of 0.1 m s^{-1}. Negative isotachs are dashed.

14 May by SE (Fig. 4.2), the model updraft's location at 45 kPa and -27 km is similar, but it has only a quarter of the amplitude. Furthermore, the updraft merely represents the averaged effect of cells going by, with mostly upward but sometimes strong downward motion, rather than being a persistent, saturated mesoscale updraft as occurred on 14 May. The key difference is the mesoscale saturation. Once this was achieved on 14 May, the updraft was self-sustaining because the associated lifting, in combination with some moistening of the dry air aloft by cumulus convection, was enough to continue saturating a deep layer of air entering the system, thus providing latent heat release to drive the updraft. The initial saturation probably resulted from a weaker convection-induced mesoscale updraft acting on accumulated debris from the convection. But in the numerical simulation the initial mesoscale saturation was never achieved, for the following conjectured reasons:

(1) The simulated cells were weaker and smaller than the actual cells, mainly because of the crudeness of the third dimension, so produced less cloud and rain debris.

(2) It was very difficult for the cloud and rain areas to expand in the third dimension, since they had to do this by a "quantum jump" across the 4 km grid spacing rather than slowly expanding as would have occurred in nature (and did occur in the x direction with the better resolution). So about the only regions where cloud extended across the entire domain in y were in the two-dimensional

lifting zone over the cold pool and in the anvil outflow aloft. And most of the rain fell on the central plane, whereas the 14 May radar data showed the echo lines to be relatively continuous.

(3) In nature, new cells might prefer to develop in a staggered arrangement somewhat like the squares of one colour on a chess board, resulting in a better coverage of debris in the y direction. In the model, this preference probably caused the occasional side plane cell developments but because of the model assumptions these could not grow strongly.

(4) If the mesoscale downdraft over the SWS on 14 May did occur, it would have developed before the updraft, in response to the initial convection and evaporative cooling aloft. By continuity this would have been associated with nearby "compensating uplift" which may have produced the initial mesoscale saturation from the convection debris. In the model, there was no such mesoscale downdraft to do this.

These reasons all emphasize how important it is to resolve the three-dimensional details of the cumulus as well as possible. Our choice of only three grid-points in y and assumed symmetry, made to minimize required computer resources while incorporating some three-dimensionality in the model, seems not to be good enough to simulate the development of the saturated mesoscale updraft.

The other feature of the 14 May system we were looking for in the simulation was the mesoscale downdraft over the surface wind shift, driven by evaporative cooling from the tops of cumulus clouds. No such feature developed; the "mesoscale" downdraft shown at 50 kPa over the TB (in Fig. 4.21) is instead part of a gravity wave response to air flowing up and over the pool of cold air. We can check the vertical structure of the wave by applying linear perturbation theory. Eliassen (1974) gives the following equation for a dry, inviscid, two-dimensional, anelastic, steady-state, linearised perturbation of the form[1] $W(z)\cos(kx)$:

$$\frac{d^2(\bar{\rho}^{\frac{1}{2}}W)}{dz^2} + (\ell^2 - k^2)(\bar{\rho}^{\frac{1}{2}}W) = 0 \tag{4.10}$$

where

$$\ell^2 = \frac{1}{\bar{U}^2}\frac{g}{\bar{\theta}}\frac{d\bar{\theta}}{dz} - \frac{1}{\bar{U}}\frac{d^2\bar{U}}{dz^2} \tag{4.11}$$

is the "Scorer parameter". The $\bar{U}$ velocity is relative to the co-ordinate system in which the wave is stationary, that is, relative to the TB in this case.

The vertical profile of ℓ^2 was obtained from the fields of $\{[\theta']\}$ and $\{[u]\}$ in the vicinity of the TB, with the local effects of the gravity wave removed by averaging over a wave-

---

[1] Although this wave has no sloping phase lines like the lee wave it will give us the vertical structure.

length of 12 km. This was then smoothed, and values taken off every 500 m in z, with linear interpolation for intermediate points. The profile is graphed in Fig. 4.23. Below 2 km the raw values were affected by the pool of cold air to the left, which really is the barrier that produces the gravity wave but does not partake in it, so a constant value of 0.3 x 10^{-6} m^{-2} was used from the ground to 2 km. The peak just above 4 km is due to a large value of $d^2\bar{U}/dz^2$ above the strongest inflow into the system (itself a result of the effects of the gravity wave extending well ahead of the system). The high values aloft are due to the strong stability; because of the vertical smoothing there is no sharp transition at the tropopause height of 12 km and the smoothed ℓ^2 is too large between 10 km and 12 km.

The equation to be solved is a second-order, homogeneous, ordinary differential equation in z. Since our model has a rigid top and bottom, natural boundary conditions to apply are $W = 0$ at $z = 0$ and z = HEIGHT, with an arbitrary, non-zero dW/dz at $z = 0$ as the solution is only unique to within a multiplicative constant. But <u>both</u> upper and lower boundary conditions can only be satisfied for certain values of k; this is an eigenvalue problem for k. Computationally, we need to solve

$$W_{HEIGHT}(k) = 0$$

where W_{HEIGHT} is determined by integrating upwards from the lower boundary using the given profile of ℓ^2 and the parameter k.

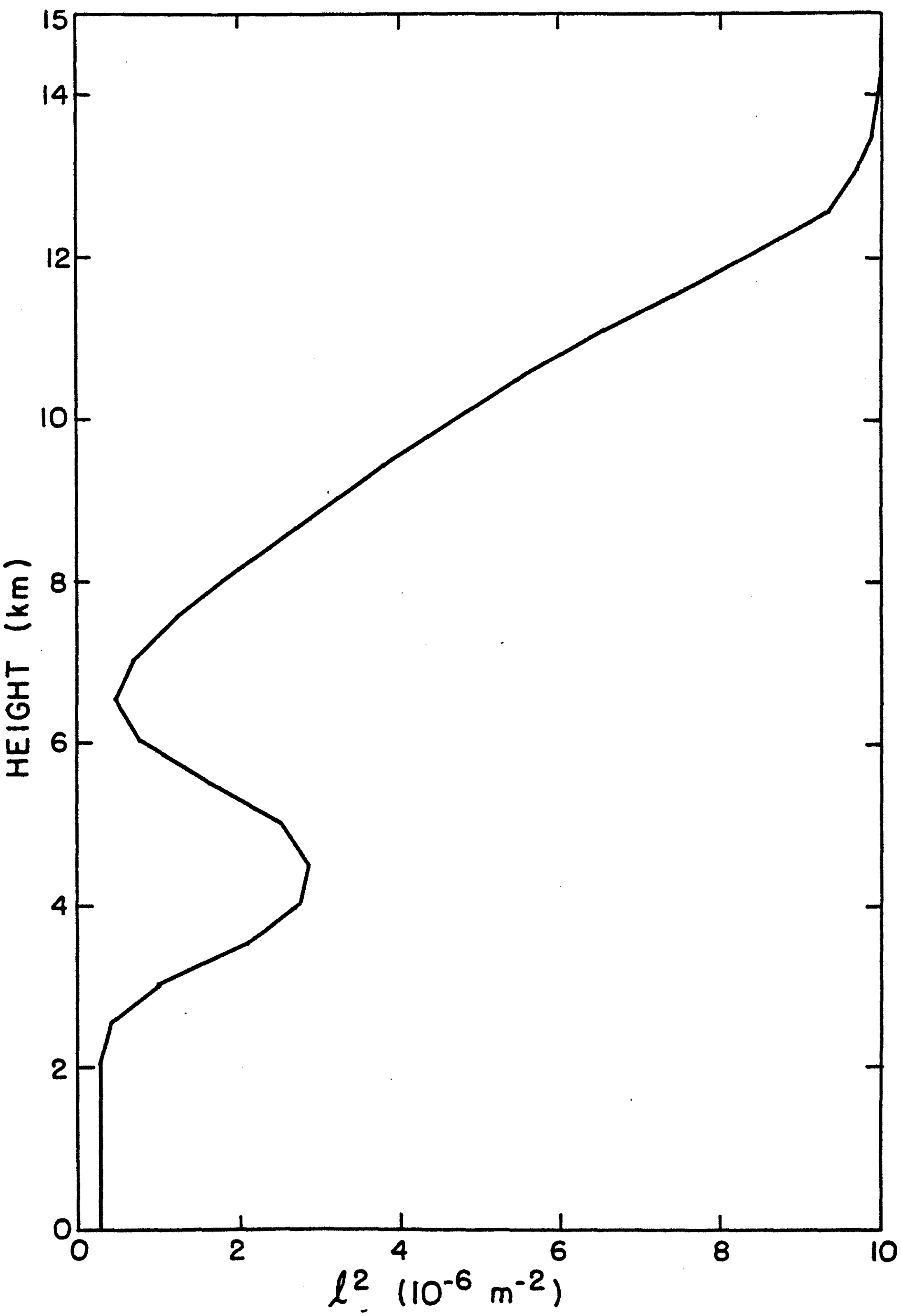

Figure 4.23. Vertical profile of the Scorer parameter, ℓ^2. This was determined from averaged fields in the neighbourhood of the TB.

This was done using a standard second-order finite-difference form for the equation, 100 m steps in z, and each of the following lower boundary conditions:

(0) $w = 0$, $dw/dz = 1$ at $z = 0$.

(1) w and dw/dz set to model values of $\{[w]\}$ above the TB at $z = 1$ km.

(2) w and dw/dz set to model values of $\{[w]\}$ above the TB at $z = 2$ km.

All eigenvalues in the horizontal wavelength range of 1 km to 100 km were found. For each lower boundary condition there were eight eigenvalues, with the wavelengths enumerated in Table 4.1 below.

TABLE 4.1. Horizontal wavelengths in kilometres of the eigenvalues for the three different lower boundary conditions.

Eigenvalue No.	L_0	L_1	L_2
1	2.10	2.10	2.10
2	2.39	2.39	2.39
3	2.81	2.81	2.81
4	3.46	3.46	3.46
5	4.51	4.51	4.42
6	4.67	4.67	4.66
7	7.94	7.86	6.25
8	13.15	11.31	8.73

The vertical structure of the first eigenvalue mode has only one turning point, the second two, and so on. Only the longest horizontal wavelength modes (with eight turning points) correspond to the actual vertical structure in the model.[1] These modes are graphed in Fig. 4.24 as W_0, W_1, and W_2 for the three boundary conditions, together with the model structure, W_m. The three solutions are normalized so that the magnitude of the first minimum above the ground is the same as for W_m. The following points are noted:

(a) The locations of the maxima and minima below 10 km match exceedingly well to W_m.

(b) Above 10 km the model resolution is too poor (grid-point values of W_m are marked with dots) to resolve the theoretical structure. Further, the theoretical vertical wavelength in the 10 km to 12 km layer is a little too short because as noted previously the vertical smoothing of ℓ^2 produced too-large values of ℓ^2 there.

(c) The first W_0 updraft is 2 km higher than for W_m; the model updraft is not part of the gravity wave but rather is forcing it.

(d) The W_1 solution matches W_m the best.

(e) The W_2 solution matches comparatively poorly, with far too strong an updraft at 7.5 km. Also, the horizontal wavelength of 8.73 km is too short.

(f) The horizontal wavelengths of 13.15 km for W_0 and 11.31 km for W_1 match the approximately 12 km wavelength in the model.

---

[1] The seventh modes all have a first downdraft at a height of about 7.5 km and look reasonable. All the other modes have unrealistically large magnitudes at middle and high levels compared with lower down (due to $\ell^2 - k^2$ attaining negative values).

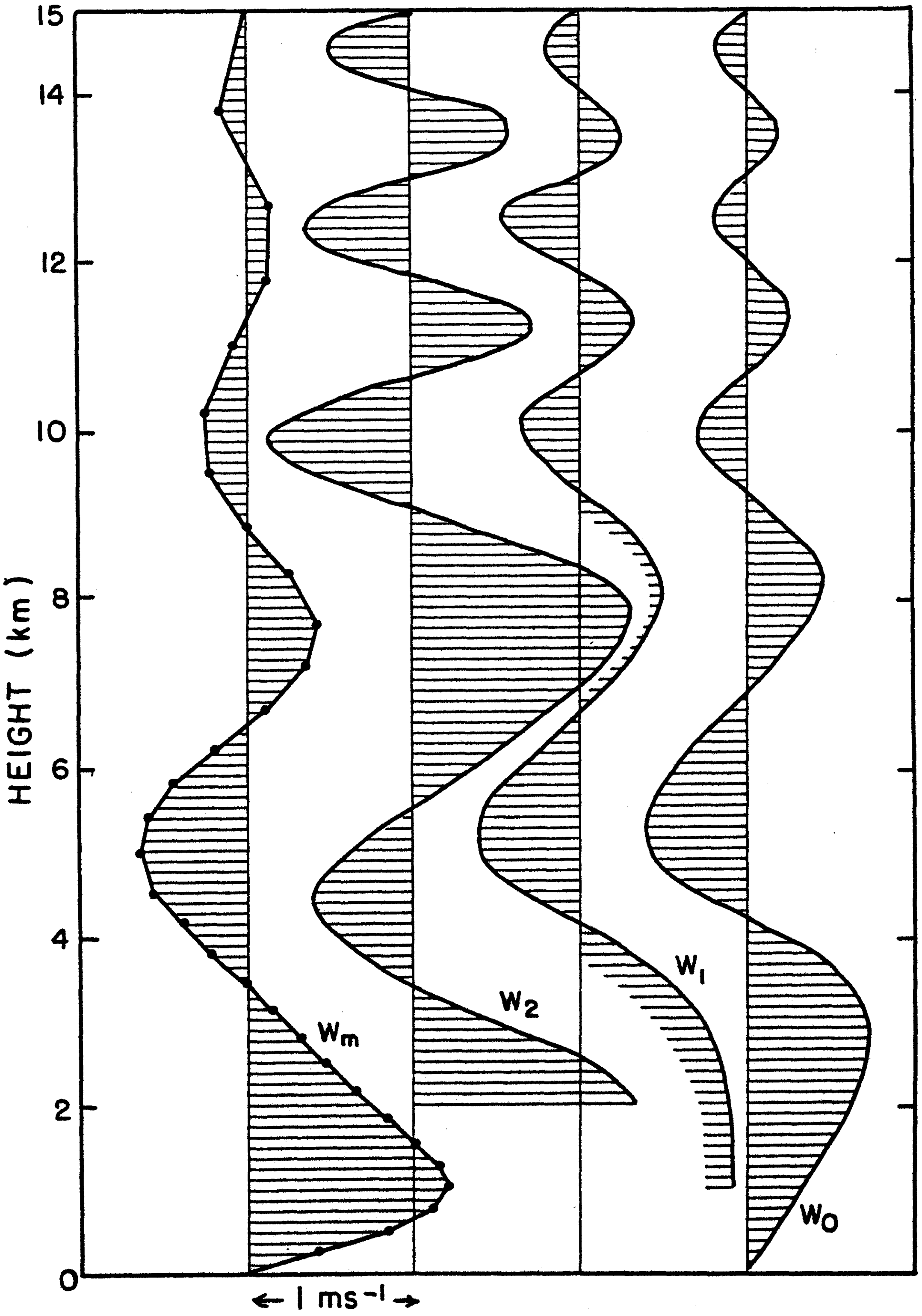

Figure 4.24. Vertical structure of the model vertical velocity (W_m) directly over the TB, and theoretical structures for three different lower boundary conditions (W_2, W_1, W_0).

The excellent correspondence in structure between theory and the model (<u>and</u> of course the actual system, since SE's u field showed the same structure) leads us to believe that the lee wave is a real phenomenon and not an artificial result produced by the model. Physically we would expect a type of lee wave to develop, in dry air, since the cold pool was acting like a moving mountain barrier over which the air had to flow. The presence of a rigid lid at 15 km may have had some quantitative effect on the wave (by not allowing it to continue propagating vertically) but qualitatively the lee wave is plausible. Other numerical simulations of gust fronts, such as that of Mitchell and Hovermale (1977) used models with lower lids that did not allow a lee wave to develop.

The problem is that the air was not dry, but moist and conditionally unstable. So with lifting and condensation in potentially unstable air over the TB why did we not instead get deep cumulus convection, breaking up the lee wave? The answer is that we did. But in the initial stages of growth the cumuli that broke off from the cloud over the TB were only modulations on the larger-scale lee wave, as is evident from the averaged vertical velocity field in Fig. 4.21. Only after the cumuli had traversed the average downdraft region of the wave did they develop strongly and break up the wave. In the downdraft region their development was slowed because of pressure forces from the lee wave in the dry air aloft.[1] (Being embedded in air of strong vertical wind shear must also have inhibited their development somewhat.)

The suppressing effect of the lee wave varied according to how strong it was; we noted in Section 4.3.2.1 that the gap in cell development was associated with a strengthening of the downdraft region that apparently expunged a new cell that was attempting to develop. Why did the downdraft strengthen? To answer this question we examined the time variation of both the peak upward motion on the central plane at the TB and the first peak downdraft directly above it. These are graphed[2] in Fig. 4.25. The overall downward slope of W_{UP} shows clearly the decreasing strength of the system, but there are also three maxima at 75 min, 140 min, and 205 min. These are followed from 10 to 20 min later by maximum amplitudes of W_{DOWN}, which in turn (see Fig. 4.6) correspond to gaps in cell development. But why is there a time delay between the peak W_{UP} and W_{DOWN}? Apparently because a change of amplitude of the forcing is propagated through the wave at the group velocity. Since the wave

---

[1] In the anelastic equations the pressure forces act to maintain mass continuity despite other forces. The air in the incipient cumulus cloud attempting to ascend needs to diverge strongly in the horizontal as it approaches the descending air of the lee wave in the dry air above; to maintain continuity, the pressure field responds with a high pressure region which acts to produce the horizontal divergence, <u>and</u> acts to weaken upward accelerations towards it and hence the growth of the cloud.

[2] The raw values of W_{UP} and W_{DOWN} were rather noisy because of space truncation error (quadratic interpolation in x might have given more consistent values) so they were smoothed in time with a 1-2-1 filter.

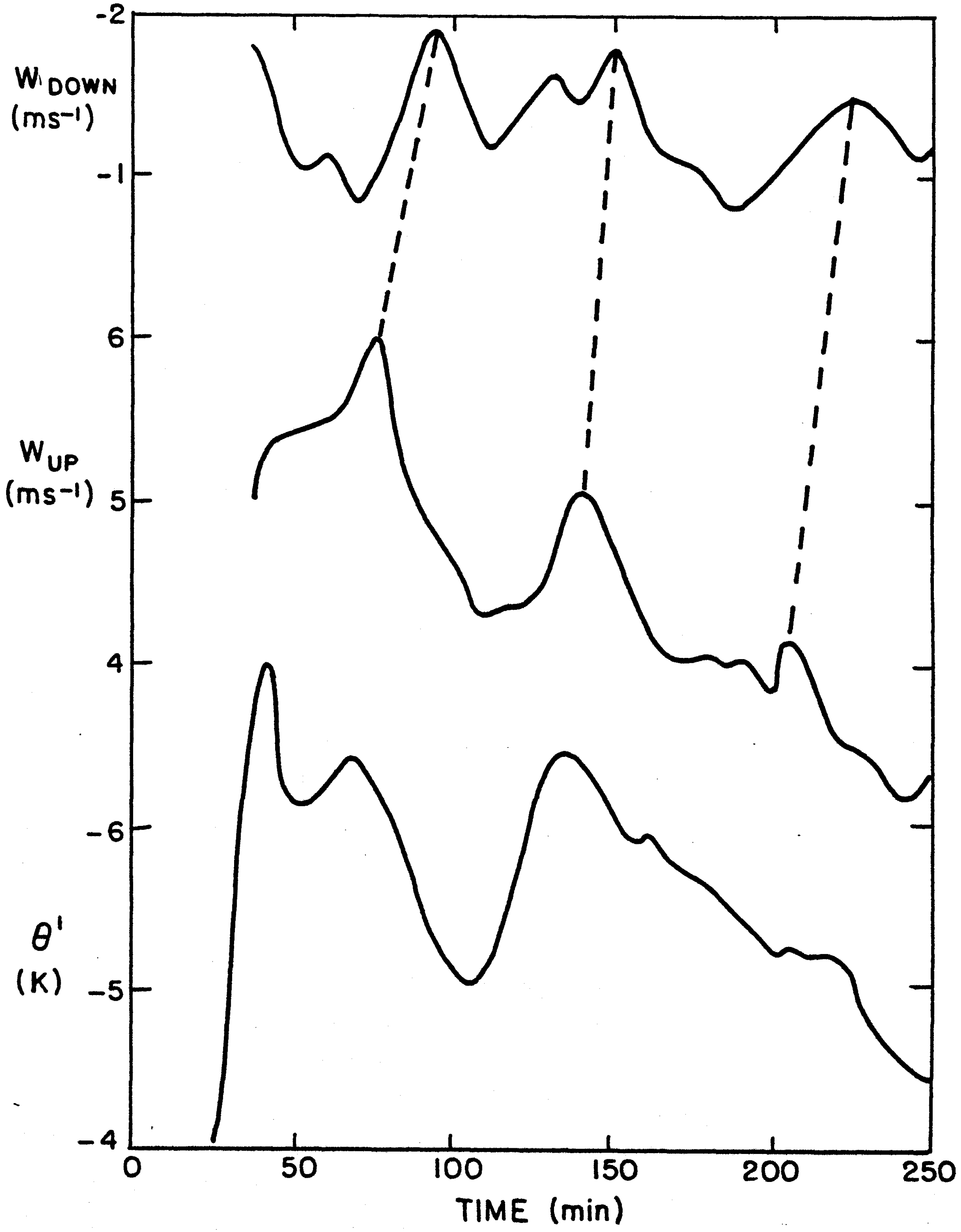

Figure 4.25. Time variation of the potential temperature perturbation 5 km behind the TB (θ'), the strongest updraft over the TB (W_{UP}) and the downdraft immediately above that (W_{DOWN}). Associated peak magnitudes of W_{UP} and W_{DOWN} are linked with dashed lines. All values are on the central plane.

stays anchored to the TB, its phase velocity in the horizontal, relative to the air at a level of about 2 km, is +12 m s^{-1}. For a horizontal wavelength of 12 km and a vertical wavelength of 8 km (the updraft and first downdraft are 4 km apart) the vertical phase velocity is downward at -8 m s^{-1}. The corresponding group velocities are +8.3 m s^{-1} in the horizontal relative to the air (-3.7 m s^{-1} relative to the TB) and +5.5 m s^{-1} in the vertical. So the increase in amplitude should take about 12 min to travel 4 km upwards, in accord with the 10 to 20 min observed in the model, and about 27 min to travel 6 km backwards to the downdraft behind the TB. Consequently we would expect the worst times for attempted new cells to pass through the downdraft region to be the times of peak TB updraft plus about 25 min, i.e., at 100 min, 165 min, and 230 min. Referring to Fig. 4.6 we see that these are indeed the times for which an anticipated new cell failed to develop.

We still need to explain the periodic maxima in the updraft over the TB. Examination of the temperature fields showed that, following the first rain at the ground from the first cell of a series, colder air produced by evaporative cooling[1] slowly began to spread forward within the cold pool, accelerating as more cold air was produced by more extensive and heavier rain. The approach of this surge of colder air

---

[1] As on 14 May there were never any strong penetrative downdrafts in the model, bringing down large amounts of potentially cold mid-tropospheric air. The colder air was mostly produced by <u>in situ</u> evaporative cooling.

near the TB produced stronger forward velocities behind the TB, stronger convergence, and stronger upward motion. To illustrate its approach, Fig. 4.25 also shows the time variation of θ' on the central plane, 5 km behind the TB. Note that the temperature minima come about 5 min earlier than the updraft maxima. (However, there is no corresponding temperature minimum for the weak updraft maximum at 205 min. This is puzzling, since the amplitude response of the downdraft is just as strong. Perhaps the nearby convection also helps to strengthen the downdraft.)

As an example, colder air began to form at about 70 min at 10 to 12 km behind the TB as the first rain fell from cell (2). This surge slowly moved forward relative to the TB, eventually producing a peak updraft at 136.8 min. This was followed by a strengthening of the first downdraft so that 14 min later (Fig. 4.11 (a)) the next attempt at a new cell was squashed.

While the lee wave structure and its time variation is interesting, it evidently represents a different mode of behaviour from that on 14 May. Even though the 14 May system was associated with a cold front and not just a spreading pool of cold air, there was evidence of a standing gravity wave (with the same vertical structure) ahead of the SWS, presumably excited by the convection and the cold front. But over the SWS it was apparently precluded by deep convection. It is possible that incoming, pre-existing cumuli[1] were given enough of a

---

[1] Surface observations suggested that there was some towering cumulus ahead of the system, and several of the rawinsonde soundings taken within 30 min before the passage of the SWS showed evidence of saturation or near saturation at a level of about 4 km.

boost by the uplift at the SWS to penetrate deeply enough to break up any attempt at a lee wave, and thus providing a source of water to drive the downdraft. In the numerical simulation the first condensation took place right at the TB and the cumulus clouds did not get a head start, so to speak. It might be of interest to perform a simulation with surface heating or some other forcing ahead of the TB to produce a pre-existing field of cumuli.

4.3.3.3 Other Fields

The final averaged field presented, in Fig. 4.26, is of $\{[\theta']\}$ over +5 km to -35 km. The cold pool stands out clearly, with the coldest air about -14 km. At the leading edge of the cold air the strong temperature gradient (i.e., the TB) has been smoothed out by the filtering in x. Above the TB the -1.0 K minimum is due to mostly dry-adiabatic lifting of air over the cold pool. There is a tongue of relatively warm air between the minimum and the cold pool, produced by latent heat release in the cloud over the TB. Aloft, the vertical structure is again due to the lee wave. Farther left there is little effect of the convection on the averaged temperature field; as in SP's analysis of the 14 May θ field the isotherms remain almost horizontal through the system. In both cases this is due to latent heating counterbalancing the expected dry-adiabatic cooling in the mesoscale updraft. But the heating took place in the convective cells in the model, and mostly in

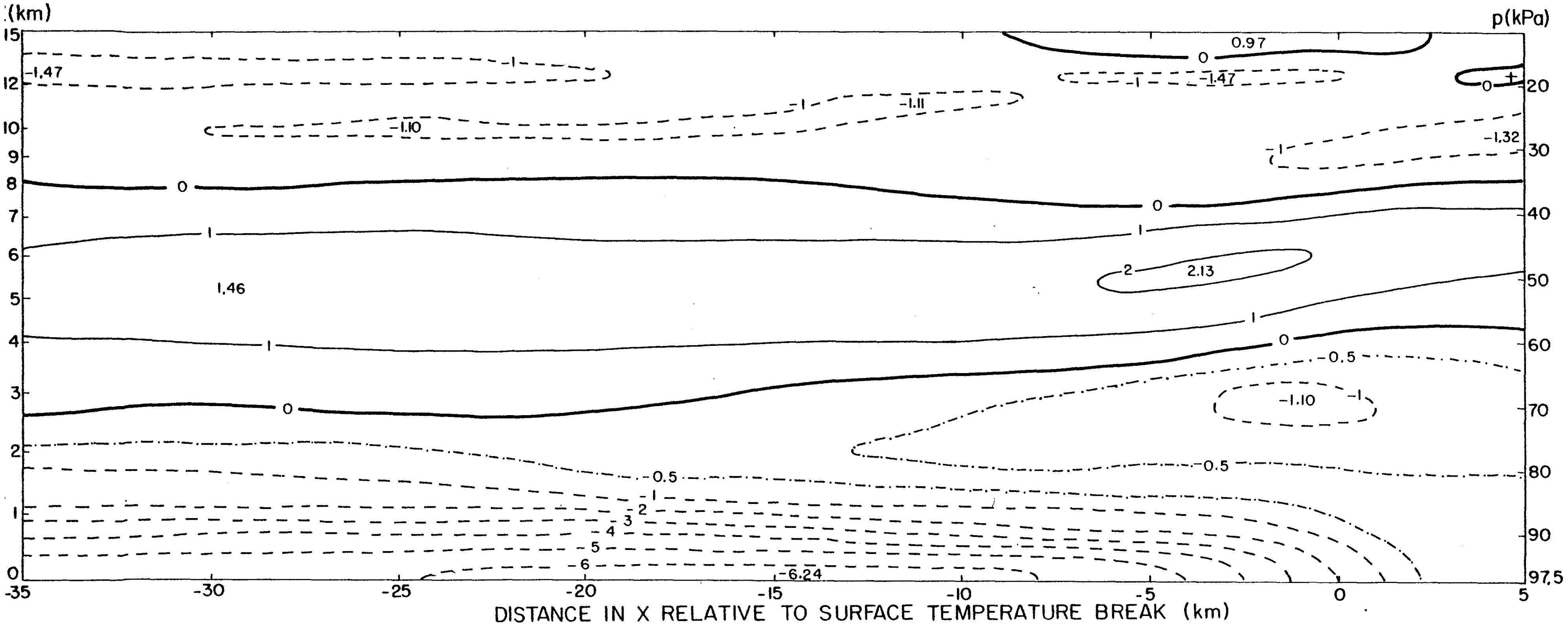

Figure 4.26. The field of $\{[\theta']\}$ averaged over 107.3 min to 165.4 min. Units are degrees kelvin, with contours at 1 K intervals and negative isotherms dashed.

the saturated mesoscale updraft itself on 14 May.

Fig. 4.27 (a) shows the apparent source of potential temperature, $\dot{\theta}^A$, derived from the three fields $\{[u]\}$, $\{[w]\}$, and $\{[\theta']\}$. The heating/cooling doublet at the ground near the TB is almost entirely due to the virtual source, i.e., it is due to fluctuations in time and in y[1] of the TB position relative to the grid that result in an eddy flux of heat from warm to cold air.

Above the TB the apparent heating of $+350 \times 10^{-5}$ K s^{-1} is mostly due to latent heat release in the cloud there. The cooling of -91 behind that is mostly due to diffusion at the top of the cold pool, as we shall see in Fig. 4.31. Farther back, there is a sloping region of apparent heating due to the convection, partly because of latent heating and partly (in its upper part) because of vertical eddy flux divergence. Fig. 4.27 (b) continues the field of $\dot{\theta}^A$ back to -75 km and we see that the apparent heating extends back into the anvil region.

Below the heating there is apparent cooling, mostly due to evaporation of rain, with the strongest cooling at -34 km. But close to the ground, everywhere behind the TB, diffusive heating overcomes the evaporative cooling to give net apparent heating.

The real source of potential temperature, $\dot{\theta}^R$, is shown in Fig. 4.28. This should represent only latent heating and

---

[1] During the run, the TB position on the side plane was as much as one grid-point or about 900 m ahead of the position on the central plane.

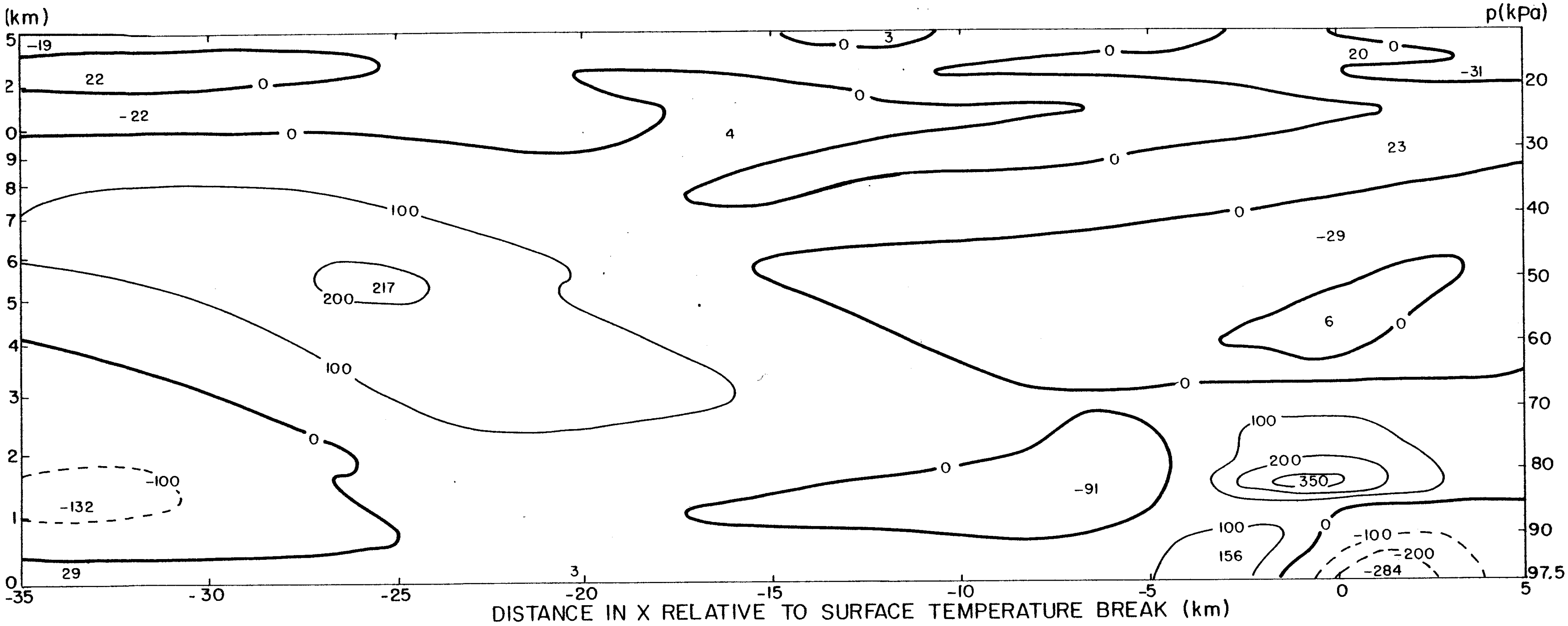

Figure 4.27. (a) The field of $\dot{\theta}^A$, the apparent source of potential temperature, for 107.3 min to 165.4 min. Units are 10^{-5} K s^{-1}, with contours at intervals of 100 x 10^{-5} K s^{-1}. Negative isopleths are dashed.

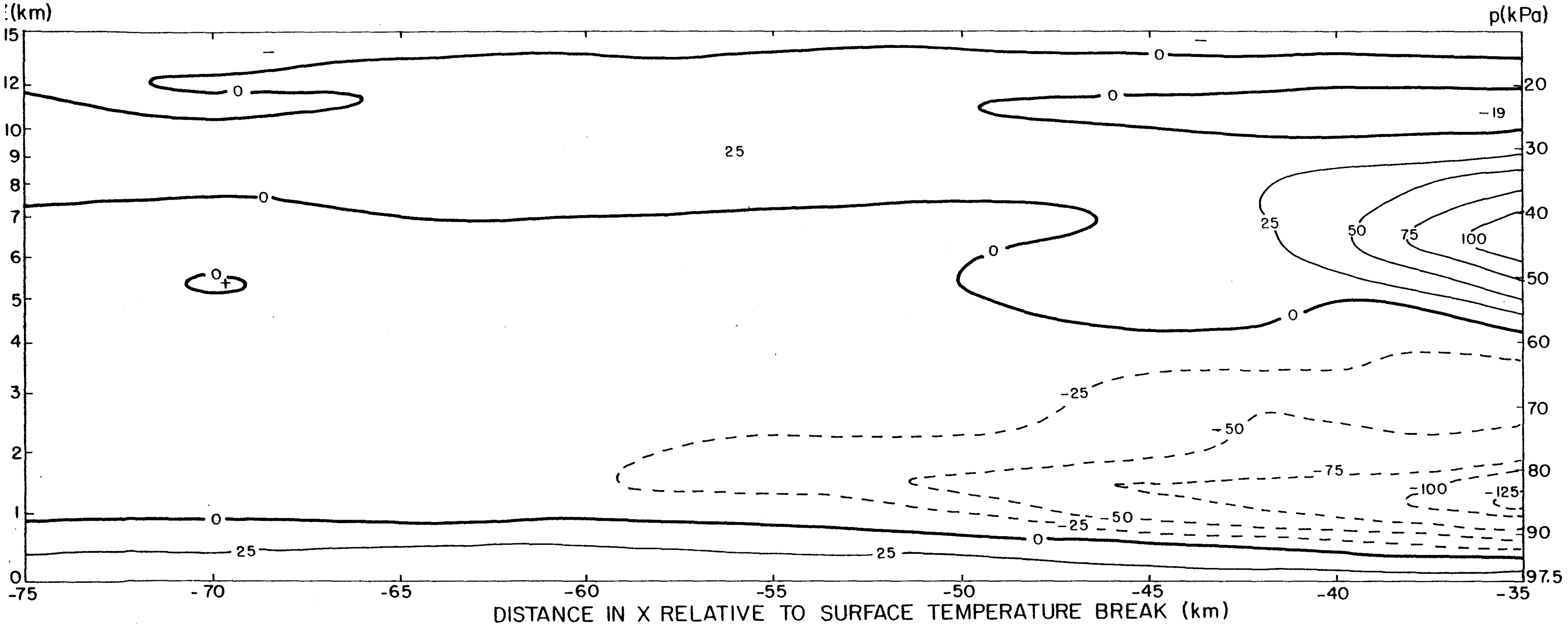

Figure 4.27. (b) As in (a) but for 35 km to 75 km behind the TB. Contours are now at intervals of 25 x 10^{-5} K s^{-1}.

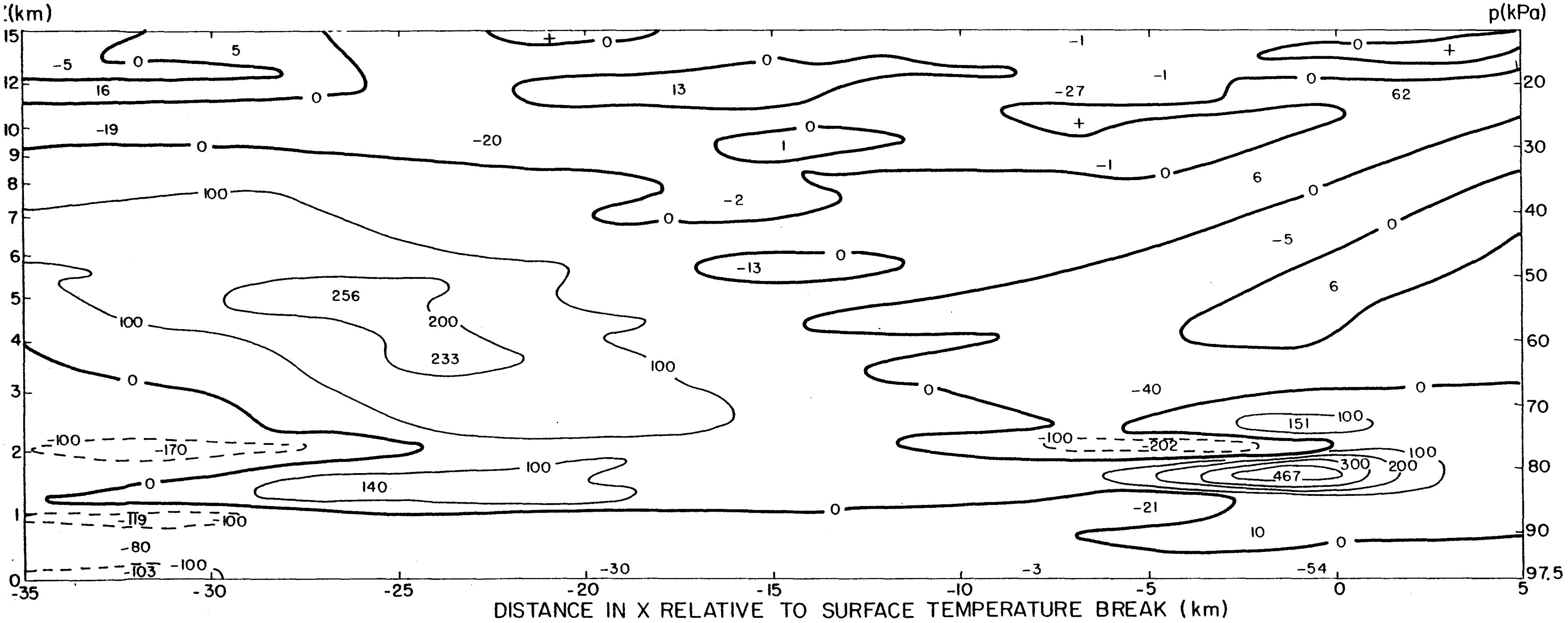

Figure 4.28. The field of $\dot{\theta}^R$, the real source of potential temperature, for 107.3 min to 165.4 min. Units are 10^{-5} K s^{-1}, with contours at intervals of 100 x 10^{-5} K s^{-1}. Negative isopleths are dashed.

cooling effects, but due to the coarse time resolution for the time integration there are some rather large values where neither condensation nor evaporation is occurring - notably at the ground near the TB, and high above the TB.

At a height of 1500 m over the TB there is strong latent heating due to cloud formation, but with a horizontal slice of cooling just above it then another maximum of heating. This cooling is an unfortunate result of the diffusion parameterization. Recall from Chapter 2 that the quantities which are diffused in the vertical are θ' and Q_v', not θ and Q_v. The justification for this was that we did not want to diffuse the base-state profiles of $\overline{\theta}$ and $\overline{Q_v}$, presuming them to be maintained by some large-scale process. But the result is that the <u>second derivative</u> in z of the base-state is untouched, not <u>the</u> base-state itself. An examination of the profile of $\overline{Q_v}$ reveals that at z = 2022 m there is a "kink" with a positive value of $d^2\overline{Q_v}/dz^2$. Consequently, $\partial^2 Q_v'/\partial z^2$ tends to be negative, resulting in diffusive drying at z = 2022 m and moistening at the levels above and below. In cloudy areas of upward motion this can even produce "first-guess" subsaturation and latent cooling at 2022 m, with correspondingly more latent heating at the next grid-point above and below. But then, fortunately, a negative feedback comes into effect. The spurious cold temperature surrounded by warm temperatures above and below results in a strong diffusion of heat back to the level of 2022 m. In fact, this diffusive heating nearly cancels the spurious latent cooling, so that the <u>net</u> apparent heating, which includes both diffusive and real sources of θ, shows no strange structure. (See Fig. 4.27 (a).)

Moving back from the TB we find a large region of latent heating, sloping up and back, due to condensation in the convective cells. Between this and the ground there is latent cooling due to evaporation of rain, with the strongest cooling near -32 km. The horizontal region of heating at a height of 1200 m near -25 km is partially a result of the layer cloud that tends to form on the side plane, forced up by the outflow from the central plane rain. (See, for example, Fig. 4.8 (b) at 122.1 min.) It is also partially due to heat and moisture diffusion at the top of the cold pool producing saturation, as will be noted when we consider $\dot{\theta}^D$.

Fig. 4.29 shows the real source of water vapour, $\dot{Q}_V^R$, which should be approximately $-(C_p/L_{vw}) \times \dot{\theta}^R$ or $-2.49 \times 10^3 \times \dot{\theta}^R$. It does match fairly well, except near the ground at the TB where there was already a problem with $\dot{\theta}^R$, and high over the TB where $\dot{Q}_V^R$ is more trustworthy due to the small magnitudes of Q_V. The only additional feature in the field of $\dot{Q}_V^R$ that was not commented on for $\dot{\theta}^R$ is the source of water vapour (and sink of θ) above the sloping condensation region, corresponding to evaporation from the tops of the convective cells. But note that the evaporation doesn't extend much higher than 3 km near the TB, so evaporative cooling cannot be invoked as a driving force for the downdraft at a height of 5 km.

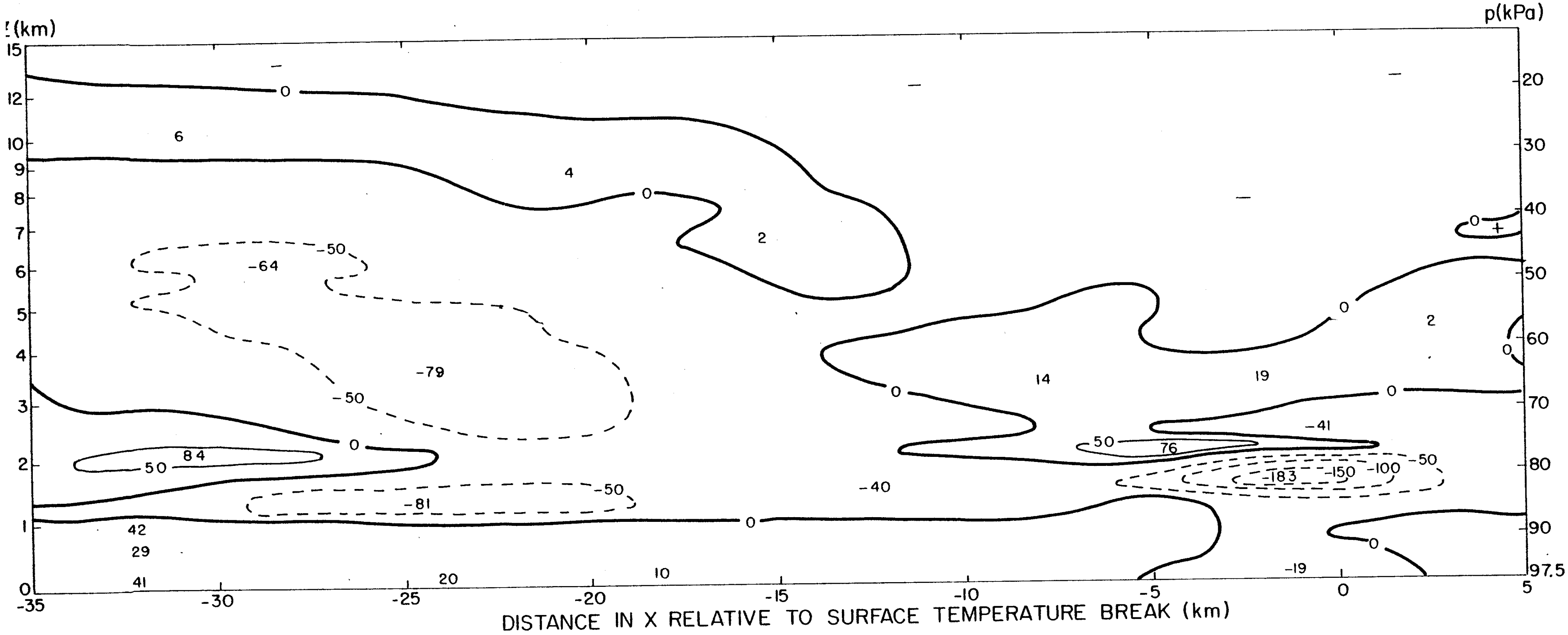

Figure 4.29. The field of $\dot{Q}_v^R$, the real source of water vapour, for 107.3 min to 165.4 min. Units are 10^{-5} g kg^{-1} s^{-1}, with contours at intervals of 50×10^{-5} g kg^{-1} s^{-1}. Negative isopleths are dashed.

The virtual source of potential temperature, $\dot{\theta}^{v}$, is in Fig. 4.30. Near the ground at the TB is the same doublet that was noted in the apparent source of θ. A coupled source and sink due to the vertical eddy fluxes of the convective cells slopes up and back from the TB, and is sufficiently strong to elevate the level of maximum apparent heating (5.5 km) over that of the maximum latent heat (4.5 km). In the lee wave region above the TB there are no strong sources or sinks, so any fluctuations in time or space from the mean lee wave have little effect. Near the ground, there is a source/sink doublet everywhere to the left of -7 km; this is a consequence of colder air and stronger subsidence on the central plane than on the side plane.

The horizontal and vertical eddy flux divergences that together comprise $\dot{\theta}^{v}$ were also computed separately. Almost everywhere the horizontal component was an order of magnitude less than the vertical component, as might be expected for vertical convection. The horizontal component was significant only near the ground at the TB, and in the lee wave above the TB where it tended to be 180° out of phase with the vertical component and was of small magnitude (about 15×10^{-5} K s^{-1}) anyway.

Fig. 4.31 shows the diffusive source of potential temperature, $\dot{\theta}^{D}$. Again, this is dominated by vertical rather than horizontal diffusion since the gradients are generally stronger in the vertical. There is a lot of structure above 3 km that

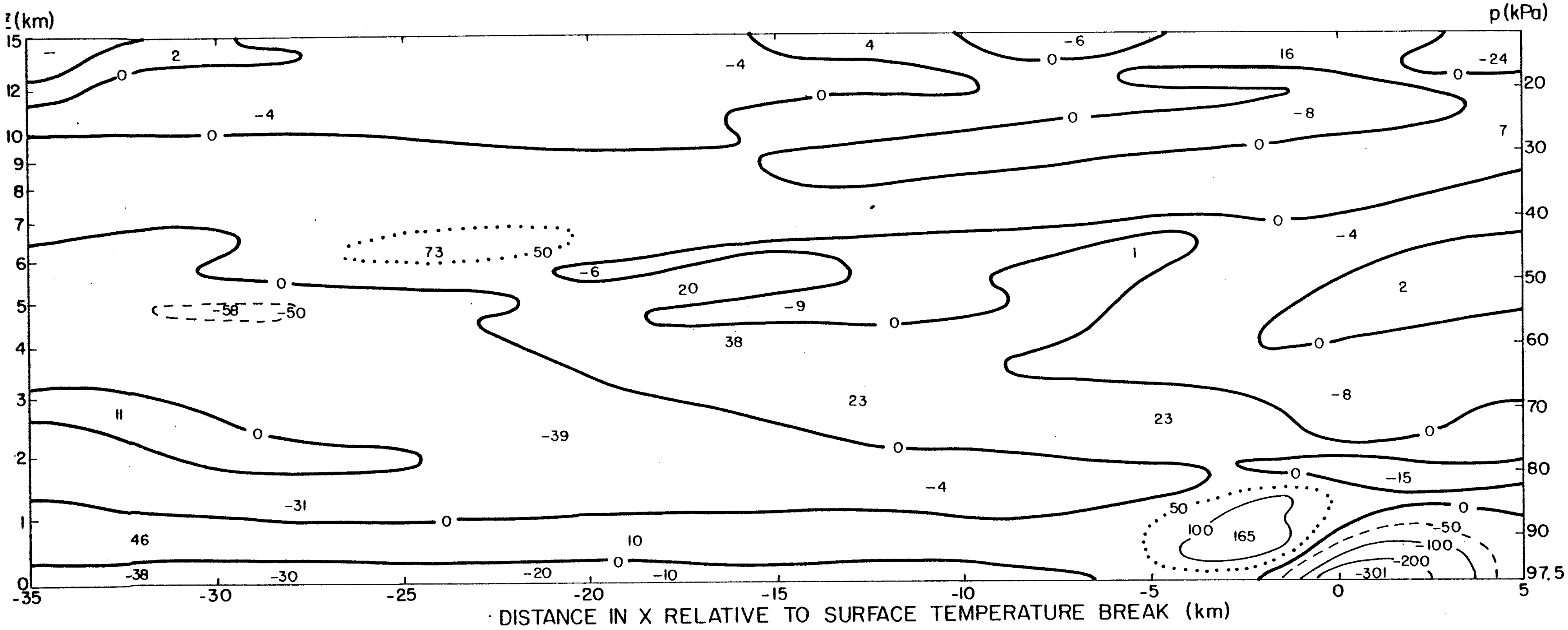

Figure 4.30. The field of $\dot{\theta}^v$, the virtual source of potential temperature, for 107.3 min to 165.4 min. Units are 10^{-5} K s^{-1}, with contours at intervals of 100 x 10^{-5} K s^{-1}, with the addition of a +50 x 10^{-5} K s^{-1} isopleth (dotted) and -50 x 10^{-5} K s^{-1} isopleth (dashed).

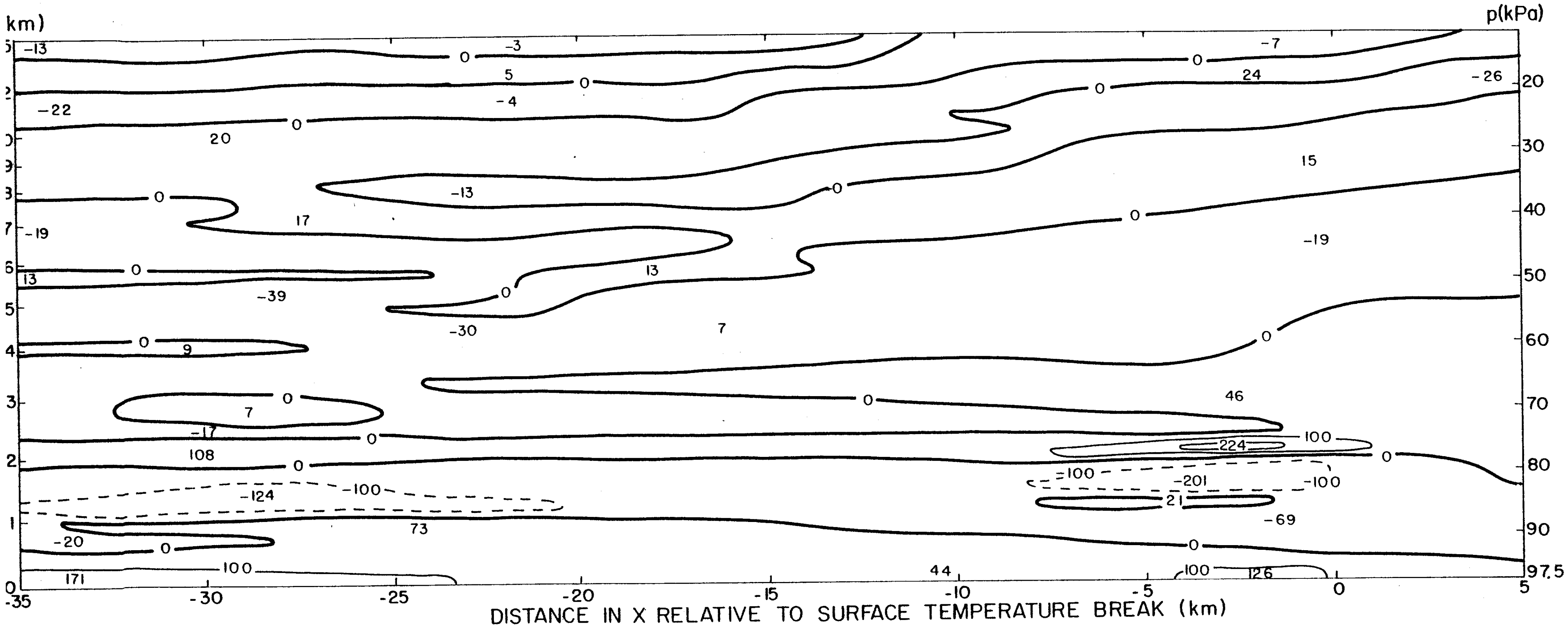

Figure 4.31. The field of $\dot{\theta}^{D}$, the diffusive source of potential temperature, for 107.3 min to 165.4 min. Units are 10^{-5} K s^{-1}, with contours at intervals of 100 x 10^{-5} K s^{-1}. Negative isopleths are dashed.

is mostly of small magnitude. Below 3 km the following features should be noted:

(1) Diffusion heats the pool of cold air at the ground rather strongly, with a peak of 171 x 10^{-5} K s^{-1} at -33 km where the averaged evaporative-cooling rate is only -103 x 10^{-5} K s^{-1}. The net warming of the cold pool[1] due to this diffusion causes the slow weakening of the system.

(2) The diffusive heating cannot come from below (the lower boundary condition is $\partial\theta'/\partial z = 0$) so it must come by cooling the air above the cold pool. Thus we have the quasi-horizontal band of diffusive cooling extending back from a height of about 900 m over the TB to a height of 1400 m near -30 km. In effect, the cold pool is warmed by (subgrid) mixing of the warmer air streaming to the left over the top of the cold pool. Along the same band there tends to be diffusive moistening of the air (because $\partial^2 Q_v'/\partial z^2$ is positive)so the net effect of the diffusion can be to produce supersaturation and hence cloud formation even in areas of downward motion over the cold pool. The cloud formed can be likened to the stratocumulus layer that forms in the top of a well-mixed boundary layer when the mixing produces saturation.

(3) Over the TB the horizontal band of diffusive heating at 2000 m is the compensation for the aforementioned problem of diffusive drying and evaporation.

---

[1] The net warming is $\{[\partial\theta/\partial t]\}$ which includes all the contributions to the apparent source, plus advection. The main advective effect is subsidence, which does tend to warm the cold pool, but where the net warming is fastest (just above the ground) it only contributes about 10 x 10^{-5} K s^{-1}.

The various averaged fields and sources were also computed for Q_V and u. We have already seen $\dot{Q}_V^R$ (Fig. 4.26); the other sources showed similar features to those for θ.

The virtual source for u revealed that, as SE found, the eddy flux divergences did produce important horizontal forces. However, unlike in SE, there were many regions of countergradient transport. In particular, from the TB back to about -12 km the cells in their early development acted to <u>enhance</u> the vertical wind shear they were growing in. In other words, kinetic energy was transferred from the cells to the environment just as Asai (1964) found for two-dimensional convection in shear. The magnitude of the enhancement was about 8×10^{-7} s^{-2} at its peak near -7 km and a height of 2 km, enough to increase the shear by 1 m s^{-1} km^{-1} in 20 min. This kinetic energy transfer obviously helped to slow the initial growth of the cells in this region.

Behind -12 km the cells mostly transported positive momentum upwards, with a peak virtual source of 13.2×10^{-4} m s^{-2} at -30 km and a height of 5 km. This upward transport was countergradient above the peak rearwards motion at a level of 3 km and between about -20 km and -35 km. There was also some resolvable eddy transport in the shear layer near the ground, in the down-gradient sense, but it was dominated by the diffusion which produced a peak negative acceleration of -24.5×10^{-4} m s^{-2} in the cold air at -21 km and a peak positive acceleration of 27.3×10^{-4} m s^{-2} above the cold air at -29 km and a height of 2 km.

The real source for u, $\dot{u}^R$, is shown in Fig. 4.32; this should be entirely due to the horizontal pressure gradient. There is a strong negative acceleration above the TB, corresponding to the strong horizontal pressure gradient as shown for 136.8 min in Fig. 4.18. Above that, the vertical structure is due to the lee wave again. Notice that at the right the isopleths tend to level out; farther right they are almost horizontal and the magnitudes weaken. By continuity this forces a vertical velocity structure that results in the modified temperature profiles as seen at the right-hand side of Fig. 4.26.

At the ground, pressure effects of the cold air force positive acceleration, but here $\dot{u}^R$ also includes the modelled surface drag (Section 2.2.2, part 3 (c)) that was not accounted for in our simplified version of the momentum diffusion, so the positive accelerations due to pressure should be a little stronger. Aloft at the far left there is some indication of an inflow/outflow doublet of pressure-gradient accelerations, presumably due to the averaged effect of the convective cells which tend to be at their strongest at about -35 km and have low pressure beneath them and high pressure above.

4.4 Sensitivity Tests

Since the model contains so many arbitrary features - notably the domain geometry (size, grid spacings, number of grid-points in y) and the parameterizations of microphysics and diffusion - it is natural to ask how the results would be

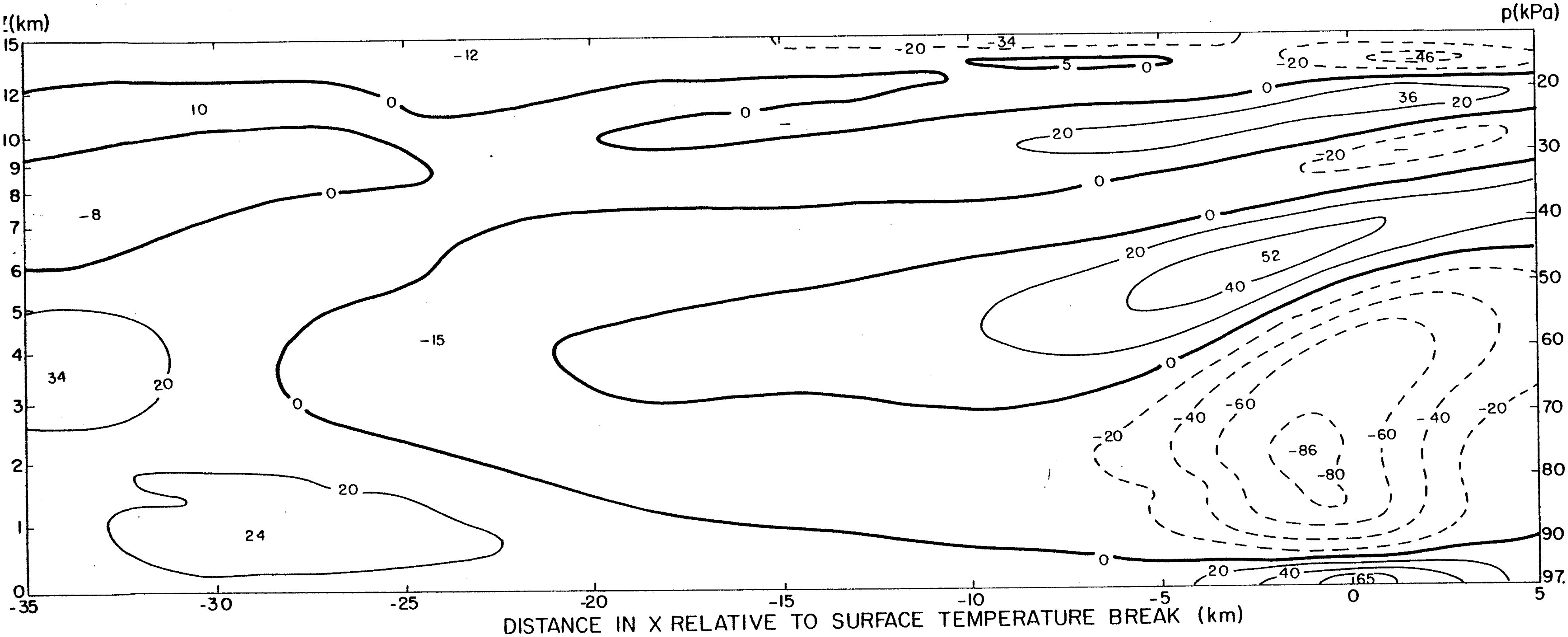

Figure 4.32. The field of $\dot{u}^R$, the real source of the u velocity component, for 107.3 min to 165.4 min. Units are 10^{-4} m s^{-2}, with contours at intervals of 20×10^{-4} m s^{-2}. Negative isopleths are dashed.

affected by changes in the model.

The simplest change to make is to run the model in two dimensions, rather than three, starting from the initial time. This is a comparatively inexpensive test to do since the two-dimensional version runs about three times faster than the three-dimensional version. The results are given in Section 4.4.1.

For changes to the three-dimensional version of the model it would have been expensive to repeat the simulation for the first 100 mins of transient response to the initial conditions, so the sensitivity tests were performed only on the period from 107.3 min to 165.4 min, starting with the fields at 107.3 min from the original simulation. This precluded changes in domain geometry but allowed changes in the parameterizations. The most arbitrary parameters in these are the autoconversion threshold (ρ_{cT}) in the microphysical parameterization and the coefficient k_D in the diffusion parameterization. Sensitivity tests on these are reported in Sections 4.4.2 and 4.4.3 respectively.

4.4.1 Two-Dimensional Simulation

The initial fields for the two-dimensional (2D) simulation were exactly the same as those for the central plane of the three-dimensional (3D) simulation. So there was again a region of extra water vapour just ahead of the cold air.

As happened in the 3D run, the cold air spread forwards and convective cells developed in the warm air aloft. But only the first cell, boosted by the strong transient convergence and extra moisture, developed strongly. It attained a peak updraft of 14.4 m s^{-1} at 44 min. Thereafter, the attempted cell developments were weak, with typical peak updrafts of 2 or 3 m s^{-1} and cloud tops of 4 km. These later cells just could not develop strongly in the two-dimensional geometry; the combination of retarding pressure-gradient forces and suppression due to the vertical wind shear was too much. They resembled the side plane cells in the 3D model which also had trouble developing strongly because they covered two-thirds of the domain in the y direction so were almost two-dimensional.

Following the rainout of the first cell, the cold air produced by evaporative cooling beneath it could only spread forwards and not sideways as allowed in the 3D model. So there was a stronger surge of cold air at the TB, with a stronger temperature gradient behind it. (θ' at 5 km behind the TB was typically -7 K compared with -6 K on the central plane at the same time in the 3D run.) This resulted in both a stronger lee wave structure over the TB and a faster forward speed (about 11 m s^{-1}) of the TB.

In view of the uninteresting results the 2D run was stopped after only 118 min of simulation.

4.4.2 Increase of Autoconversion Threshold

We have already commented in Section 2.2.2 (on microphysical parameterizations) that there was reason to believe that the autoconversion threshold should not be a particularly sensitive parameter because of the feedback effect of accretion of cloud by rain. The conclusion was that an increase in the autoconversion threshold would act to delay the formation of rain but not affect too much the total amount of rain produced.

However, prior to the simulation of 14 May 1970 we were mindful that to grow initial deep cumulus clouds over the TB and have large amounts of evaporation at their tops, as required by SP's explanation for the mesoscale downdraft, a time delay was necessary in the initial rain formation to allow enough cloud water to reach the cumulus tops and be evaporated. So the threshold was thought to be a critical parameter. As it turned out, there was never any indication in the simulation of deep cumulus over the TB and the cloud-water densities there never reached the threshold used of 1.0 g kg^{-1}. Nonetheless, it was thought to be worthwhile to see just how sensitive the results were to an increase in the threshold to 1.5 g kg^{-1}.

The results for the new run, starting from the original fields at 107.3 min, were remarkably similar to the original, with the same time sequence of new cell developments. There was even the same gap in development at 150.6 min, and cell (8) appeared on schedule at the final time of 165.4 min with an updraft of 1.7 m s^{-1} compared with the original of 1.5 m s^{-1}. A very slight tendency was noted for the new cells to have weaker and later peak updrafts, probably due to the increased water load in the early stages of the updrafts.

To determine the effect on rainfall, the maximum rainfall rate at the ground beneath each of the new cells (5) and (6) was determined from the saved fields for each run, with the results plotted in Fig. 4.33. The delay in rain formation due to the higher threshold is evident for each cell, but thereafter the rainfall rates match very closely. Cell (5) reaches a peak of 69 mm hr^{-1} for the lower threshold; the peak for the higher threshold is unknown since it falls between two times.

Time integration over the period for cell (5) using Simpson's method, gives a mean rainfall rate of 31.6 mm hr^{-1} for $\rho_{cT} = 1.0$ g kg^{-1} and 29.4 mm hr^{-1} for $\rho_{cT} = 1.5$ g kg^{-1}. In view of the coarse time resolution for the integration, these rates are very close.

In conclusion, a higher autoconversion threshold has little effect on the model simulation; there tends to be a slightly less rainfall and slightly weaker and later peak updrafts in the convective cells. However, it should be noted that had the model produced rapidly rising convective cells with stronger updrafts, the time delay effect in the initial formation of rain may have been more important to the cell dynamics and had more effect on the simulation.

4.4.3 Variation of k_D

The diagnosis of the eddy diffusion coefficients for heat and momentum, using (2.18) requires the coefficient k_D which was set to 0.42 for the runs previously described in this

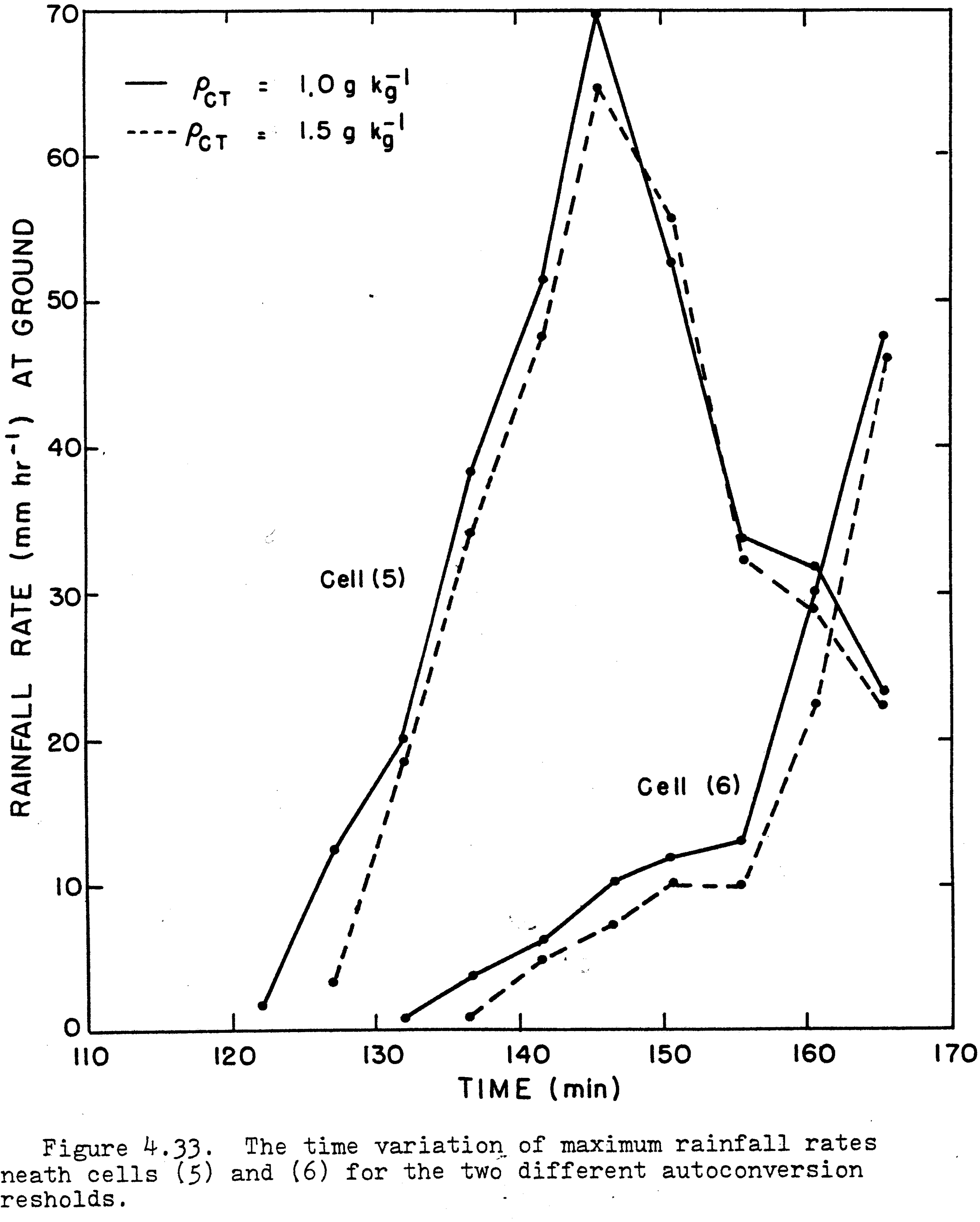

Figure 4.33. The time variation of maximum rainfall rates beneath cells (5) and (6) for the two different autoconversion thresholds.

chapter. To test the sensitivity of the results to the value of k_D the model was rerun from 107.3 min to 165.4 min using $k_D = 0.35$ and $k_D = 0.50$. Since the diffusion coefficients are proportional to the square of k_D, these values give respectively a decrease of 31% and an increase of 42% in the magnitude of the diffusion.

Rather than describe in detail what happened in each of the runs, we will simply point out the major differences from the standard results for $k_D = 0.42$. For $k_D = 0.35$ these were:

(1) The cells were generally stronger, with peak updrafts typically 2 m s^{-1} larger.

(2) The cell development sequence was the same, but with the addition of an extra cell on the central plane at 150.6 min where before there was a gap (see Fig. 4.6).

(3) The averaged vertical motion field $\{[w]\}$ exhibited the same pattern, but the mesoscale updraft area 25 to 35 km behind the TB was about 10% stronger. Corresponding to that was a 10% increase in the apparent source of potential temperature.

(4) The apparent warming of the pool of cold air at the ground was only half as large.

(5) All fields were generally noisier.

For $k_D = 0.50$ the major differences from $k_D = 0.42$ were:

(1) The cells were generally weaker, particularly cell (6) which reached a peak updraft of only 3.0 m s^{-1} compared to 10.9 m s^{-1}.

(2) The cell development sequence was the same, including the gap at about 155 min. Cell (8) had just started to develop at 165.4 min.

(3) In the $\{[w]\}$ field the areas of upward motion over the TB and back in the convective region were completely separated by an area of downward motion. The mesoscale updraft area was about 10% weaker and its associated apparent source of potential temperature was about 20% weaker.

(4) The apparent warming of the cold pool was about 50% stronger.

Almost all of these differences could have been expected a priori, since an increase (decrease) of diffusion should weaken (strengthen) the development of the convective cells and hence the system as a whole. What is important is that, in spite of all three runs having a similar lee wave structure over the TB, the increase in magnitude of the downdraft area (following the surge of cold air) for the case of weakest diffusion was not enough to suppress the cell development at that time and produce a gap. For the operation of this particular feedback mechanism the value of k_D is critical, suggesting that the equality of the interval between cell gaps in the model and line developments on 14 May may have been fortuitous.

5. CONCLUDING REMARKS AND SUGGESTIONS FOR FURTHER WORK

Our stated objective in the Introduction was to numerically simulate a mesoscale convective line like that which occurred in Oklahoma on 14 May 1970, with the particular intent of seeing whether a mesoscale downdraft/updraft doublet developed and whether the system went through the characteristic life cycle postulated by Sanders and Emanuel (1977). Because of the importance of the cumulus convection in the system it was necessary to use a model which, unlike most previous models, could resolve both the cumulus scale and the mesoscale. To that end, in Chapter 2 we designed a model which used stretched co-ordinates in the x and z directions, in order to have good resolution in the region of expected important convection while using a large enough domain to encompass the mesoscale system but not requiring too many grid-points. Also, to alleviate the well-known problems in two-dimensional (slab-symmetric) simulations of cumulus clouds, a crude form of three-dimensionality was proposed. This had three grid-points over a distance of 12 km in the y direction (along the line), assumed periodicity of 12 km, and assumed symmetry about the central grid-point so that computations were needed at only two grid-points.

On the basis of comparison simulations of an isolated cumulus cloud, reported in Chapter 3, we concluded that the model was producing valid results and that there was little difference between clouds simulated using a uniform or a nonuniform grid both having the same horizontal resolution inside the cloud. The three-dimensional version of the model using two computed grid-points (i.e., two computed x-z planes) was significantly better at simulating the cloud than the two-dimensional slab-symmetric model. Although it was also significantly worse than a fully three-dimensional model, a further increase in the number of grid-points in y produced a smaller incremental improvement than that from two-dimensional to the simplest three-dimensional. We therefore decided to use the simplest three-dimensional version for the 14 May simulation.

The model was initialized with temperature and moisture profiles typical of the inflowing air on 14 May, no motion, and a 2 km deep pool of cold air (based on the actual cold front) covering the left two-thirds of the domain. From this highly unbalanced setup, a horizontal wind structure developed in the model which was very similar to that observed. The leading edge of the cold air, or temperature break (TB), advanced at a comparable speed to that of the cold front on 14 May. As on 14 May, convective cells (i.e., lines of cells) developed periodically in the warm air flowing over the cold pool, moved back, and rained out.

However, in many respects the simulated system was very different from the actual one. The differences were mostly in amplitude, and could almost all be traced back to deficiencies in the representation of the third-dimension. So although the simple three-dimensionality was a vast improvement over a slab-symmetric two-dimensional model (which produced only very weak convection) it was unfortunately not good enough to simulate a system of the strength of 14 May. The main differences are enumerated below:

(1) The period of development of new cells in the model was 15 min, compared with an hour on 14 May. The difference was due partly to the model cells' faster movement back from the TB (a result of being rooted in faster-moving air) and partly to their being smaller and less vigorous (a result of the crudeness of the three-dimensionality). An hourly gap in new cell development, caused by modulation of a lee wave over the TB by surges of colder air within the cold pool, resulted in swaths of merged (normal to the line) radar echoes with about the same temporal frequency as the echo lines on 14 May. However, the agreement was probably coincidental since the cell suppression was very sensitive to the magnitude of the parameterized diffusion.

(2) The simulated mesoscale updraft was in approximately the same location as the actual one, but had only a quarter of the amplitude. Further, it was not a persistent, saturated updraft modulated by the passage of convective cells (as on 14 May) but was instead a region of sometimes upward and sometimes downward motion, dominated by the upward motion during the passage of cells near their peak development. The inability of the model to produce a saturated

mesoscale updraft was attributed to a number of reasons, almost all based on the crudeness of the three-dimensionality. The primary reason was that it was difficult for the convection debris to attain a large coverage in y, since it had to do so by a quantum jump from covering just the central plane to covering central and side planes, rather than slowly expanding as it would in nature. Thus the initial mesoscale saturation was difficult to achieve.

(3) The modelled system did not exhibit a life cycle like that on 14 May. Instead, it slowly weakened due to the diffusive warming of the pool of cold air, and the simulation was stopped after four hours simulated time. If a saturated mesoscale updraft had developed there would have been more rain (maintaining the coldness of the cold pool by evaporation) and a more extensive mass of cloud debris, with the probable development of inflow from the rear and a dissociation of the system from the surface TB and wind shift (as on 14 May).

(4) Although there was a simulated downdraft aloft over the TB, it was part of a lee wave produced by air flowing up and over the cold pool and not associated with evaporative cooling from the tops of deep cumulus clouds as apparently occurred on 14 May. The vertical structure of the lee wave corresponded both to linear perturbation theory and to the structure of a vertical oscillation in the u field

observed ahead of the system on 14 May. This led us to believe that it was a real phenomenon and not an artificial result of the model. It is unclear why no lee wave developed on 14 May, but the reason may be that a preexisting field of cumuli ahead of the system was given a boost at the surface wind shift, penetrating deeply enough to prevent the wave from occurring and provide water for evaporation to drive the mesoscale downdraft.

While the deficiency of the representation of the third dimension in the model apparently prevented our being able to simulate a system as strong as that on 14 May, the simulation is perhaps representative of weaker systems which never develop the saturated mesoscale updraft (and which propagate against the wind at all levels, as in the case of many tropical squall lines). It is therefore worthwhile summarizing the main features and interactions that occurred:

(1) The convergence at the leading edge of the mesoscale cold pool (usually produced in nature by previous convection) provides the initial lifting and condensation in the low-level air. Aloft, a lee wave develops, with a sloping phase structure for upward transport of energy and momentum. Its effect extends ahead of the system, producing slow rising and sinking motions that modify the temperature profile of the approaching air.

(2) Embryonic convective cells break off periodically from the cloud over the TB and move back. Their initial develop-

ment is slowed by pressure effects from the lee wave above and by transfer of kinetic energy to the sheared environment they grow in. An upward modulation of the amplitude of the lee wave can cause complete suppression of an embryonic cell.

(3) Once past the downdraft region of the lee wave the cells can develop strongly. Through latent heat release in their updrafts and eddy flux divergence of heat the cells provide enough heating to counterbalance the otherwise-expected dry-adiabatic cooling in the unsaturated mesoscale updraft.

(4) Rain is produced by microphysical interactions in the cell updrafts. As it falls it erodes the lower portions of the cell by accretion of cloud and a drag-induced downdraft. This eventually cuts off the cell from the supply of high θ_e air. Where the rain falls in unsaturated air there is evaporative cooling which aids the cumulus-scale downdraft. Evaporation in the cold pool helps to maintain its coldness and results in occasional forward surges of colder air.

(5) Behind the system an anvil composed of debris from the convection trails back, based at about 6 km. Some light rain continues to fall from it. Below about 4 km there is subsidence driven partly by evaporation of the rain and partly by divergence within the cold pool beneath.

(6) Parameterized diffusion acts everywhere to smooth out

local gradients, but its main effect on the system is to warm the cold pool by transferring heat down from the warm air streaming over the top of it.

One of the most interesting features of the simulation, because it was so unexpected, was the development of the lee wave. We have been able to locate two examples of indirect observational evidence for lee wave structures over gust fronts. The first, in Fig. 5.1, is a photograph taken by Dr Howard Bluestein (personal communication), looking west in Norman, Oklahoma at about 0715 CDT on 27 May 1977 at an approaching severe gust front. (Estimated peak wind speeds with it were more than 25 m s^{-1}, with some minor damage.) The cloud over the gust front was very low based. The photo shows that its upper part was lenticular in character, suggesting that the flow there was stable, with perhaps a lee wave structure above.

The other example is seen in satellite photographs taken at 1510 Z on 22 May 1973 (Erickson and Whitney, 1973). Severe thunderstorms had occurred in the Oklahoma/Arkansas/Texas area overnight with the apparent development of a mesohigh and cold pool, the leading edge of which moved southeastwards accompanied in some areas by roll clouds and a pressure jump. Above the mesohigh, the photos show wave clouds at a level of about 55 kPa which look very much like mountain wave clouds. A rough estimate of their horizontal wavelength is 10 km. Erickson and Whitney believed the waves to have been produced by the earlier violent convection (perhaps interacting with the tropopause in

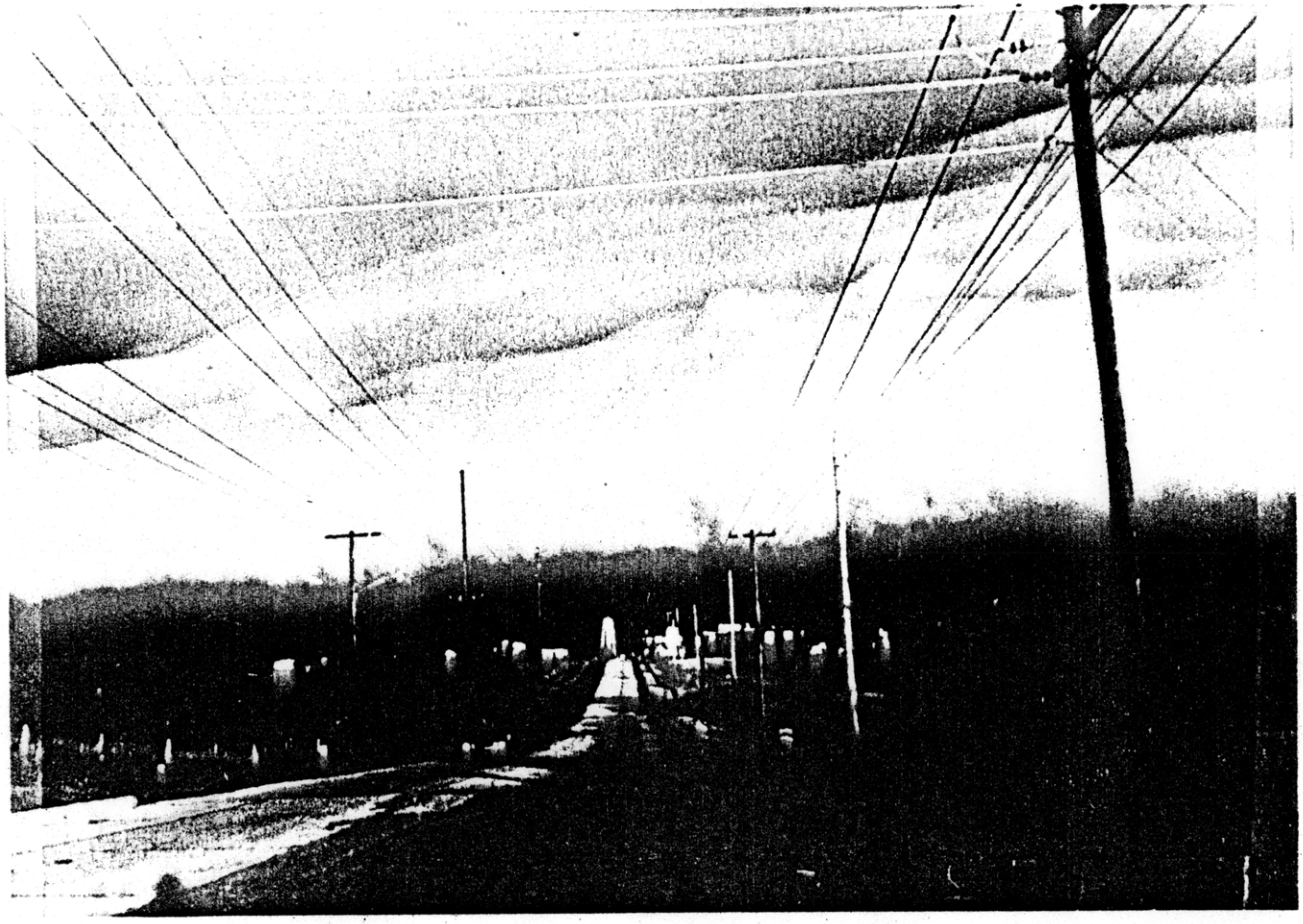

Figure 5.1. **Photograph of an approaching severe gust front. Taken at** 0715 CDT, 27 May 1977 with a 28 mm lens, looking west in Norman, Oklahoma. (Courtesy of Dr Howard Bluestein.)

the manner suggested by Curry and Murty, 1974). A more plausible explanation suggested by the work in this thesis is that they were lee waves produced by the southeastwards motion of a gust front at the leading edge of the mesohigh. Since the gust front was moving through dry low-level air no convection was produced to disturb the waves.

Further modelling work along the lines in this thesis would definitely benefit from better spatial resolution, particularly in the third dimension. The assumption of symmetry in the third dimension should also be removed, both because of its artificiality and to allow a mean flow along the line and the incorporation of the Coriolis force. For the simulation reported here the microphysical parameterization was adequate, but in cases of stronger simulated updrafts some account should be taken of a time delay effect in initial production of rain. Limited ice microphysics could also be added. The diffusion parameterization is definitely in need of improvement, if not by changing it to a second-order closure scheme like that of Manton and Cotton (1977) then at least by determining a less arbitrary value for the parameter k_D. If diffusion is to act on perturbations from base-state profiles, then those profiles should be chosen with more care to avoid the problems noted in Section 4.3.3.3.

With some or all of these improvements a new attempt should be made to simulate the mesoscale convective line of 14 May. If the Coriolis force has been incorporated then it should be possible to start the simulation in a balanced state representative of the situation before the convection developed, just as Soong and Bloom (1977) have tried for another case from the NSSL mesonetwork (8 June 1966). In view of the significance attached to a pre-existing field of cumuli in the development of the mesoscale downdraft, it would be worthwhile trying to produce such a field by surface heating or some other forcing.

Other cases from the NSSL archives could also be simulated. A likely candidate is the squall line of 26 April 1969, since Stokes' (1977) observational study provides a basis for comparison. In that case there was strong vertical wind shear along the line so the Coriolis force would probably be very important.

Finally, <u>direct</u> observational evidence should be sought for the existence of lee waves over gust fronts. The most obvious source of data is from aircraft traverses at an altitude of 5 or 6 km. Data from one squall line during the GATE, studied by Emanuel (1976), has already been looked at but showed no evidence of the phase relationships between temperature and vertical velocity which would characterize a lee wave. Further aircraft data from the GATE, the NSSL network, and other field programs should be examined.

Appendix A

LIST OF SYMBOLS

Symbol	Definition
a	$R_w/R_d - 1$ (= 0.6078).
a_F	Filter function used in (4.3) for the definition of $\{[Q]\}$.
$a_0, a_1, \ldots$	Polynomial coefficients for e_{sw} (see Appendix B).
A	Sum of advection and diffusion terms in u momentum equation (2.2).
AA	Sum of diagnosed autoconversion and accretion rates, used in (2.52).
al_i, am_j	Coefficients in diagnostic pressure equation (2.48).
$b_0, b_1, \ldots$	Polynomial coefficients for de_{sw}/dT (see Appendix B).
B	Sum of advection and diffusion terms in v momentum equation (2.3).
C	Sum of advection, diffusion and buoyancy terms in w momentum equation (2.4).
C_D	Drag coefficient, used in (2.44).
C_p	Specific heat of dry air at constant pressure (1005 $m^2\ s^{-2}\ K^{-1}$).
cl_i, cm_j	Coefficients in diagnostic pressure equation (2.48).
d	The assumed constant ratio of K_H/K_m.
D	Raindrop diameter in the Marshall-Palmer distribution (2.8). Deformation, with magnitude given by (2.22).
D_Q	Parameterized diffusion term in (4.1).

Symbol	Definition	
DUU	$\partial u/\partial x + \partial u/\partial x$	velocity gradients used in determining the deformation and in the computation of friction.
DUV	$\partial u/\partial y + \partial v/\partial x$	
DUW	$\partial u/\partial z + \partial w/\partial x$	
DVV	$\partial v/\partial y + \partial v/\partial y$	
DVW	$\partial v/\partial z + \partial w/\partial y$	
DWW	$\partial w/\partial z + \partial w/\partial z$	
e_{sw}	Saturation vapour pressure over water, determined as a function of temperature as described in Appendix B.	
F	Forcing function in the pressure equation, defined by (2.49).	
$\mathbb{F}$	Fourier coefficient of the variation of F in the y direction.	
F_x, F_y, F_z	Frictional forces per unit volume.	
g	Acceleration of gravity (9.80 m s^{-2}).	
G	Computational net divergence, as defined in (2.5).	
HEIGHT	Vertical height of the domain of integration.	
i	Grid co-ordinate in the x direction.	
j	Grid co-ordinate in the z direction.	
k	Grid co-ordinate in the y direction. Horizontal wavenumber of gravity wave.	
k_a	Autoconversion rate constant, used in (2.13).	
k_D	Constant in eddy diffusion coefficient formula (2.18).	
kc	Superscript for Fourier coefficients.	
K_H	Eddy diffusion coefficient for heat ($= d \times K_M$).	
K_M	Eddy diffusion coefficient for momentum.	
l^2	Scorer parameter, defined by (4.11).	
L	Number of pressure grid-points in the x direction.	

Symbol	Definition
L_0, L_1, L_2	Horizontal wavelengths of theoretical gravity waves over the TB (see Table 4.1).
L_{vw}	Latent heat of vaporization of water $(2.5 \times 10^6\ m^2\ s^{-2})$.
LENGTH	Length of the domain in x.
M	Number of pressure grid-points in the vertical.
N	Number of computed pressure grid-points in the y direction. Number of raindrops per unit diameter in Marshall-Palmer distribution (2.8).
N_0	Intercept in Marshall-Palmer distribution (2.8).
N_c	Number of cloud droplets per unit volume.
p	Pressure.
Δp	Pressure interval used for co-ordinate stretching in the vertical.
p_0	Surface pressure for z stretching formula (2.29).
P	Transformed nondimensional pressure, as defined by (2.1).
$\mathbb{P}$	Fourier coefficient of the variation of P in the y direction.
Q_C	Mixing ratio of cloud-water.
Q_R	Mixing ratio of rain-water.
Q_V	Mixing ratio of water vapour.
ΔQ_V	Change in Q_V for saturation adjustment (2.53).
Q_{VS}	Saturation mixing ratio of water vapour, given by (2.12).
ΔQ_{VS}	Change in Q_{VS} for saturation adjustment (2.53).

Symbol	Definition
R_d	Gas constant for dry air (287.0 m^2 s^{-2} K^{-1}).
R_w	Gas constant for water vapour (461.5 m^2 s^{-2} K^{-1}).
Ri	Richardson number, defined by (2.20).
t	Time.
Δt	Integration time-step.
T	Temperature.
ΔT	Temperature change for saturation adjustment (2.53).
T_0	Surface temperature for z stretching formula (2.29).
u	Velocity component in x.
u_a	u at imaginary anemometer level.
UTRANS	Translational speed of the domain in x.
v	Velocity component in y.
v_a	v at imaginary anemometer level.
$\underset{\sim}{V}$	Velocity vector.
w	Velocity component in z.
w_0, w_1, w_2	Vertical structures of theoretical gravity waves over the TB (see Fig. 4.24).
w_m	Vertical structure of the model gravity wave over the TB (see Fig. 4.24).
w_R	Terminal velocity for rain.
WIDTH	The width of the computational domain in y - fields are assumed periodic with this period.
x	Horizontal space co-ordinate.
Δx	Grid spacing in x ($\Delta x_i = x_{i+\frac{1}{2}} - x_{i-\frac{1}{2}}$ etc.).

Symbol	Definition
y	Horizontal space co-ordinate, orthogonal to x.
Δy	Grid spacing in y, constant at WIDTH/(N+N-1).
z	Vertical space co-ordinate.
Δz	Grid spacing in z ($\Delta z_{j-\frac{1}{2}} = z_j - z_{j-1}$ etc.).
α	Expression used in (2.44) to determine anemometer-level wind components.
β	$\partial Q_{vs}/\partial T$, used in saturation adjustment (2.53).
Γ	Representative vertical temperature gradient, $-\partial T/\partial z$, used for z stretching formula (2.29).
Δ	Grid spacing scale for diffusion coefficient determination.
θ	Potential temperature.
θ_e	Equivalent potential temperature.
λ	Parameter in Marshall-Palmer distribution (2.8).
ρ	Air density.
ρ_o	Mean-sea-level air density (1.225 kg m^{-3}).
ρ_{cT}	Threshold density of cloud-water for autoconversion.
ω	Frequency $(2\pi/(N-1))$ used for Fourier series in y.
∇	Three-dimensional divergence operator.

The following conventions may be used to qualify these symbols:

(a) An overbar, e.g., $\overline{p}$, denotes the base-state value, a function of z only.

(b) A prime, e.g., θ' , denotes a deviation from the base-state.

(c) Subscripts involving i, j , and k represent positions on the grid.

(d) A tilde, e.g., $\tilde{u}_{ijk}$ or $\tilde{G}_{i-\frac{1}{2},j,k}$, is used for an estimated advecting velocity (obtained by a weighted sum of known velocities at standard grid-points) and for the field of computational net divergence derived from those estimated velocities.
In Section 4.3.3 it is used to denote the deviation of a quantity from its space- and time-averaged value, as defined by (4.4).

(e) All variables are generally assumed to be for time t unless they have superscripts of $t-\Delta t$ or $t+\Delta t$, or are starred (e.g., $Q_c{}^{*}_{ijk}$) to denote a first-guess value for time $t+\Delta t$.

(f) A dotted variable, such as $\dot{\theta}$, represents the real rate of change of that quantity, as defined by (4.1).
With a superscript A, e.g., $\dot{\theta}^A$, it is the apparent source defined by (4.5).
With a superscript R, e.g., $\dot{\theta}^R$, it is the real source defined by (4.6).
With a superscript V, e.g., $\dot{\theta}^V$, it is the virtual source defined by (4.7).
With a superscript D, e.g., $\dot{\theta}^D$, it is the diffusive source defined by (4.8).

(g) Square brackets, e.g., $[u]$, denote an average in time and y as defined by (4.2).
Additional curly brackets, e.g., $\{[u]\}$, denote that the average has also been filtered in x as defined by (4.3).

Appendix B

COMPUTATION OF SATURATION VAPOUR PRESSURE

The standard values for saturation vapour pressure over water, e_{sw}, are given by the Goff and Gratch (1946) formula, over the range -50°C to +50°C. Lowe (1977) gives an accurate sixth-order Chebyschev polynomial fit over this range, with coefficients:

$$\begin{aligned} a_0 &= 6.107\,799\,961 \times 10^{2} \\ a_1 &= 4.436\,518\,521 \times 10^{1} \\ a_2 &= 1.428\,945\,805 \times 10^{0} \\ a_3 &= 2.650\,648\,471 \times 10^{-2} \\ a_4 &= 3.031\,240\,396 \times 10^{-4} \\ a_5 &= 2.034\,080\,948 \times 10^{-6} \\ a_6 &= 6.136\,820\,929 \times 10^{-9} \end{aligned} \tag{B.1}$$

where

$$e_{sw}(T) = \sum_{n=0}^{6} a_n (T-273.16)^n \tag{B.2}$$

for T in degrees kelvin.

Lowe also gives a sixth-order fit to the first derivative of e_{sw}, with coefficients:

$$\begin{aligned} b_0 &= 4.438\,099\,984 \times 10^{1} \\ b_1 &= 2.857\,002\,636 \times 10^{0} \\ b_2 &= 7.938\,054\,040 \times 10^{-2} \\ b_3 &= 1.215\,215\,065 \times 10^{-3} \\ b_4 &= 1.036\,561\,403 \times 10^{-5} \\ b_5 &= 3.532\,421\,810 \times 10^{-8} \\ b_6 &= -7.090\,244\,804 \times 10^{-11} \end{aligned} \tag{B.3}$$

where

$$\frac{de_{sw}(T)}{dT} = \sum_{n=0}^{6} b_n (T-273.16)^n \tag{B.4}$$

This derivative is used to compute β, for the saturation adjustment equations (2.53).

These formulations were used for all the runs described in this thesis. It was then discovered that for temperatures less than -60°C the formula (B.2) with coefficients (B.1) gave <u>negative</u> saturation vapour pressures; this had not affected the previous results since the lowest temperature in the model runs had been about -58°C.

To fix this up, new polynomials were fitted to the Goff-Gratch formula over the range -70°C to +50°C, and should be used for future runs. The polynomials were fitted so that the maximum absolute percentage error was minimized, rather than the (usual) maximum absolute error. The resulting coefficients for an eighth-order polynomial fitting e_{sw} to within 0.1% over the range are:

$$\begin{aligned}
a_0 &= 6.107\,815\,684\,584 \times 10^{2}\\
a_1 &= 4.438\,807\,668\,690 \times 10^{1}\\
a_2 &= 1.429\,868\,651\,122 \times 10^{0}\\
a_3 &= 2.646\,198\,206\,649 \times 10^{-2}\\
a_4 &= 3.016\,596\,455\,980 \times 10^{-4}\\
a_5 &= 2.054\,874\,158\,231 \times 10^{-6}\\
a_6 &= 6.732\,227\,159\,465 \times 10^{-9}\\
a_7 &= -2.713\,799\,743\,227 \times 10^{-12}\\
a_8 &= -6.354\,261\,479\,512 \times 10^{-14}
\end{aligned} \tag{B.5}$$

and the coefficients for de_{sw}/dT to within 0.0035% are:

$$\begin{aligned}
b_0 &= 4.436\,720\,750\,255 \times 10^{1}\\
b_1 &= 2.858\,710\,330\,986 \times 10^{0}\\
b_2 &= 7.938\,394\,518\,547 \times 10^{-2}\\
b_3 &= 1.209\,410\,684\,776 \times 10^{-3}\\
b_4 &= 1.036\,394\,121\,013 \times 10^{-5}\\
b_5 &= 4.024\,733\,743\,536 \times 10^{-8}\\
b_6 &= -6.334\,203\,612\,658 \times 10^{-11}\\
b_7 &= -1.183\,993\,899\,828 \times 10^{-12}\\
b_8 &= -3.183\,611\,880\,027 \times 10^{-15}
\end{aligned} \tag{B.6}$$

Appendix C

THE SHAPIRO FILTER

The sixteenth-order Shapiro filter (Shapiro, 1970) is defined by:

$$F_S(\phi) = \left(1-(F_H^2)^8\right)(\phi) \tag{C.1}$$

where the second-order, high-pass filter F_H^2 is computed by:

$$F_H^2(\phi_i) = \frac{1}{4}\left(-\phi_{i-1} + 2\phi_i - \phi_{i+1}\right) \tag{C.2}$$

and has a response amplitude of $\sin^2(\pi/\ell)$ for a wavelength of ℓ grid-points. The response for the filter F_S is thus $1 - \sin^{16}(\pi/\ell)$.

To compute F_S at a single point we need grid-point values at a total of seventeen points - the central one plus eight on either side. Near the boundaries we must either reduce the order of the filter to accommodate the available number of points, or use a boundary condition to implicitly obtain the extra points. Here we assume symmetry at each boundary, so that if we are filtering the grid-point values $\phi_1, \phi_2 \dots, \phi_L$ the boundary conditions for the filter application are:

$$\phi_0 = \phi_1, \quad \phi_{-1} = \phi_2, \quad \phi_{-2} = \phi_3, \dots$$

and

$$\phi_{L+1} = \phi_L, \quad \phi_{L+2} = \phi_{L-1}, \quad \phi_{L+3} = \phi_{L-2}, \dots$$

Each application of the filter F_H^2 is accomplished in two steps:

(1) $\phi^{(1)}_{i+\frac{1}{2}} = \phi_{i+1} - \phi_i$ for $i = 1, 2, \dots, L-1$

boundary conditions give $\phi^{(1)}_{\frac{1}{2}} = \phi^{(1)}_{L+\frac{1}{2}} = 0$ etc.

(2) $\phi^{(2)}_i = \phi^{(1)}_{i-\frac{1}{2}} - \phi^{(1)}_{i+\frac{1}{2}}$ for $i = 1, 2, \dots, L$

boundary conditions give $\phi^{(2)}_0 = \phi^{(2)}_1, \; \phi^{(2)}_{L+1} = \phi^{(2)}_L$ etc.

The resulting vector $\phi_i^{(2)}$ is equal to $4 \times F_H^2\ (\phi)$; eight successive applications give $(4 \times F_H^2)^8\ (\phi)$, which is multiplied by 4^{-8} and subtracted from the original vector to obtain $F_S(\phi)$. As noted by Francis (1975), the filtering requires only seventeen additions and one multiplication for each point - a remarkably small amount of computation.

The filter has the property that it conserves ϕ under the given boundary conditions, i.e.,

$$\sum_{i=1}^{L} F_S(\phi_i) = \sum_{i=1}^{L} \phi_i$$

In the model it is applied in the x direction only, to the fields of $Q_V{}^*_{ijk}$ and θ'^*_{ijk} for i from 2 to $L - 1$, and all j and k. This does not give exact conservation - the filter would have to be applied to the fields of $\Delta x_i\, Q_V{}^*_{ijk}$ and $\Delta x_i\, \theta'^*_{ijk}$ to do that.

Appendix D

PROGRAMMING CONSIDERATIONS

The model was programmed entirely in FORGOL, a language developed by the author during the course of this research, and described fully in Gordon (1977). The language is an extension of FORTRAN which includes a number of syntactic constructs similar to those in ALGOL. As an example, the FORTRAN loop

```
   DO 10 I=1,L
   X(I)=0.0
10 Y(I)=0.0
```

could be programmed in FORGOL as

```
@FOR I=1,L @DO @BEGIN X(I)=0.0; Y(I)=0.0 @END
```

Other FORGOL constructs include "@IF condition @THEN statement @ELSE statement", and "@WHILE condition @DO statement".

Another feature of the language is the macro facility: An identifier can be defined to represent a string of characters so that subsequent use of the identifier will be replaced by the string. This is very useful in setting array dimensions at compile time, and in programming all the finite-difference equations. The field arrays are named and subscripted according to conventions depending on the grid-point type. For instance, $u_{\frac{1}{2},j,k}$ is stored at UFJK(1,J,K), and $w_{i,3/2,k}$ at WIGK(I,2,K). These conventions allow macro definitions such as

```
¢IMH_J_K#FJK(I,J,K)#
¢IPH_J_K#FJK(I+1,J,K)#
```

where the macro definition is introduced by a cent sign (¢), and the string is contained within number signs (#). (Note that the underline character is completely ignored.) Then the expression $u_{i+\frac{1}{2},j,k} - u_{i-\frac{1}{2},j,k}$ may be written down immediately as

```
U¢IPH_J_K - U¢IMH_J_K
```

where the absence of the following # causes the macro identifier to be replaced by its corresponding string of characters.

A test can be made on the first character of a macro string to see whether it is a "T" (meaning true) or an "F" (meaning false); on the basis of this the subsequent section of code will either be processed or ignored, respectively. As an example, suppose we define

```
¢3D#FALSE#
```

and then write the following code:

```
@FOR I=1,L @DO @FOR J=1,M @DO  ?(3D @FOR K=1,N @DO ?)
G¢I_J_K = (U¢IPH_J_K - U¢IMH_J_K)/DX¢I
          +(RHOB¢JPH*W¢I_JPH_K - RHOB¢JMH*W¢I_JMH_K)
                                  /(RHOB¢J * DZ¢J)
    ?(3D +(V¢I_J_KPH - V¢I_J_KMH)/DY ?)
```

Referral to the finite-difference equation (2.30) will show that this code corresponds to it exactly. Since the macro identifier has been set to the string "FALSE" we are programming only a two-dimensional model. The loop over K at the end of the first line - between the bracketing ?(3D and ?) - is completely ignored, as is the entire last line (computing the gradient of the v velocity component).

By such means, it was possible to write the entire model as one set of programs which could then be compiled as either a two- or a three-dimensional model by changing only a single card (defining the macro 3D) at the front of the deck.

The FORGOL source programs were first translated to FORTRAN and then compiled into machine code using a FORTRAN H optimizing compiler. All fields were in single precision - approximately seven significant digits. The computations were carried out via a remote terminal to the Goddard Institute for Space Studies' IBM 360/95 in New York, and AMDAHL 470 in Beltsville, Maryland.

REFERENCES

Ackerman, B., 1967: The nature of meteorological fluctuations in clouds. J. Appl. Meteor., 6, 61-71.

American Meteorological Society, 1974: SI units to be used in AMS journals. Bull. Amer. Meteor. Soc., 55, 926-930.

Asai, T., 1964: Cumulus convection in the atmosphere with vertical wind shear. J. Meteor. Soc. Japan, 42, 245-259.

________, 1965: A numerical study of the air-mass transformation over the Japan Sea in winter. J. Meteor. Soc. Japan, 43, 1-15.

Battan, L. J., 1963: Relationship between cloud base and initial radar echo. J. Appl. Meteor., 2, 333-336.

Betts, A. K., 1974: The scientific basis and objectives of the U.S. convection subprogramme for the GATE. Bull. Amer. Meteor. Soc., 55, 304-313.

Brown, J. M., 1975: Mesoscale motions induced by cumulus convection: a numerical study. Ph.D. thesis, M.I.T., 207 pp.

Browning, K. A., and D. Atlas, 1965: Initiation of precipitation in vigorous convective clouds. J. Atmos. Sci., 22, 678-683.

Bryan, K., 1966: A scheme for numerical integration of the equations of motion on an irregular grid free of nonlinear instability. U.S. Mo. Wea. Rev., 94, 39-40.

Chalon, J.-P., J. C. Fankhauser, and P. J. Eccles, 1976: Structure of an evolving hailstorm, Part I: General characteristics and cellular structure. U.S. Mo. Wea. Rev., 104, 564-575.

Clark, T. L., 1973: Numerical modeling of the dynamics and microphysics of warm cumulus convection. J. Atmos. Sci., 30, 857-878.

________, 1976: Use of log-normal distributions for numerical calculations of condensation and collection. J. Atmos. Sci., 33, 810-821.

Cotton, W. R., 1972: Numerical simulation of precipitation development in supercooled cumuli - Part I. U.S. Mo. Wea. Rev., 100, 757-763.

Curry, M. J., and R. C. Murty, 1974: Thunderstorm-generated gravity waves. J. Atmos. Sci., 31, 1402-1408.

Dutton, J. A., and G. H. Fichtl, 1969: Approximate equations of motion for gases and liquids. J. Atmos. Sci., 26, 241-254.

Eliassen, A., 1974: Mountain waves. Subsynoptic Extratropical Weather Systems: Observations, Analysis, Modeling and Prediction. NCAR Summer Colloquium, Boulder, Colo., 138-149.

Emanuel, K. A., 1976: Preliminary investigation of a tropical squall mesosystem as observed by aircraft during GATE. NCAR Tech. Note. TN-119, 39-70.

Erickson, C. O., and L. F. Whitney, Jr., 1973: Picture of the month: Gravity waves following severe thunderstorms. U.S. Mo. Wea. Rev., 101, 708-711.

Fankhauser, J. C., 1974: The derivation of consistent fields of wind and geopotential height from mesoscale rawinsonde data. J. Appl. Meteor., 13, 637-646.

Francis, P. E., 1975: The use of a multipoint filter as a dissipative mechanism in a numerical model of the general circulation of the atmosphere. Quart. J. Roy. Meteor. Soc., 101, 567-582.

Goff, J. A., and S. Gratch, 1946: Low-pressure properties of water from -160 to 212 F. Heating, Piping and Air Conditioning, 18, 125-136.

Gordon, N. D., 1977: The FORGOL preprocessor. Unpublished notes, 14 pp.

Hane, C.E., 1973: The squall line thunderstorm: Numerical experimentation. J. Atmos. Sci., 30, 1672-1690.

Hill, G. E., 1974: Factors controlling the size and spacing of cumulus clouds as revealed by numerical experiments. J. Atmos. Sci., 31, 646-673.

Holloway, J. L., 1958: Smoothing and filtering of time series and space fields. Adv. Geophys., 4, 351-389.

Howard, L. N., 1961: Note on a paper of John W. Miles. J. Fluid Mech., 10, 509-512.

Kálnay de Rivas, E., 1975: On the use of nonuniform grids in finite-difference equations. J. Comp. Phys., 10, 202-210.

Kasahara, A., and W. M. Washington, 1967: NCAR global general circulation model of the atmosphere. U.S. Mo. Wea. Rev., 95, 389-402.

Kessler, E., 1969: On the distribution and continuity of water substance in atmospheric circulations. Meteor. Monog., 10, 84 pp.

Klemp, J. B., and R. B. Wilhelmson, 1977: The simulation of three-dimensional convective storm dynamics. Preprints, Tenth Conf. on Severe Local Storms, Omaha, Neb., Amer. Meteor. Soc., 283-290.

Kreitzberg, C.W., and D. J. Perkey, 1976: Release of potential instability: Part I. A sequential plume model within a hydrostatic primitive equation model. J. Atmos. Sci., 33, 456-475.

________, and ________, 1977: Release of potential instability: Part II. The mechanism of convective/mesoscale interaction. J. Atmos. Sci., 34, 1569-1595.

Kyle, T. G., W. R. Sand, and D. J. Musil, 1976: Fitting measurements of thunderstorm updraft profiles to model profiles. U.S. Mo. Wea. Rev., 104, 611-617.

Lilly, D. K., 1962: On the numerical simulation of buoyant convection. Tellus, 14, 148-172.

Lowe, P. R., 1977: An approximating polynomial for the computation of saturation vapour pressure. J. Appl. Meteor., 16, 100-103.

Malkus, J. S., 1952: The slopes of cumulus clouds in relation to external wind shear. Quart. J. Roy. Meteor. Soc., 78, 530-542.

Manton, M. J., 1974: On the dispersion of a developing droplet spectrum in a turbulent cloud. Tellus, 26, 489-494.

________, and W. R. Cotton, 1977: Formulation of approximate equations for modeling moist deep convection on the mesoscale. Colorado State University Atmos. Sci. Paper No. 266, 62 pp.

Marshall, J. S., and W. McK. Palmer, 1948: The distribution of raindrops with size. J. Meteor., 5, 165-166.

Mason, B. J., and J. B. Andrews, 1960: Dropsize distributions from various types of rains. Quart. J. Roy. Meteor. Soc., 86, 346-353.

Meneely, J. M., 1972: A study of the convective storms of 14 May 1970 using data from the NSSL rawinsonde mesonetwork. S.M. thesis, M.I.T., 100 pp.

Miles, J. W., 1961: On the stability of heterogeneous shear flows. J. Fluid Mech., 10, 496-508.

Miller, M. J., and A. K. Betts, 1977: Travelling convective storms over Venezuela. U.S. Mo. Wea. Rev., 105, 833-848.

Mitchell, K. E., and J. B. Hovermale, 1977: A numerical investigation of the severe thunderstorm gust front. U.S. Mo. Wea. Rev., 105, 657-675.

Molenkamp, C. R., 1968: Accuracy of finite-difference methods applied to the advection equation. J. Appl. Meteor., 7, 160-167.

Moncrieff, M. W., and M. J. Miller, 1976: The dynamics and simulation of tropical cumulonimbus and squall lines. Quart. J. Roy. Meteor. Soc., 102, 373-394.

Ogura, Y., and J. G. Charney, 1960: A numerical model of thermal convection in the atmosphere. Int. Symposium on N.W.P., Proc., Tokyo, Japan, Nov. 1960, 431-451.

________, and N. A. Phillips, 1962: Scale analysis of deep and shallow convection in the atmosphere. J. Atmos. Sci., 19, 173-179.

Piacsek, S. A., and G. P. Williams, 1970: Conservation properties of convection difference schemes. J. Comp. Phys., 6, 392-405.

Sanders, F., and K. A. Emanuel, 1977: The momentum budget and temporal evolution of a mesoscale convective system. J. Atmos. Sci., 34, 322-330.

________, and R. J. Paine, 1975: The structure and thermodynamics of an intense mesoscale convective storm in Oklahoma. J. Atmos. Sci., 32, 1563-1579.

Sasaki, Y., 1959: A numerical experiment of squall-line formation. J. Meteor., 16, 347-353.

Schlesinger, R. E., 1973: A numerical model of deep moist convection: Part I. Comparative experiments for variable ambient moisture and wind shear. J. Atmos. Sci., 30, 835-856.

________, 1975: A three-dimensional model of an isolated deep convective cloud: Preliminary results. J. Atmos. Sci., 32, 934-957.

________, 1977: A three-dimensional numerical model of an isolated large-diameter thunderstorm: Results of an experiment with directional ambient wind shear. Preprints, Tenth Conf. on Severe Local Storms, Omaha, Neb., Amer. Meteor. Soc., 255-262.

Shapiro, R., 1970: Smoothing, filtering and boundary effects. Rev. Geophys. and Space Phys., 8, 359-387.

Simpson, J. E., 1969: A comparison between laboratory and atmospheric density currents. Quart. J. Roy. Meteor. Soc., 95, 758-765.

Soong, S.-T., and S. C. Bloom, 1977: A numerical simulation of the formation of a mid-latitude squall line. Preprints, Tenth Conf. on Severe Local Storms, Omaha, Neb., Amer. Meteor. Soc., 265-266.

________, and Y. Ogura, 1973: A comparison between axisymmetric and slab-symmetric cumulus cloud models. J. Atmos. Sci., 30, 879-893.

Steiner, J. T., 1973: A three-dimensional model of cumulus cloud development. J. Atmos. Sci., 30, 414-435.

Stokes, J., 1977: Mesoscale structure and heat and moisture budgets for an Oklahoma squall line. Submitted to J. Atmos. Sci.

Swarztrauber, P., and R. Sweet, 1975: Efficient FORTRAN subprograms for the solution of elliptic partial differential equations. NCAR Tech. Note. NCAR-TN/IA-109.

Tepper, M., 1950: A proposed mechanism of a squall line: The pressure jump line. J. Meteor., 7, 21-29.

Walsh, J. E., 1974: Sea breeze theory and applications. J. Atmos. Sci., 31, 2012-2026.

________, 1976: On the nesting of grids in nonhydrostatic computations. U.S. Mo. Wea. Rev., 104, 735-743.

Wilhelmson, R., 1974: The life cycle of a thunderstorm in three dimensions. J. Atmos. Sci., 31, 1629-1651.

________, and Y. Ogura, 1972: The pressure perturbation and the numerical modelling of cloud. J. Atmos. Sci., 29, 1295-1307.

Yamasaki, M., 1975: A numerical experiment of the interaction between cumulus convection and the larger-scale motion. Pap. Meteor. Geophys., 26, 63-91.

Yau, M. K., 1977: Microphysical-dynamical processes and interactions in a precipitating cumulus cell model. Sc.D. thesis, M.I.T., 256 pp.

Zipser, E. J., 1969: The role of organized unsaturated convective downdrafts in the structure and rapid decay of an equatorial disturbance. J. Appl. Meteor., 8, 799-814.

BIOGRAPHICAL NOTE

The author was born on 4 October 1951 in Auckland, New Zealand, where he spent his childhood and attended local schools. From 1969 to 1971 he studied at the University of Auckland, graduating with a B.Sc. During this time he met Jennifer Huzziff and they were married in January 1971.

In 1972 he attended the Victoria University of Wellington and graduated with a B.Sc. (Hons, 1st Class) in Information Science. He then worked for the N.Z. Meteorological Service in Wellington, doing computer programming in the research section, and aviation, marine, and public forecasting.

In September 1974 he entered the Department of Meteorology at M.I.T. as a graduate student, with the assistance of a N.Z. National Research Advisory Council fellowship.